Progress in Materials Science 133 (2023) 101066

Contents lists available at ScienceDirect

Progress in Materials Science

journal homepage: www.elsevier.com/locate/pmatsci

A state-of-the-art review on fatigue performance of powder bed fusion-built alloy 718

Esmaeil Sadeghi [a,*], Paria Karimi [a], Reza Esmaeilizadeh [a], Filippo Berto [b], Shuai Shao [c,d], Johan Moverare [e], Ehsan Toyserkani [a], Nima Shamsaei [c,d]

[a] Multi-Scale Additive Manufacturing Lab, University of Waterloo, Waterloo N2L 3G1, Canada
[b] Department of Chemical Engineering Materials Environment, SAPIENZA - UNIVERSITÀ DI ROMA, 00184 Roma, Italy
[c] Department of Mechanical Engineering, Auburn University, Auburn, AL 36849, USA
[d] National Center for Additive Manufacturing Excellence (NCAME), Auburn University, Auburn, AL 36849, USA
[e] Department of Management and Engineering, Division of Engineering Materials, Linköping University, Linköping SE-58183, Sweden

ARTICLE INFO

Keywords:
Additive manufacturing
Powder bed fusion
Microstructural characteristics
Fatigue and fracture
Alloy 718

ABSTRACT

Alloy 718 is a Ni-Fe-based superalloy, which has been successfully adapted to powder bed fusion (PBF) additive manufacturing because of the alloy's adaptability with such emerging technology in achieving enhanced mechanical properties. Despite a promising perspective for PBF-built Alloy 718 in different industries, a few factors, including microstructural non-uniformities, volumetric defects, undesired non-metallic inclusions, anisotropic behavior, residual stress, as well as surface and sub-surface irregularities, lead to premature fatigue life of the parts. However, the PBF technology has been quickly growing, and associate progress has resulted in substantial advances in quality, hence increased fatigue life of the parts. Therefore, a critical assessment of the efficacy of the PBF-built Alloy 718 parts can be highly enlightening. A fundamental understanding of the relationship between feedstock material, manufacturing process, process parameters, microstructure, properties, and fatigue life of PBF-built Alloy 718 is crucial for improving the characteristics of the current materials, designing new alloy systems, and enhancing the capability of the PBF techniques. The present paper aims to comprehensively review the fundamentals and recent advances in the PBF-built Alloy 718 parts with improved fatigue life, the influence of thermal and mechanical post-treatment, mechanisms of fatigue crack initiation and growth, thermo-mechanical fatigue, dwell-time fatigue, as well as fracture behavior in different loading conditions and environments considering anisotropic characteristics of the material. An unbiased review of the literature provides an understanding of the advanced and outstanding achievements in the field that assure further research. An evaluation of the status of the field, the gaps in the theoretical understanding, and the fundamental needs for the sustainable development of PBF-built Alloy 718 with enhanced fatigue life in specific applications are also provided.

* Corresponding author.
E-mail address: esmaeil.sadeghi@uwaterloo.ca (E. Sadeghi).

https://doi.org/10.1016/j.pmatsci.2022.101066
Received 4 August 2021; Received in revised form 5 November 2022; Accepted 14 December 2022
Available online 19 December 2022

Nomenclature

2Nf	number of reversals to failure
AM	additive manufacturing
BCT	body-centered tetragonal
CAD	computer aided design
CSL	coincident site lattice
CT	computed tomography
DA	direct aging
DE	dynamic embrittlement
DED	directed energy deposition
EB-PBF	electron beam-powder bed fusion
EBSD	electron back-scattered diffraction
FCC	face-centered cubic
FCG	fatigue crack growth
FE	finite element
G	thermal gradient
HAGB	high angle grain boundary
HCF	high cycle fatigue
HIP	hot isostatic pressing
HT	heat-treated
LCF	low cycle fatigue
LoF	lack of fusion
LB-PBF	laser powder bed fusion
NDE	non-destructive evaluation
Nf	number of cycles to failure
PBF	powder bed fusion
R	solidification rate
Ra	surface roughness
Rε	strain ratio
Rσ	stress ratio
SAGBO	stress-assisted grain boundary oxidation
SR	stress relief
ST	solution treatment
STA	solution treated and aged
VHCF	very high cycle fatigue
Δε/2, εa	strain amplitude
Δσ/2, σa	stress amplitude
ε	axial strain
σ	axial stress
σy	yield stress

1. Introduction

1.1. Additive manufacturing of Alloy 718

Alloy 718, commonly known as Inconel 718 or IN718, is a Ni-Fe-based superalloy, which has presented outstanding mechanical properties at elevated temperatures (up to 650 °C) [1,2]. The elevated temperature tensile and creep properties, along with resistance to thermo-mechanical fatigue, oxidation, and good weldability, render Alloy 718 a suitable material for aero-engines and stationary gas turbine applications [2]. Nevertheless, Alloy 718 has also been identified as a hard-to-machine alloy because of its low thermal conductivity and high hardness, which cause a low removal rate and massive tool depreciation. The combination of high rejection rates, huge material waste, extended lead time, and environmental effects confronts the conventional manufacturing methods, such as casting or forging [3]. In this context, additive manufacturing (AM) technology, particularly powder bed fusion (PBF) techniques, including laser- and electron beam-powder bed fusion (LB-, and EB-PBF, respectively) processes, has been successively used to manufacture the Alloy 718 parts [4].

The AM's computer-aided design (CAD) and layer-by-layer manufacturing strategy [3] allow the technology to avoid conventional design constraints [5], leading to a much higher degree of geometrical freedom and, thus, mass customization of parts. Moreover, AM conserves resources such as lead time, energy, and material that can substantially decrease the cost per part in low production volume compared to the conventional manufacturing processes [6]. Despite its numerous advantages, the AM parts are prone to form process-

induced defects that deteriorate their structural integrity [7], due to AM's unique processing conditions, including high cooling rate, steep thermal gradient (G) [8], high solidification rate (R), and successive thermal cycling. These resultant drawbacks include but are not limited to residual stress, undesired phases, thermal cracks, pores, lack-of-fusion (LoF) defects, and highly-textured columnar microstructures. The pores and harmful phases are stress risers and serve as nucleation sites for voids under tension and initiation sites for fatigue cracks under cyclic loading, leading to premature mechanical failures. Moreover, the highly-textured columnar grain structure perpendicular to, and the LoF defects parallel to the build direction in the PBF processes lead to anisotropic mechanical properties/performance [9,10].

Furthermore, the subsequent addition of the layers on top of each other results in successive thermal cyclic conditions and increased heat accumulations in the upper layers. By adding a new layer, a couple of underlaying solidified layers are subjected to re-melting, leading to changes in the thermal history of the part and subsequently the resulted microstructural features and mechanical performance at different heights of the part [11]. In addition, the thermal history of the parts in PBF also affects the melt pool's geometry, which can change temperature distribution and alter the microstructure, hence the mechanical properties. Therefore, there is a fundamental need to understand the link between the feedstock material, manufacturing process, microstructure, properties, and fatigue performance of the PBF-built parts, particularly those manufactured with Alloy 718; see Fig. 1. The thermal and mechanical post-processing treatments also become crucial to secure necessary and expected properties.

Fatigue-related failures have contributed to approximately 55 % of all failures detected in the aerospace parts [12]. The fatigue failures are still a critical and unresolved issue for metallic parts in general and specifically for adapting the PBF technologies in the industry. While the mechanical properties of conventionally manufactured Alloy 718 are well known and used for part design, deviations of these properties from their conventional counterparts, and significant property variance among themselves, are expected for the PBF-built parts, which are less explored.

The fatigue performance of PBF-built Alloy 718 is particularly important for the qualification and certification of load-bearing parts, and thus, for the adaption of PBF in the industry on a large scale. A decrease in size and number of volumetric and surface defects is expected from the development of new powder manufacturing techniques, the evolution of the new PBF systems, the optimization of the process parameters, and the post-treatments [13,14]. The rough surface of the as-built PBF parts is one of the detrimental factors to fatigue life of AM parts [15]. Improving the surface condition within the manufacturing process or through a mechanical/chemical post-treatment [16] is highly desired for enhanced fatigue life. In the machined surface condition, the volumetric defects in Alloy 718 do not significantly influence fatigue performance.

Despite the rich literature on AM Alloy 718, several research questions regarding their fatigue performance remained unanswered, in which some of them are listed here:

- How and to what extent do the powder features influence fatigue life of Alloy 718 parts?
- How can the macro- and microstructural characteristics influence fatigue life?
- What is the effect of phases, such as δ, carbides, and unwanted non-metallic inclusions on crack initiation and growth?

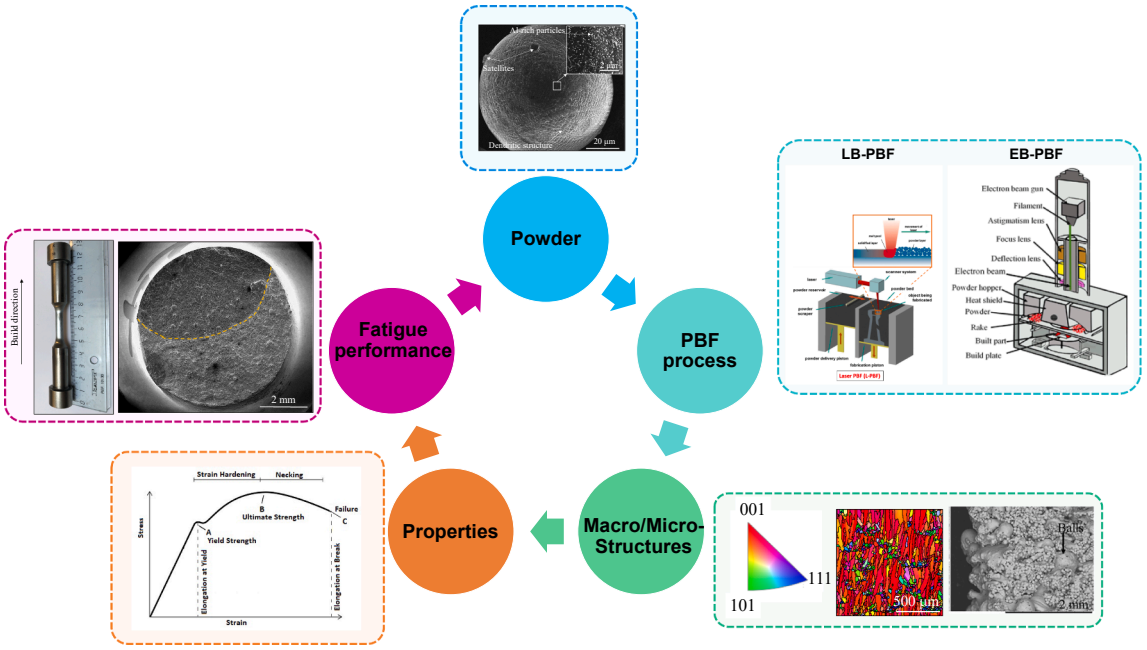

Fig. 1. The relationship between feedstock powder, processes, surface, microstructure, properties, and performance of PBF-built Alloy 718 in fatigue applications.

- How can the process parameters help in pushing the inclusions towards the side surface of the part during manufacturing before the surface removal by machining?
- What is the effect of texture and grain morphology on crack initiation and growth?
- What is the impact of surface irregularities on the fatigue performance of PBF-built Alloy 718?

The following sections aim to address the above scientific questions.

1.2. Structure of the review

This paper presents an extensive review of the fundamental concepts in PBF of Alloy 718 with an emphasis on fatigue performance. The review uses a holistic approach to the relevant topics while being concise and critical, with a primary focus on the key challenges and opportunities in PBF-built Alloy 718. The review allows both skilled and fresh researchers entering the field to be informed of various critical aspects of PBF, and their connection to fatigue life of the Alloy 718 parts. The paper is structured so that Section 2 is devoted to the influence of the feedstock powder characteristics on fatigue life. Section 3 is dedicated to the factors that can affect the bulk and surface conditions of the part, and eventually, its fatigue performance. Section 4 presents the progress in understanding the fracture mechanisms of the PBF-built Alloy 718 parts. In Section 5, the potential future research in the field of PBF and fatigue of Alloy 718 are discussed. All the sections begin with a general background of the intended subject.

Despite the growing interest in the PBF of Alloy 718, a comprehensive understanding of the material from the experimental methodologies to the fundamentals and of their fatigue performance in service environments is lacking. There are currently review papers on various aspects of the mechanical properties of different materials in AM [17-22]. Nonetheless, there is no review addressing the effect of the feedstock powder, microstructure, and surface characteristics on the fatigue of PBF-built Alloy 718. This review adopts a thorough approach besides the timely nature of capturing the growth in research activities in recent years. The research trend in the field of fatigue of PBF-built Alloy 718 is reviewed, identifying the present and future research gaps and research directions in the field. Finally, this paper has primarily concentrated on fatigue of Alloy 718 built via the LB- and EB-PBF processes.

2. Feedstock powder

2.1. Alloying elements and phases

Alloy 718 contains >15 major and minor alloying elements (see Table 1), each of which has a critical role in the final properties of the alloy. The alloying elements, such as Ti, Al, and Nb, facilitate the formation of the strengthening precipitates, such as γ'-Ni_3(Al,Ti), and more importantly, γ''-Ni_3Nb, with the latter being the principal strengthening phase in Alloy 718. Various features of these precipitates (i.e., size, distribution, volume fraction, and morphology) are typically controlled by an aging heat treatment, which are discussed in Section 4 and extensively reviewed in [23]. Moreover, elements such as C, Nb, Ti, Cr, and Mo contribute to the carbide formation, controlling grain size and hindering grain boundary sliding at elevated temperatures. In addition, Al and Cr enhance high-temperature corrosion resistance [24]. A summary of the typical phases found in PBF-built Alloy 718 is given in Table 2. The volume fraction and distribution of the phases/precipitates, which depend on the thermodynamics/kinetics of the manufacturing process, govern the behavior of the alloy in service. Several phases, such as γ'' (ordered $D0_{22}$ BCT crystal structure) usually with disc-like or oblate spheroidal morphology, γ' (ordered $L1_2$ FCC crystal structure) with spherical/cuboidal morphology, needle-shaped δ (ordered $D0_a$ orthorhombic crystal structure), globular or blocky shaped MC-type carbides, and eutectic Laves phase $(Ni,Cr,Fe)_2(Nb,Mo,Ti)$ (hexagonal crystal structure) with irregular morphology have been frequently reported in PBF-built Alloy 718 [25,26].

γ'' is the key strengthening precipitate in Alloy 718, whereas δ, as an incoherent phase with the γ matrix, does not contribute to strengthening. δ indirectly impacts the precipitation strengthening by depleting Nb, and directly affects the cracking susceptibility during fatigue. The characteristics of δ (e.g., size, volume fraction, and distribution) are generally controlled through proper thermal post-treatments leading to some benefits to the microstructure and mechanical properties. The δ phase frequently resides at the grain boundaries, and if it has the proper size, grain size control and the prevention of notch sensitivity, which is a major concern for the EB-PBF of Alloy 718 during the service life, can be achieved [31,32].

Interdendritic segregation of Nb in the form of hexagonal Laves phase found in PBF-built Alloy 718 (mainly LB-PBF) adversely affects the mechanical properties, because the phase serves as a crack initiation site and an easy crack growth path [33]. Basically, segregation of Nb and the subsequent formation of the Laves phase can cause liquation cracking in Alloy 718, which typically forms at the last stage of solidification via a chemical reaction from γ to Laves [34]. Because of the sluggish precipitation of γ'', Alloy 718

Table 1
Chemical composition of Alloy 718 (all in wt%) [27].

Element	Ni (+Co)	Cr	Fe	Nb (+Ta)	Mo
	50.00–55.00	17.00–21.00	Bal.	4.75–5.50	2.80–3.30
Element	**Ti**	**Al**	**Co**	**C**	**Mg**
	0.65–1.15	0.20–0.80	Max 1.00	Max 0.08	Max 0.35
Element	**Si**	**P**	**S**	**B**	**Cu**
	Max 0.35	Max 0.015	Max 0.015	Max 0.006	Max 0.30

Table 2
Typical phases formed during PBF of Alloy 718 [28-30].

Phase	Label	Crystal structure	Formula	Solvus temperature (℃)	Description
Solid solution matrix	γ	Cubic (FCC)	(Co,Cr,Ni,Fe)-based	1260–1364 (liquidus)	Strengthening by elements with larger atomic diameters than Ni
Intermetallic	γ'	Cubic (FCC) (ordered $L1_2$)	$Ni_3(Ti,Al)$	850–910	Coherent with γ; spherical, globular, blocky, or cuboidal shape depending on the γ/γ' lattice mismatch
	γ''	Tetragonal (BCT) (ordered $D0_{22}$)	Ni_3Nb	910–940	Semi-coherent with γ; metastable; disc or plate shape
Topographically close-packed (intermetallic)	δ	Orthorhombic (ordered $D0_a$)	Ni_3Nb	1005–1020	Incoherent; stable; needle or plate shape
	Laves	Hexagonal (C_{14})	$(Ni,Cr,Fe)_2(Ti,Nb)$	1163	Irregular shape
Carbide	MC	Cubic (B_1)	(Nb,Ti)(C,N)	1260–1305	Globular or blocky shape

typically shows outstanding weldability (e.g., reduced strain age cracking susceptibility) and manufacturability [30]. Moreover, different thermal post-treatments were applied to homogenize the elemental distribution in the interdendritic regions and facilitate recrystallization to resolve the anisotropic mechanical properties [35-37].

Considering the high cooling rate in the PBF processes, especially LB-PBF (up to 10^7 K/s), the formation of metastable precipitates is facilitated, as presented in Fig. 2a. While Fig. 2b does not differentiate γ'' from δ as they have a similar composition, it is noted that upon exposure above 650 °C, metastable γ'' converts slowly to the incoherent but stable δ [38] (this is why Alloy 718 must be used below 650 °C in the target application). Fig. 2c presents the segregation of critical alloying elements in Alloy 718 during solidification. The black dash-dot line shows the changes in the liquid fraction (f_L) with respect to temperature. The segregation of Nb, Mo, and Ti happens in the liquid phase. Fig. 2c presents four stages of the development of liquid chemistry during solidification with respect to temperature. For Nb, the stages include i) monotonic rise (between melting temperature and 1178 °C) having a high slope, ii) monotonic rise (between 1178 and 1145 °C) having a short slope, iii) monotonic rise having a short slope (between 1145 and 1142 °C), and iv) monotonic fall (between 1142 and 1140 °C). Stage (i) is mainly linked to the formation of the γ and γ' phases during the equilibrium condition of solidification. Stages (ii), (iii), and (iv) are because of the formation of the Laves, σ, and γ'' phases, respectively. The amount of Nb in the liquid phase presents a significant increase with solidification, particularly in stage (i).

2.2. Powder characteristics

The Alloy 718 powder for the PBF processes is usually manufactured via gas atomization, plasma atomization, or plasma-rotating electrode process (PREP) in an inert environment, such as argon [40]; see Fig. 3. Regardless of the powder manufacturing process, the morphology of the powder particles is one of the essential parameters on the mechanical properties because the powder morphology can significantly affect the spreadability (or flowability), thermal and electrical conductivity, and the powder bed packing density. All of which influence the penetration depth of laser or electron beam [41], which is associated with the formation of the melt pools. The melt pool geometry (i.e., depth and width) is a key factor in determining the level of defects and even the solidification mode in the PBF processes. If the melt pool depth becomes larger than the layer thickness, it can lead to re-melting or partial melting of the underlying layers, avoiding the risk of the LoF defect formation [42]. Therefore, the changes in the penetration depth of the heat source can result in quality issues that include the formation of different types of defects, e.g., balls and voids within a layer, which eventually affects the fatigue performance [43,44]. Moreover, the width of the melt pools, which affects the overlap zone between two adjacent melt pools, is a critical factor too, which affects the amount of the un-melted powder particles locked between them.

The thermal and electrical conductivity of the powder bed, which are critical factors in EB-PBF, are collectively determined by powder composition [48] and the gaps and connections among the powder particles, affecting the packing density [40,46]. The packing density, in turn, depends on the powder morphology and the associated spreading dynamics. A low packing density can lead to gaps in the powder bed, resulting in an unstable and noncontinuous melt flow, which leads to the formation of the defects [47]. Moreover, the packing density of the powder is a function of its flowability (or spreadability), which is dictated by the shape and size distribution of the powder particles. For instance, the spherical powders flow better than the particles with an irregular shape because of the low likelihood of interlocking and the free rotation of the particles [48].

The powder size distribution is also a significant parameter in controlling the size of the pores. Fine satellite particles connected to coarse powder particles can change the packing density by lowering flowability because of increased mechanical interlocking [49]. For LB-PBF, the gaps will then form gas bubbles within the melt pool and, if there is insufficient time for the bubbles to escape, gas entrapped pores will form. It is worth noting that the number of recycling can significantly improve powder flowability [50]. It is reported that the recycled powder typically contains a decreased number of very fine particles and agglomerates, leading to a more uniform powder distribution on the build plate and fewer and smaller defects in the specimens, hence improving fatigue life [51].

The powder morphology of Alloy 718 is typically characterized by satellites and a dendritic structure; see Fig. 4. Such features are commonly seen after powder recycling (e.g., Fig. 3c), if not present in the fresh powder. Nanoscale Al-rich oxides can be observed on the powder surface [52]. A low level of oxygen (around 5 ppm) in the environment (during either powder or part manufacturing) is

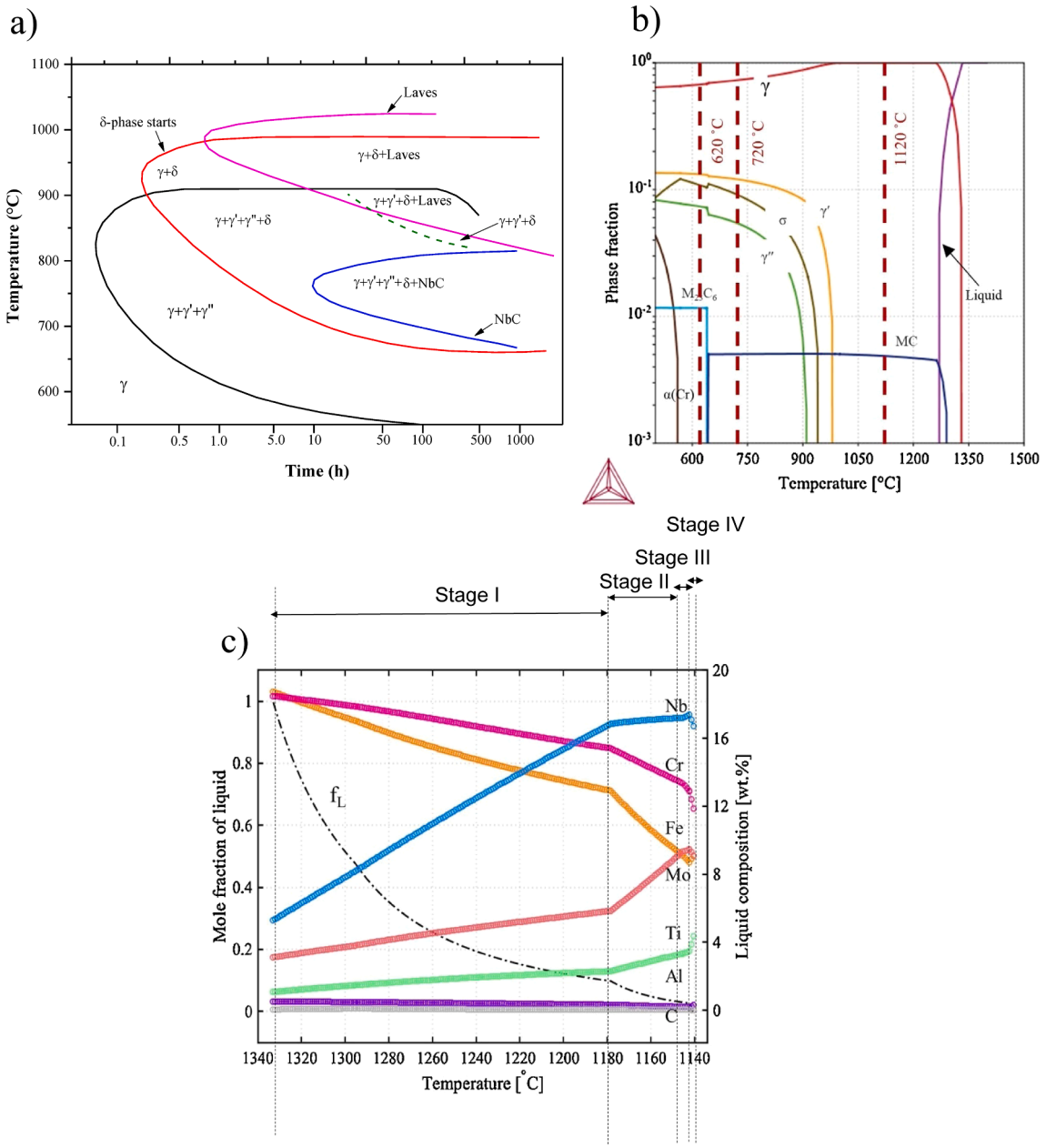

Fig. 2. (a) Time-temperature-transformation (TTT) diagram for Alloy 718 (b) The equilibrium step diagram generated using the TCNI8 database in Thermo-Calc, CALPHAD and (c) Nb, Mo, and Ti segregation and Cr, Fe depletion in the liquid at the growth front during solidification estimated by the Scheil-Gulliver model, showing substantial segregation. δ was ignored in the calculations [39]. Reprinted with permission from Elsevier.

enough to facilitate the nucleation and growth of the oxides (e.g., Al-rich oxide) on the surface of the powder particles [53]. The oxygen level of the powder particles can exceed 100 ppm during the atomization process, even using argon gas [54]. The powder handling steps during recycling, such as sieving or powder recovery (in the case of EB-PBF) that occur in ambient air, and the multiple exposures of the powder to the high-temperature build chamber environment, can lead to the formation of the Al-rich oxides on the recycled powders [55]. A thin ALB-rich oxide with a thickness of around 30 nm was reported on the surface of the fresh powder particles, which grew up to 200 nm after 14 times of usage and recycling [53]. The Al-rich oxide is extremely deleterious because it serves as the nucleation site for other undesired non-metallic inclusions, such as TiN, during the solidification stage in PBF.

The primary precipitates observed in the cross-section of the recycled Alloy 718 powder were the needle-shaped δ phase [52]. δ in the powder is not typically seen as a critical issue, as the melting point of Alloy 718 (around 1360 °C) exceeds the dissolution temperature of δ (around 1020 °C) [56].

The non-metallic inclusions were also observed in the powder particles. The size range of the non-metallic inclusions was 1–10 μm.

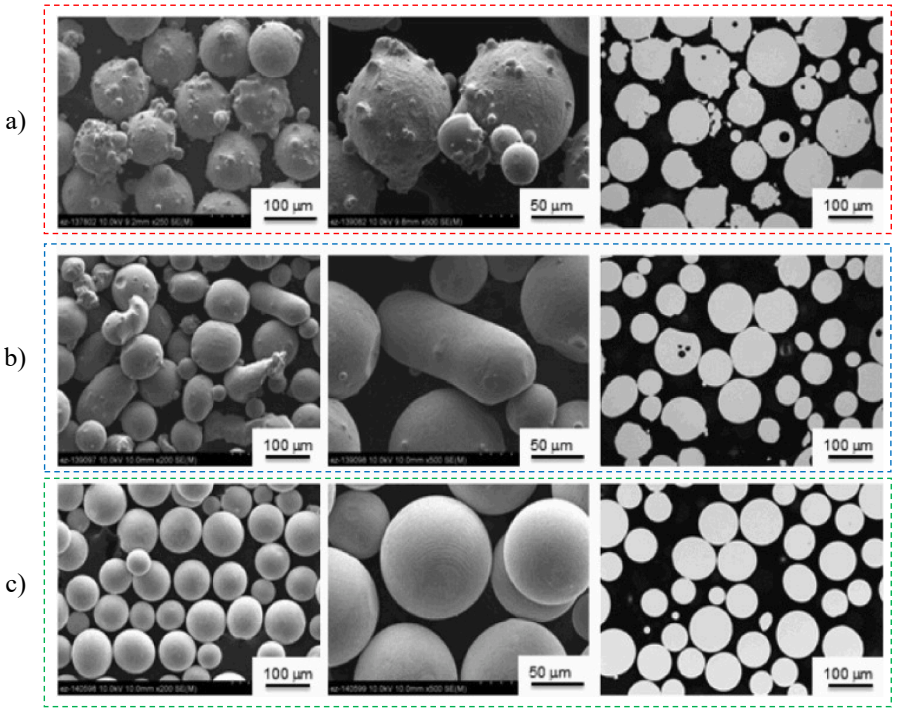

Fig. 3. Comparison of the Alloy 718 powder particles, a) gas atomized, b) plasma atomized, and c) from the plasma rotating electrode process [45]. Reprinted with permission from Elsevier.

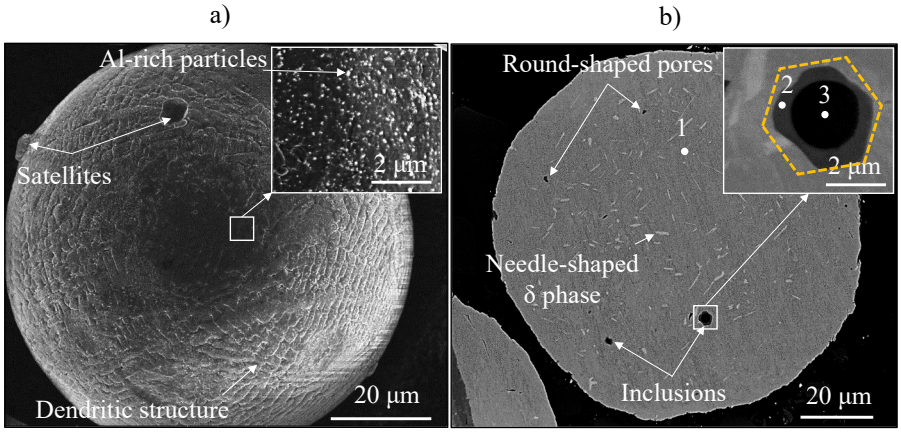

wt%	C	N	O	Al	Ti	Cr	Ni	Nb	Mo	Fe
Point 1	-	-	0.3	0.7	1.3	19.4	55.4	5.2	2.3	20.6
Point 2	6.8	24.3	1.2	-	50.0	6.8	0.9	10.0	-	-
Point 3	-	-	52.1	38.7	0.7	7.9	-	0.6	-	-

Fig. 4. A) Morphology, and b) cross-section of a recycled alloy 718 powder particle. the point analysis by energy dispersive x-ray spectroscopy (eds) in the matrix, the surrounding and core of a non-metallic inclusion are highlighted as points 1, 2, and 3, respectively. the signals from the light elements, such as c and n are only for a qualitative assessment [52]. Reprinted with permission from Elsevier.

The TiN inclusions showed a hexagonal morphology with sharp corners, shown in Fig. 5, which can be detrimental to fatigue life [57,58]. Because of the high stability of the inclusions, they remain intact during melting and form clusters of inclusion during solidification [59]. The size of the clustered inclusions was in the range of 10–400 µm [52]. The low cycle fatigue (LCF) tests performed on EB-PBF of Alloy 718 verified the sensitivity of the crack initiation to the agglomerated inclusions, mainly when the grains are finer than the size of the clustered inclusions [60].

Parameter	Power, W	Speed, mm/s	Hatch spacing, µm	Modification
1	285	960	110	Nominal parameter
2	285	960	150	Increased hatch spacing
3	285	960	80	Decreased hatch spacing
4	300	1200	80	Increased cooling rate
5	200	400	180	Decreased cooling rate

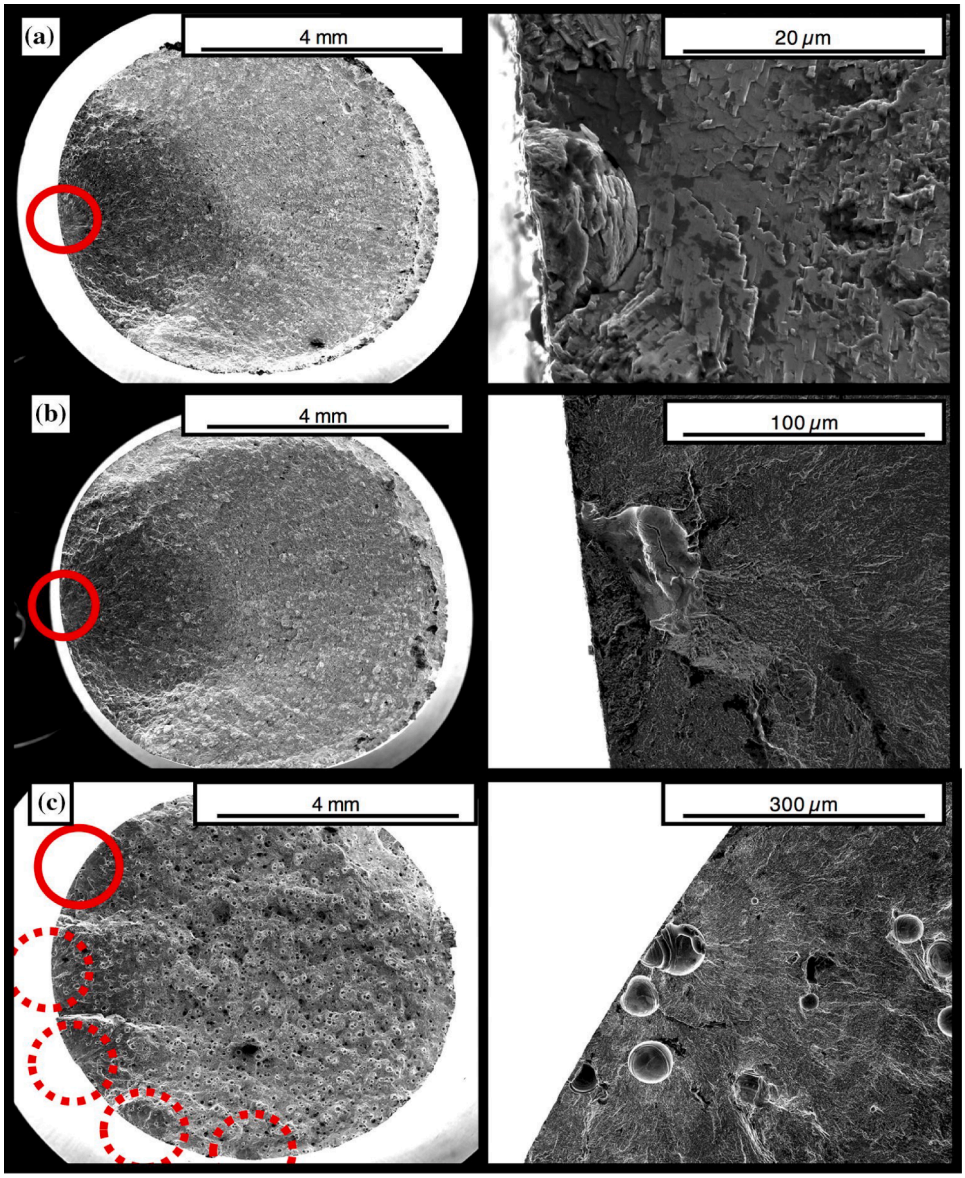

Fig. 5. The process parameters and selected fracture surfaces at two different magnifications for the process parameter sets a) 1, b) 2, and c) 5, presenting the frequency of the crack initiation sites (marked in the red circles) at low magnification and the exact locations of the crack initiation sites at high magnification [100]. Reprinted with permission from Elsevier. (For interpretation of the references to color in this figure legend, the reader is referred to the web version of this article.)

3. Process parameters

Research on Alloy 718 built via LB- and EB-PBF has been extensively growing in recent years [11,15,39,43,61-63,63-71]. In both processes, a part is manufactured by melting selected regions of powder layers using an energy source of electron beam or fiber laser [72,73]. The beam-material interactions cause the powder to be melted and form the melt pool, which then rapidly solidifies and cools down. After the entire layer is consolidated, the building platform moves down by a predefined distance (i.e., layer thickness) before the fresh powder for the new layer is spread. These steps are repeated until the whole part is manufactured [74]. In the end, the unmelted powder is often recovered, sieved, and recycled (sometime with the addition of fresh powder with an appropriate ratio) for future runs. The parts are then removed from the build plate and post-processed (i.e., thermal and mechanical post-treatment) as needed [75]. Despite several similarities between LB- and EB-PBF, there are many inherent differences between the processes [76]. When electrons hit the powder surface in EB-PBF, electron charging of the powder particles leading to smoking is a major challenge. EB-PBF mainly consists of multiple steps, including pre-heating 1 (to prevent smoking), pre-heating 2 (to improve powder sintering), melting, and post-heating (to balance energy), whereas LB-PBF typically only involves melting. In EB-PBF, pre-heating the layers is mandatory; however, LB-PBF does not require this step because electrostatic charging is not a concern in LB-PBF. In addition, while there is no standard or a comprehensive study, the feedstock powder particles used for EB-PBF have been typically coarser than LB-PBF. Using coarser powders in EB-PBF was motivated primarily by safety and a desire to avoid the risk of explosion caused by electrical charging (during either the process or post process), which was not the case in LB-PBF. Utilizing fine powder particles and accordingly small layer thicknesses in LB-PBF, which compensates for the materials' low laser energy absorption, have significantly enhanced the surface quality of the parts [77].

The scan speed is higher in EB-PBF than LB-PBF, as the electrons are directed using electromagnetic lenses in EB-PBF, while the laser beam in LB-PBF is mechanically directed using mirrors [73]. Moreover, electrons can carry a higher amount of energy than photons. One of the most significant advantages in EB-PBF is the use of vacuum, thereby protecting sensitive alloying elements from probable oxidation. In contrast, the entrapment of gas pores originating from the process gas can be a challenge in LB-PBF. It is pertinent to state that generally, vaporization of low melting point constituents and subsequent formation of pores is a major concern in the PBF processes [78]. However, in the case of EB-PBF, it is reported that the vaporization pores might not form easily [79]. LB-PBF is performed at a much lower bed temperature around 80–300 °C compared to EB-PBF (above 950 °C for Alloy 718) leading to a higher cooling rate and thermal gradient in the former process. Therefore, as-built LB-PBF lacks the typical strengthening precipitates found in Alloy 718 and contain a higher level of residual stress, which demand performing an appropriate post-heat treatment.

Both PBF processes (i.e., LB- and EB-PBF) result in extreme thermal gradients and subsequently the formation of non-equilibrium structures; the effect of each on the fatigue performance needs further exploration [76,80-82]. For instance, the very high cooling rate and thermal gradient that occur during LB-PBF can lead to the formation of cellular structures with high dislocation density and chemical segregation at the cell boundaries, which can significantly alter the mechanical properties [9,83-86]. In general, the PBF-built parts experience intricate non-equilibrium phase transformations during the process [87]. The efficacy of standard heat treatments designed for wrought Alloy 718 on these non-equilibrium phases, microstructures, and in turn, the resulting fatigue performance must be understood for the broad use of the alloy in industrial applications.

There are several process parameters that determine the energy input (E) ($E = \frac{\text{beam power}}{\text{layer thickness} \times \text{scan speed} \times \text{line offset}}$) for melting the powder bed, including beam power (i.e., beam current × accelerating voltage in EB-PBF), scan speed, the distance between adjacent melt lines (line offset in EB-PBF, and hatch spacing/distance in LB-PBF), and layer thickness. The generated microstructure resulted from altering the process parameters can affect the fatigue performance. It was shown that the linear energy input impacts the size and morphology of the melt pools, and eventually, the final microstructure in LB-PBF [88]. A high linear energy input leads to a large melt pool in LB-PBF, whereas a low linear energy input leads to the formation of shallow and small melt pools resulting in an equiaxed grain morphology with a weak texture [89,90]. In the latter, less segregation of alloying elements, lower content of the Laves phase, and greater precipitation of γ' and γ'' after aging were reported. However, the low linear energy input might increase the level of pores and reduce the part density, e.g., due to the insufficient fusion between melt tracks [88].

Several scanning strategies to determine beam path during the melting of a layer have been studied, influencing the microstructure, residual stress distribution, and the defect distribution in the parts [91-95]. The sensitivity of the microstructure to the scanning strategy and beam parameters helped to obtain location-specific microstructure [96]. For instance, functionally-graded Alloy 718 was produced via LB-PBF [97] with grains of different sizes in specific locations. The variations in microstructure had a significant impact on the local mechanical properties. Under uniaxial loading, the coarse grains resulted in the highest deformation and final fracture because of the easy movement of dislocations that triggers the onset of plasticity [97]. Moreover, the complicated melting, re-melting, and cooling steps during LB-PBF inhibited complete precipitation of γ" and γ', and the as-built microstructure contained segregation, non-equilibrium phases, and residual stress [84].

As defect formation has critical effects on fatigue life, the optimization of the process parameters is highly essential to minimize the level of defects. The relationship between the primary process parameters and microstructure in LB-PBF of Alloy 718 was investigated by Sheridan et al. [14] to establish a fatigue life prediction theme. The results indicated a high fatigue life for regions of high density (with fine pores). A low fatigue life in regions of both extremely high and low energy inputs was found due to reduced density (with coarse pores). According to Yang et al. [98], the fatigue cracks can be initiated from the pores in a mechanism known as *pore-assisted crack initiation*. The round-shaped pores form due to the uniform distribution of pressure inside the pore. The pressure is developed by the entrapped argon gas used during powder manufacturing. In LB-PBF, There might be gas residue already in the feedstock powder particles sourced from the gas atomization process [99]. Moreover, the inert gas used in LB-PBF can fill the spacings among the powder

particles. When a high-energy laser beam hits the powder bed, the powder particle quickly starts melting from top to bottom of the powder. The processing gas (e.g., argon) is, therefore, entrapped in the form of bubbles in the melt pools. The gas buoyancy and turbulence in the molten metal facilitate the migration of the bubbles due to the fluidity of the melt [93]. The majority of the fine bubbles are merged and form coarse bubbles or pores. Upon solidification, the fluidity of the molten metal quickly decreases; therefore, the entrapped bubbles fail to solidify in the form of pores.

The influence of the process parameters, including beam power, scan speed, and hatch spacing, on the fatigue performance of LB-PBF-built Alloy 718 was investigated [100]. Altering the process parameters did not affect the structure of the precipitates in the alloy. An increase in the hatch spacing from 80 to 180 μm led to a high level of defects. A combination of low beam power, low scan speed, and large hatch spacing (i.e., 285 W, 400 mm/s and 80 μm, respectively) also increased defects, which significantly reduced fatigue life [100]. Fig. 5 shows the process parameters and the fracture surfaces of the selected sets of the process parameters. The process parameters (set 1) showed a small pore on the surface, while the fracture surface for set 2 showed an LoF defect as the crack initiation site. Set 5 led to multiple crack initiation sites at the surface and sub-surface regions owing to many pores in the material.

3.1. Build layout and orientation

The effect of build layout on fatigue performance of EB-PBF of Alloy 718 was investigated [101]; see Fig. 6. The influence of the part location on the microstructure was insignificant; therefore, the microstructure evolution was excluded from the observed scatter in the fatigue results related to the part location. The building layout affected the surface topography and, consequently, fatigue life. The parts in the front half of the build plate (zone II) showed superior LCF life. Meanwhile, the parts built at the outer regions of the build plate showed high hardness values; however, a closer look at the hardness values confirmed that only two samples (colored in white) had very low hardness values. Therefore, it can be indicated that the building layout did not have a significant effect on hardness. The

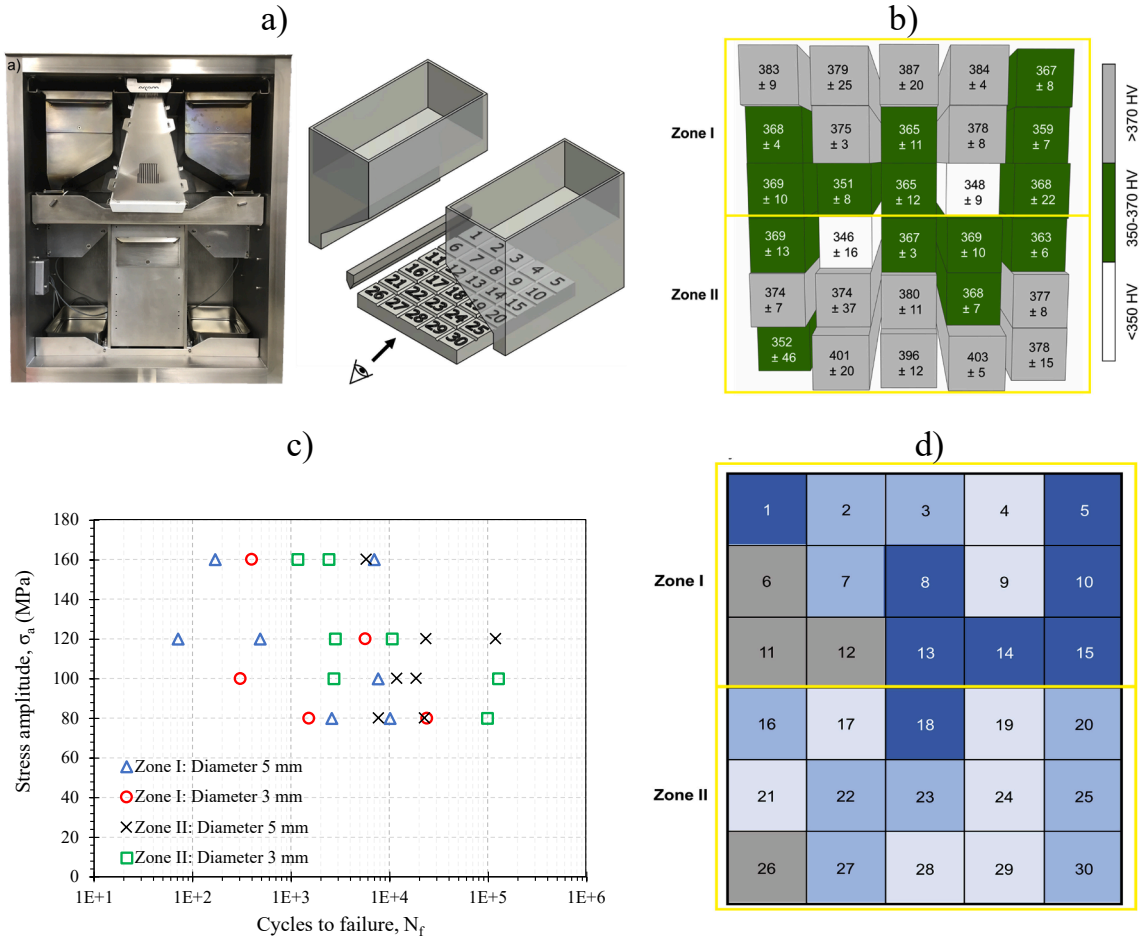

Fig. 6. A) Arcam a2x machine and schematic view of segmentation of the build platform, b) the link between the hardness values and the positions on the building platform, c) stress–cycles to failure curves, and d) color map showing the fatigue performance (dark blue: lowest n_f, light blue: highest N_f) [101]. Reprinted with permission from Elsevier. (For interpretation of the references to color in this figure legend, the reader is referred to the web version of this article.)

plate-pile-like stacking surface features observed on the as-built samples were found extremely deleterious in fatigue. The location of the parts did not notably influence the relative density of the parts on the build platform. Therefore, the pores were resulted from the individual non-uniformities within distinct part volumes during EB-PBF.

High cycle fatigue (HCF) of Alloy 718 built via LB-PBF was systematically studied with the possibility to track the position of the fatigue failure in parts built vertically and horizontally on the build plate [15]. The crack initiation site was at an azimuthal location aligned with the edges of the scanned islands in LB-PBF. A clear failure location in reference to the powder bed was observed as the contour scan strategy followed a similar pattern (not random) in each layer. Small and circular features (in singular or closely-spaced form) found in the contour region acted as the fatigue crack initiation site. No apparent variation between the S—N curves was found for a specific combination of stress ratio (R) and surface condition. The S—N curves were also similar for the vertical (0°) and angled (30°) parts with the as-built surfaces. The horizontal (90°) parts could not be built without the support structure, therefore testing the horizontal parts in the as-built surface condition was impossible. However, the S—N curves for the horizontal and vertical parts with machined surfaces were found almost identical at the stress ratio of 0.1.

3.2. Part's geometry

The qualification or certification practices in the aerospace industry currently depend on the building block concept (e.g., see common test part design for various fatigue experiments in Fig. 7) and a statistical approach using a huge mechanical test data to evaluate variability in the material and process parameters [102]. The building block concept is costly and time-consuming and involves testing at several steps, starting from material property examination testing and ending with full-scale verification testing. This approach might often be impractical for qualifying the PBF-built parts known for their high variability in the process and process parameters. Thus, more robust and cost-effective qualification methods might need to be developed to understand better and utilize

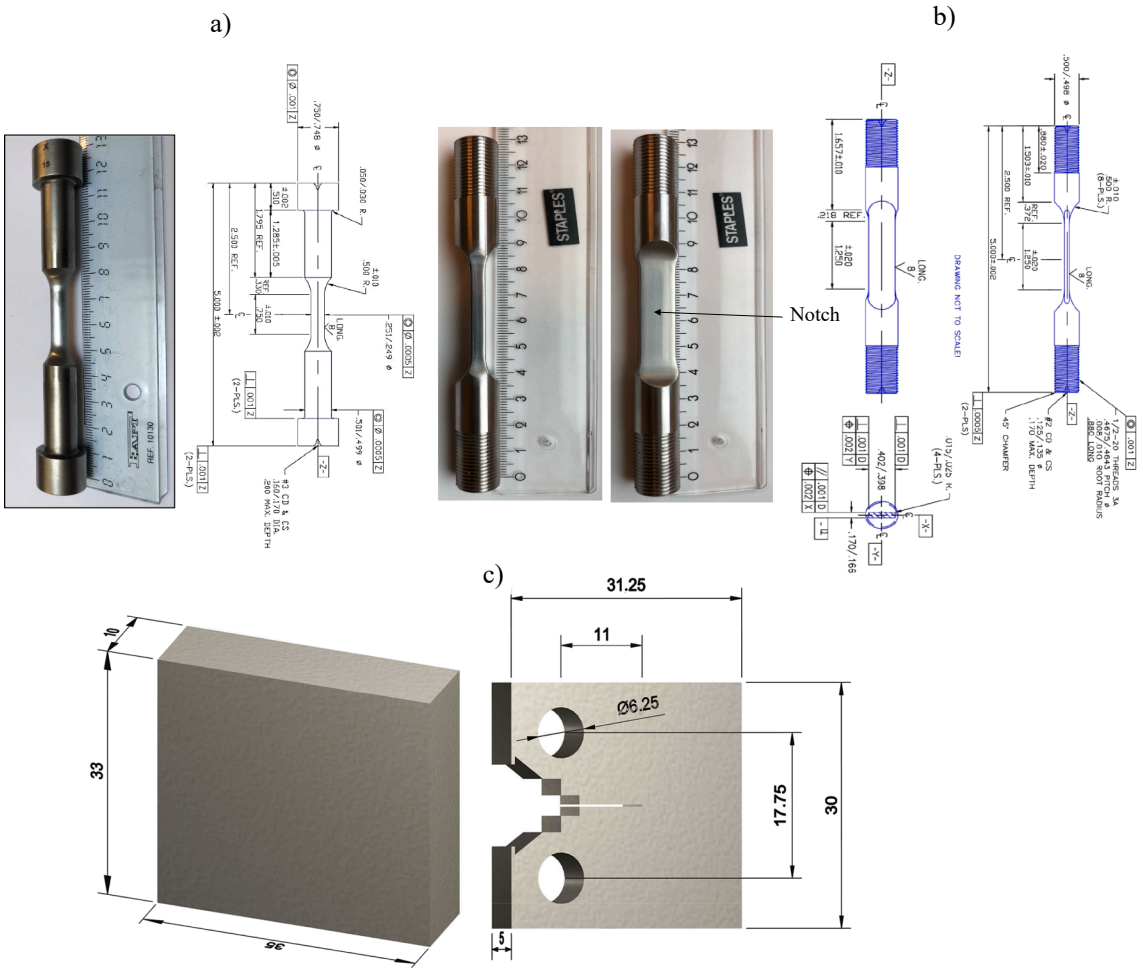

Fig. 7. Examples of typical fatigue test parts, a) button-head test part used in the low and high cycle fatigue (LCF and HCF) tests [52], b) k_b-type test part utilized in the fatigue crack growth (FCG) test, and c) compact tension (CT) test part utilized in the fatigue crack growth (FCG) test [104]. Reprinted with permission from Elsevier.

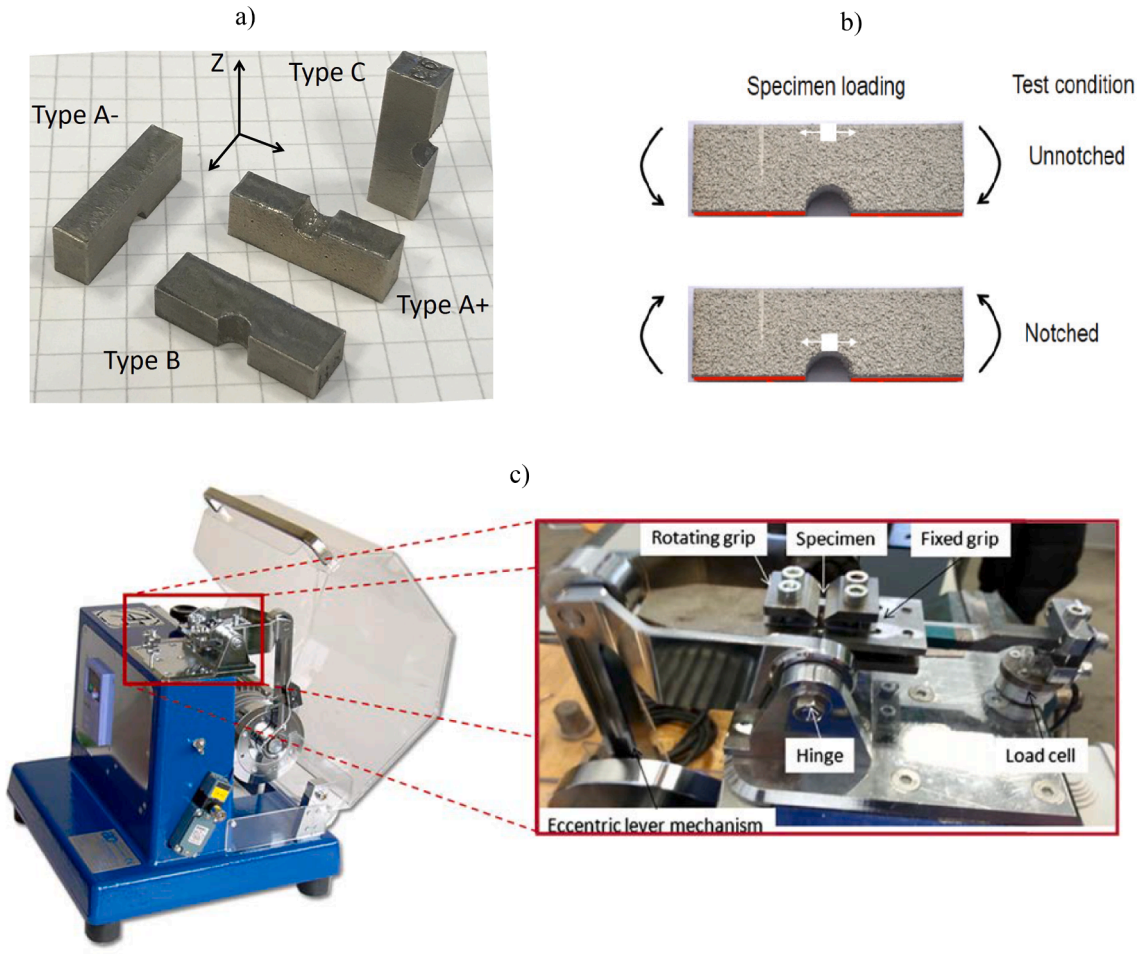

Fig. 8. A non-standard (miniature) part used in the fatigue test, a) different orientations, b) loading direction with respect to the notch, and c) cyclic plane bending fatigue testing machine with the details of mini part in the grips [103]. Reprinted with permission from Elsevier.

the PBF-built parts [103].

Nicoletto [103,105] proposed a new fatigue test condition that uses non-standard (i.e., miniature) parts; see Fig. 8. Apart from the economic benefit, testing the pre-defined material surface is another advantage of the miniature part geometry. Thus, parts can be readily oriented in relation to the build direction to study the anisotropic fatigue behavior. A primary screening phase using the small parts allows shortlisting of the process parameters and the test conditions for a given material.

The thickness of the manufactured parts can also affect fatigue life. In as-built LB-PBF Alloy 718, the thinner parts exhibited a more prolonged high-temperature (at 650 °C) fatigue life than the thicker parts; however, the machined parts showed an opposite behavior [106]. Such behavior was mainly linked to the variation in the thickness-dependent microstructure and surface roughness, whereas stress distribution did not play a significant role. The grains were found coarser in the thinner parts. The primary reason was the change of thermal history during printing, influenced by the inter-layer time interval (i.e., the time taken for the laser to finish one layer and start to melt the next layer). The thicker parts with a longer inter-layer time interval experienced a higher cooling rate, resulting in a finer grain structure. The thin parts showed a stronger $\langle 001 \rangle$ texture compared to the thick parts, because of a much higher thermal gradient in the thin parts. Moreover, the surface of the thick parts was significantly rougher than that of the thin parts due to the fact that a higher total energy requirement in the former parts enhances the sintering phenomenon by providing more energy to sinter more powders from the surroundings, resulting in the rougher surface of the thick parts. In the machined specimens, in which the surface condition was similar, the grain orientation mainly dictated fatigue life [106]. It was reported that the grains with $\langle 001 \rangle$ crystallographic orientation has the lowest Young's modulus, while the grains with $\langle 110 \rangle$ and $\langle 111 \rangle$ crystallographic orientations have larger Young's modulus. The very low measured Young's modulus was linked to the $\langle 001 \rangle$ crystallographic orientation. Regarding the sensitivity of accumulative plastic strain to grain orientation, thin parts were subjected to a greater accumulative cyclic plastic strain than thick parts for a given stress amplitude, resulting in a shorter fatigue lifetime.

Several research has explored the lattice structures that consist of several linked unit cells. However, the stress/strain distribution in the lattice structures is highly complicated; therefore, the evaluation of damage accumulation and understanding the failure mechanisms are greatly challenging. Therefore, single-unit cells need to be initially studied to establish the property-failure linkage.

Persenot et al. [107] reported that struts have distinct mechanical properties based on their orientation to the build direction. Kotzem et al. [108] used a newly designed Alloy 718 strut part manufactured via EB-PBF to investigate the damage tolerance. The surface roughness, as the most severe surface irregularity of the struts, was shown as the primary reason for failure. A drop in the cross-sectional surface area resulted in a microstructural change from highly-textured columnar grains to a mixed grain morphology containing both equiaxed and columnar grains. The change in the microstructure and enhanced defect content in the struts and transition regions did not provide a harmful influence on the fatigue performance of the struts. The localized deformation of single struts resulted in a localized increase in temperature, associated with the dissipated energy due to plastic deformation [108].

4. Microstructure and surface condition

There are two distinct regions in the PBF-built parts, i.e., the bulk (also known as hatch) and the skin (also known as contour) regions, each of which substantially impacts fatigue life. Surface conditions are primarily related to the contour region process parameters; however, the microstructure of both hatch and bulk is a factor that can dictate several mechanical properties, yield, ultimate tensile strength, and fatigue performance [109]. Several studies have investigated the microstructure of PBF-built Alloy 718 [26,35,39,61,70,97,110-120]. It is essential to know whether the entire process-microstructure-properties-performance linkage results from a deliberate alteration or an intrinsic geometrical effect [121]. It should be emphasized that many of the previous fatigue studies only implemented the process parameters recommended by the machine suppliers and often did not report the full set of the process parameters used for manufacturing. Moreover, the time, temperature, and cooling rate of the thermally post-treated material are not entirely disclosed, which makes it challenging to reproduce the same characteristics and fully understand the process-microstructure-properties-performance relationship.

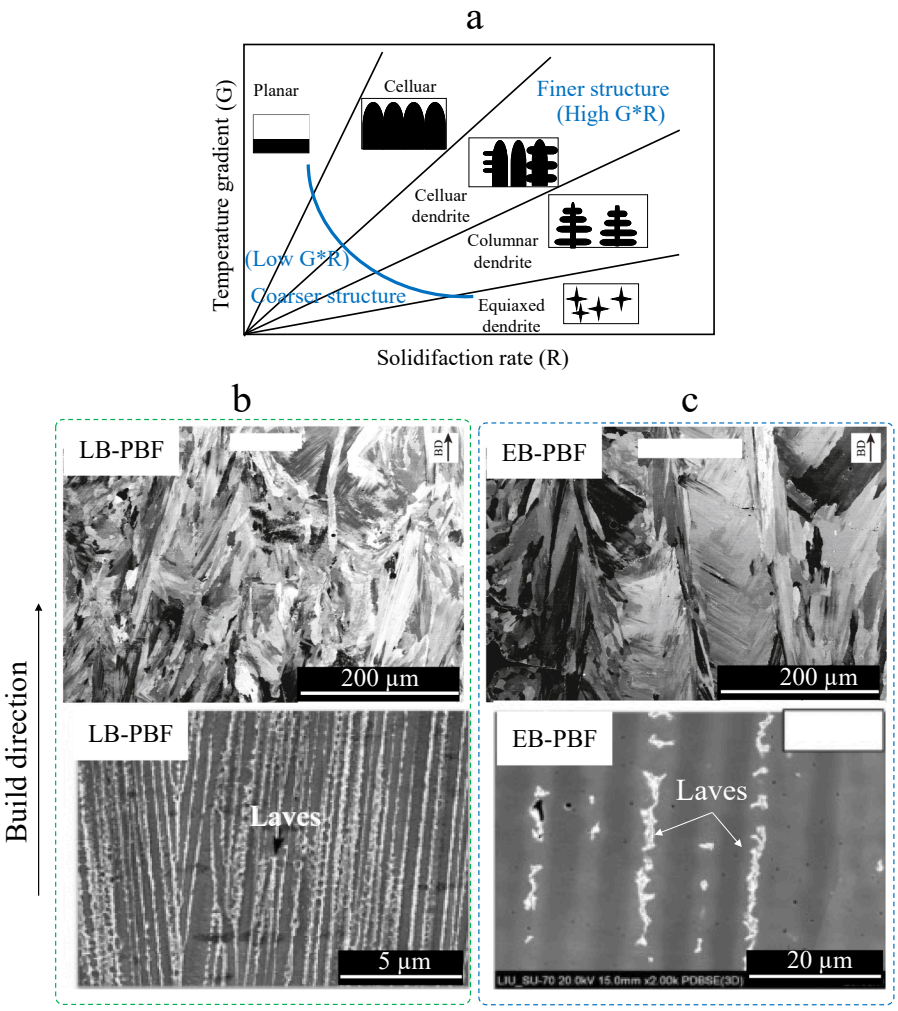

Fig. 9. Effect of G, R, and cooling rate (T) on the solidification modes [129], the SEM images of the microstructure of a) LB-PBF-built, and b) EB-PBF-built Alloy 718 [113,130,131]. Reprinted with permission from Elsevier.

Two major solidification parameters, including thermal gradient (G) and solidification rate (R) are a function of process parameters in the material which during any PBF processes affect the solidification mode (i.e., planar, cellular, columnar-dendritic, or equiaxed-dendritic) and grain morphology, whereas the cooling rate (T) affects the size of the grains, see Fig. 9a [122]. The liquid–solid influences the microstructure, and solid–solid (e.g., γ'' to δ at above 700 ℃ [123]) phase transformations during the complex thermal history resulted from PBF. Fig. 9b-c shows the typical microstructure of as-built LB- and EB-PBF built Alloy 718. Both the LB- and EB-PBF materials had the columnar grains spanned multiple build layers, with interdendritic segregations. The columnar grains along the build direction and the equiaxed grains perpendicular to the build direction indicated the formation of the rod-shaped elongated grains. Because of the very high cooling rate in LB-PBF, the grain structure was much finer than that of EB-PBF. The columnar grains were expanded within several layers because of the partial re-melting of the underlaying layers (i.e., epitaxial growth). As illustrated in Fig. 9b-c, the elemental segregation in PBF-built Alloy 718 could result in the formation of the Nb and Mo-rich phases, such as Laves phase, carbide, δ phase, or even in the form of Nb-rich regions, like interdendritic regions, depending on the part's localized thermal history, which is a function of local cooling rate [124]. It is reported that via very high cooling, segregation of Nb, and the formation of the Nb-rich phases can be avoided. However, due to the lack of *in-situ* annealing, a high level of the Nb-rich phases is common in LB-PBF; the Laves phase was commonly observed in the top layers of the part (up to around 2 mm) [125]. Similarly, the last few layers in EB-PBF showed the Laves phase [113,114], whereas the phase was dissolved in the rest of the part due to *in-situ* homogenization occurred during high-temperature processing of EB-PBF [113,114]. In general, the cooling rate in PBF is extremely high, and therefore, the grains are almost an order of magnitude finer than those of the cast counterparts [126]. Cast Alloy 718 shows strong segregation of Nb and Mo, whereas PBF-built Alloy 718 presents reduced segregation because of the inherent high G and R [112]. The previous studies have also shown that *in-situ* or post-heat treatments of the material facilitate controlling the grain structure (size and morphology) and phases, which are influential on the fatigue performance of PBF-built Alloy 718 [127,128].

4.1. Texture and grain morphology

The texture (distribution of crystallographic orientations in a polycrystalline material) of PBF-built Alloy 718 has been frequently investigated [93,97,115,117,132-135]. The texture was found to be dependent on the directions of heat flow and the six ⟨001⟩ preferred and competing grain growth directions in Alloy 718 (with the face-centered cubic (FCC) crystallographic structure) [136]. One of the six ⟨001⟩ crystallographic orientations predominantly forms parallel to the build direction. Determined by the process parameters, i.e., energy input and scanning strategy, a variety of textures (from weak to strong) has been found in PBF of Alloy 718 [94,132]. The ⟨001⟩ texture along the build direction was found desired for enhanced fatigue performance at elevated temperatures. It can be concluded that texture is considered a critical parameter for improving location-specific properties [97].

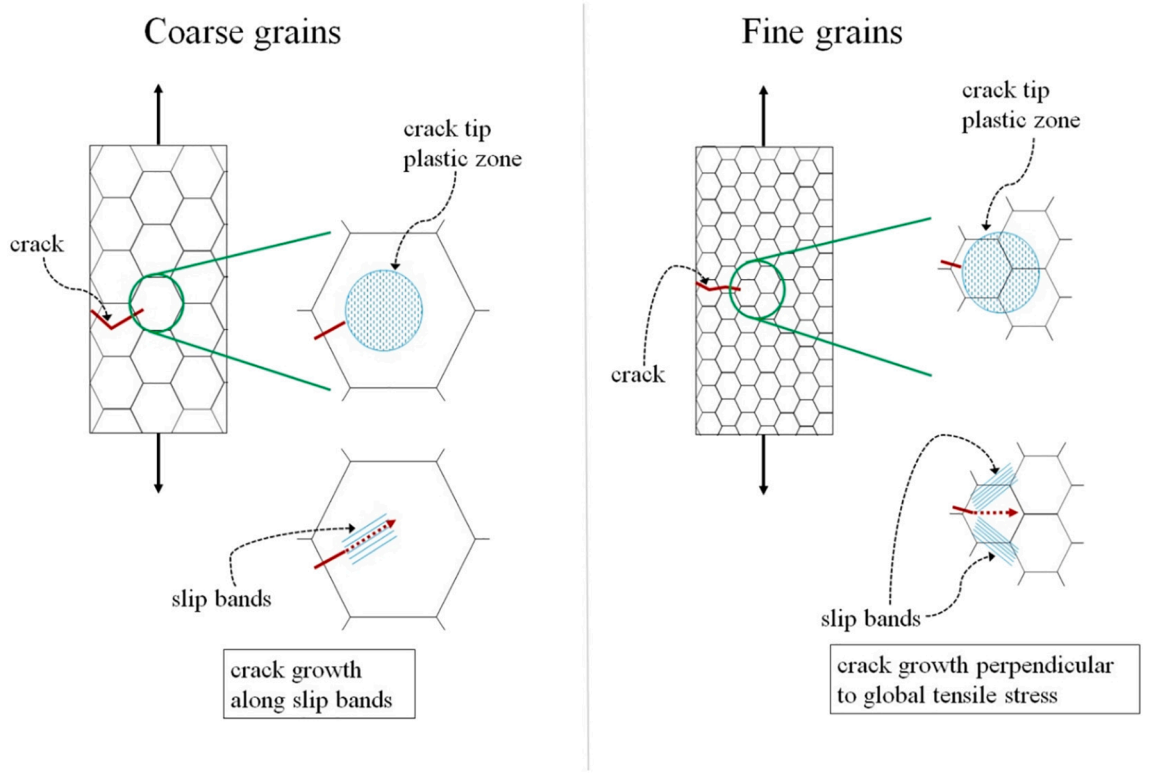

Fig. 10. Fatigue crack growth in coarse- and fine-grained parts [141]. Reprinted with permission from Elsevier.

The PBF techniques have opened a particular possibility to control anisotropic microstructures by altering thermal gradient, grain growth rate, and cooling rate during solidification. Recently, the relationship between the texture and the scanning strategies in the PBF-built parts has been investigated [137,138]. Nonetheless, limited understanding is available regarding the use of texture and grain size for functional microstructure design. Moreover, the link between preferred anisotropy, microstructure, and fatigue performance has been less investigated.

The PBF-built parts are usually identified by a textured structure with elongated grains through a few layers because of directional solidification and epitaxial growth. It was shown in LB-PBF that the elongated grains, separated by high-angle grain boundaries (HAGBs), are identified by particular sub-structures produced by regions of parallel dendrite-cells with low-angle misorientation [36,139]. Popovich et al. [97] showed that the elastic modulus is heavily influenced by texture. The regions of coarse grains with the {1 0 0} texture showed the lowest elastic modulus (~113GPa).

The impact of texture and the grain morphology on LCF of EB-PBF-built Alloy 718 were also investigated [115]. Thermally post-treated EB-PBF-built Alloy 718 acted similarly or surpassed the LCF life of reference wrought Alloy 718 at 650 ℃. The columnar grains parallel to the build direction showed a greater fatigue life than the transverse columnar and equiaxed grains. The parallel columnar part failed in a *trans*-granular mode with cracks initiating from the surface flaws. In contrast, the failure in the transverse columnar part was inter-granular, and the crack grew due to cyclic fracture of brittle oxide formed at the crack tip. The grain boundaries were shown as fast diffusion paths for oxygen towards the crack tip [140]. A small difference in fatigue life was seen in the equiaxed grains between the two orientations. Indeed, a lower inelastic strain was seen for the part under loading parallel to the build direction rather than the transverse orientation. In the parts with equiaxed grains, the effect of grain orientation on the failure was negligible, and the cracks grew in a mixed inter-granular/*trans*-granular mode through debonded/cracked carbides and voids, which formed along twin boundaries. Little sensitivity to orientations was found in the parts with the equiaxed grains.

Balachandramurthi et al. [141] showed that the fatigue crack grew through cyclic cleavage mode along with slip bands according to the single shear mechanism in coarse-grained material [109]; see Fig. 10. Moreover, the cyclic hardening behavior in the textured part was different from the non-textured one [109]. The grains in the contour region of EB-PBF-built Alloy 718 after full post-treatment (HIP + solutionizing + aging) became coarser but still with weak texture. In contrast, the grain in the hatch region after the post-treatment remained at the same size but with a stronger texture in the ⟨1 0 0⟩ orientation. Therefore, the differences in the deformation behavior and fatigue performance were linked to the dissimilarities in the grain size and the texture [141,142]. The faceting behavior was observed in the post-treated condition but not in the non-HIPed parts, in which the latter can be linked to the random orientation of the finer grains found in the non-HIPed parts. Therefore, it is concluded that the ⟨1 0 0⟩ texture in EB-PBF of Alloy 718 affected both the crack initiation and growth behavior. Sheridan et al. [142] reported that coarse-grained parts experienced shorter lives than parts with finer grains and equivalent defects.

Generally, the microstructure of PBF-built Alloy 718 differs along with the build direction because of the height-dependent thermal profile undergone by different heights of a manufactured part [119]. The bottom layers experience faster heat dissipation to the build plate due to the direct contact with the build plate compared to the top layers [125]. Therefore, the bottom layers are typically

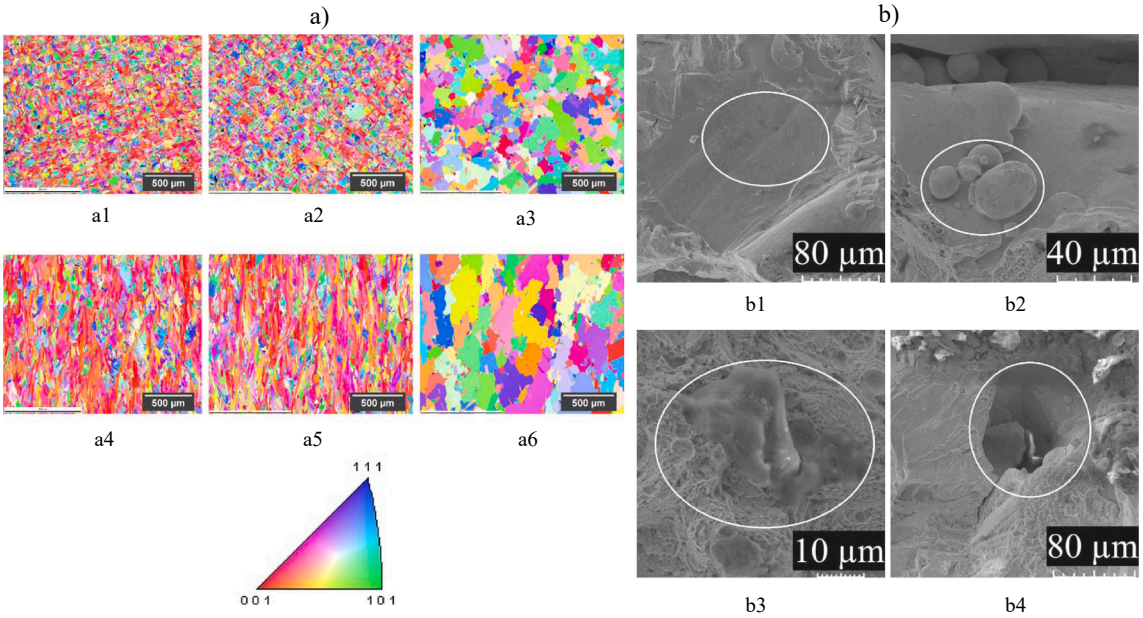

Fig. 11. Grain texture of the as-built (a1,a4), ASM-5662-treated (a2,a5) and modified heat-treated (a3,a6) Alloy 718 parts. (a1–a3) are transverse to the build direction, but (a4-a6) are parallel to the build direction, b) defects, including (b1) unadhered layers, (b2) partially sintered and unsintered particles, (b3) carbides, and (b4) pores [145]. Reprinted with permission from Elsevier.

expected to show finer microstructural features compared to those of the top layers. However, it must be considered that the bottom layers are exposed to a higher heat dwell time than the top layers, which may coarsen the microstructural features. Therefore, depending on the part size, which has a direct effect on the thermal history of the final part, nonhomogeneous microstructure is typically expected in the PBF-built parts. Material anisotropy due to the steep thermal gradient in both the LB- and EB-PBF processes can greatly influence fatigue life of Alloy 718 under strain-controlled loading, i.e., a low elastic modulus typically leads to a lower stress amplitude for a specific strain range. Larger inelastic (plastic + creep) strains typically found in parts with higher elastic modulus presented a lower fatigue life [143,144].

It was shown that the anisotropic mechanical properties of the PBF-built parts, including fatigue performance, can be mitigated by developing a new thermal post-treatment procedure. Sabelkin et al. [145] developed a modified thermal post-treatment procedure to eliminate the anisotropic mechanical behavior inherent to LB-PBF-built Alloy 718; see Fig. 11. The modified thermal post-treatment decreased the influence of the part orientation and anisotropy on the fatigue life. The surface roughness analysis showed a threshold between roughness-controlled fatigue life and orientation-controlled fatigue life. Electron backscatter diffractometry (EBSD) showed that the new thermal post-treatment led to the grain coarsening by a factor of 2.5. The part becomes highly crystallized while removing the columnar grain structure. Both thermal post-treatments enhanced the fatigue lives of the parts. The fatigue lives of the modified heat-treated 0° and 90° parts were almost similar.

Pei et al. [146] investigated the anisotropic mechanical properties of LB-PBF-built Alloy 718. The material revealed slight cyclic softening and much lower fracture strain, see Fig. 12. The LCF and HCF life of LB-PBF-built Alloy 718 was lower than wrought Alloy 718 due to the low ductility and defects in the LB-PBF-built part. Higher crack growth rates were found in LB-PBF-built Alloy 718 compared to wrought Alloy 718. The slit-shaped LoF defects in the LB-PBF-built Alloy 718 process resulted in lower fatigue life. The LoF defects were found responsible for the low ductility of LB-PBF-built Alloy 718. Moreover, the grain orientation did not affect the fatigue crack growth behavior.

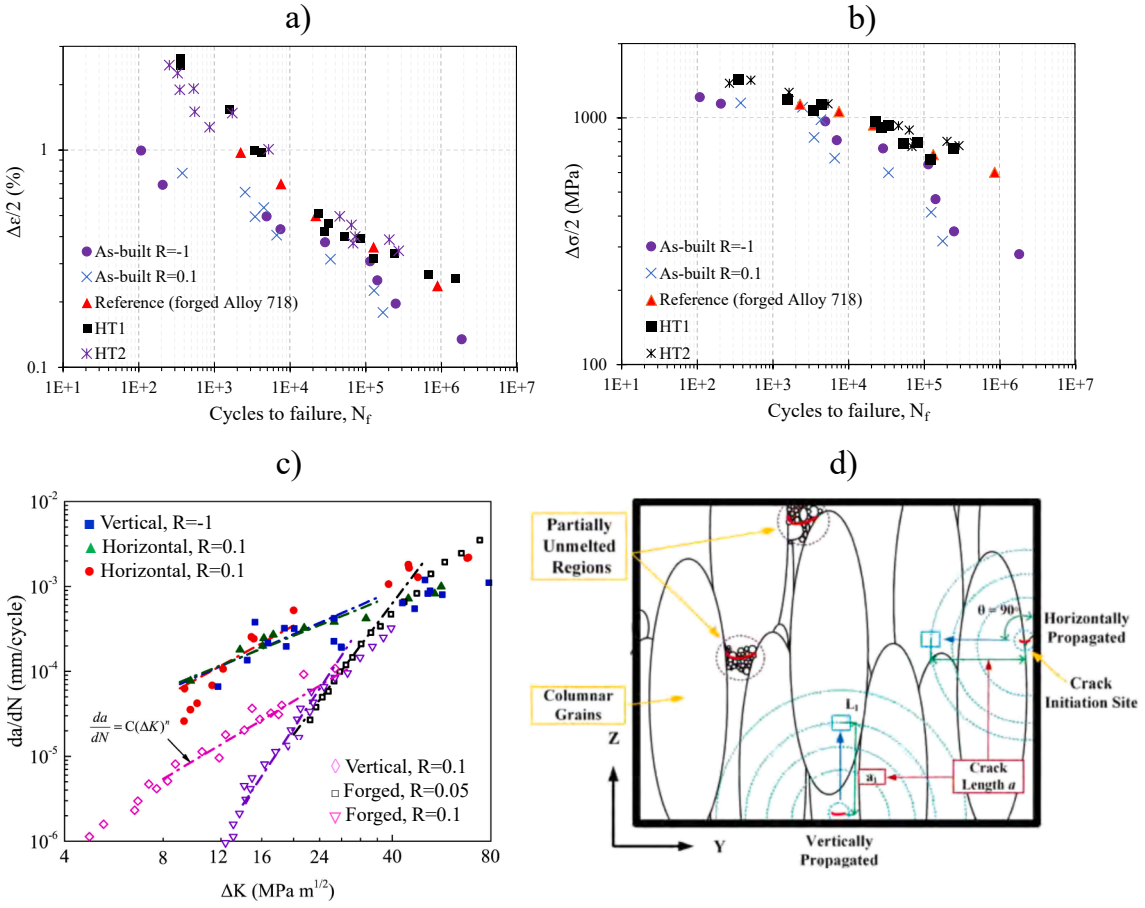

Fig. 12. (a) The strain versus fatigue life, (b) the stress versus fatigue life, c) Fatigue crack growth rates of LB-PBF-built Alloy 718 compared to the literature, and d) Schematic view of the defect distribution, crack initiation sites, and growth directions in a nonuniform material [146]. HT1: solution annealed at 1038 °C for 2 h/air cooling + double aging at 760 °C for 10 h/furnace cooling to 649 °C held for a total double-step aging time of 20 h, then air cooling. HT2: solution annealed at 940 °C for 2 h/air cooling + double aging at 718 °C for 8 h/furnace cooling to 621 °C, hold at 721 °C for a total duplex aging time of 18 h, then air cooling. Reprinted with permission from Elsevier.

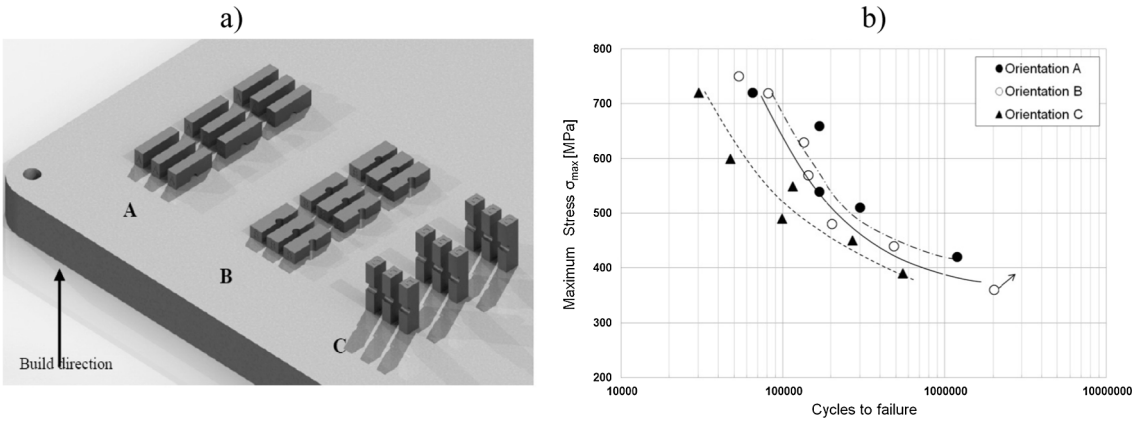

Fig. 13. A) Rendering of specimens layout in the build, and b) fatigue life of lb-pbf-built alloy 718 in different orientations with respect to the build orientation [147]. Reprinted with permission from Elsevier.

The HCF life of LB-PBF-built Alloy 718 was investigated via a novel test method to quantify the anisotropic fatigue performance [147]. The level of anisotropy of LB-PBF-built Alloy 718 was studied by testing the parts manufactured in three different directions (A, B, and C); see Fig. 13. The S—N curves showed that the direction parallel to the build direction had the minimum fatigue strength. The directionality of HCF showed that applying the cyclic loading in the build direction (C) was the most dangerous loading direction for the part, resulting in the shortest fatigue life. The other part orientations (A and B) exhibited identical fatigue life. The anisotropic fatigue performance is due to the complex microstructure inherently obtained by the layer-by-layer manufacturing process. In general, the directional fatigue response was due to i) the surface roughness that was different in the three different directions (A, B, and C), and ii) the crack initiation mechanisms.

The *in-situ* fatigue testing of LB-PBF-built Alloy 718 showed an evident link between the orientation and the growth rates of short crack [148]. The cracks grew faster in the vertically (0°) manufactured part (loading along the built direction) than the other two orientations (X:horizontal, and XZ: 45° tilted), mainly because of the small misorientation of the neighboring grains of the vertical part, following a cube texture and the lower strength along with the build direction. The part manufactured in the XZ direction showed a lower crack growth rate than that of the X specimen at room temperature; however, the difference was less at 650 °C. Witkin et al. [15] reported that the difference in the fatigue performance of the vertical and angled parts with the as-built surfaces was negligible. The horizontal parts for the intended part geometries could not be manufactured without the support structure, therefore testing the horizontal parts with the as-built surfaces was impossible. Nevertheless, the fatigue life in the horizontal and vertical parts after machining was similar, confirmed at only one stress ratio of 0.1. The LCF life of the EB-PBF-built Alloy 718 parts loaded in the parallel direction was shown better than the transverse direction. The stress ranges needed to obtain a similar strain range were lower in the

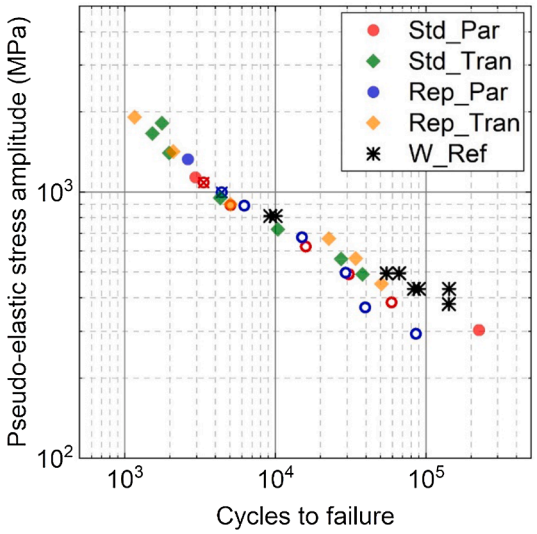

Fig. 14. Pseudo-elastic stress amplitude vs fatigue life plot. Par, Tran, Std, Rep, and W represent parallel direction, transverse direction, standard heat treatment, repair heat treatment, and wrought Alloy 718. Open symbols indicate inclusion-based crack initiation, and solid symbols indicate crack initiation due to slip at the specimen surface [149]. Reprinted with permission from Elsevier.

parallel direction than the transverse direction because the elastic modulus (E) was lower in the former direction [149]. It was postulated that the resolved shear stress on the slip planes in part loaded in the parallel direction was lower than the transverse direction. The pseudo-elastic stress based on the strain amplitude and elastic modulus ($\sigma_{pseudo\text{-}elastic} = \varepsilon_a.E$) versus fatigue life was drawn; see Fig. 14. After implementing the pseudo-elastic characteristics, the points for the parallel and transverse directions, in different post-treatment conditions (Std and Rep represent standard and repair heat treatment, respectively), converged to a linear behavior. Moreover, the scatter in data was associated with the presence of the surface inclusions.

4.2. Defects

The process-induced defects, such as the LoF defects, cracks, semi-round shape pores, shrinkage pores, and surface irregularities, have a critical role in the fatigue performance of the parts [21,102,142,150]. In particular, the PBF-built parts typically exhibit high surface roughness [151], geometrical deviations from the CAD design [152,153], residual stress [154], and anisotropic characteristics [80]. Lately, several investigations have been performed to link the process-induced defects to fatigue performance [10,155,156].

Relating the defects to the fatigue performance, several studies [157,158] have recently employed the $\sqrt{defectivearea}$ method established by Murakami [159]. In this method, the effective size of the defects in the fracture surface is firstly measured, and then relates this size to fatigue life. Bond and Zikry [160] investigated the effects of various PBF process-induced defects on the crack initiation and growth in Alloy 718. For an aggregate with 1 % area fraction of pores, a maximum in stress and the accumulated plastic shear slip were found around the pores. Cracking started in a ligament between two pores, where the interplay between the pores led to a temperature rise resulted from the plastic slip and dislocation-density activity. Cracking was dominant through the carbide/matrix interfaces. The mechanical properties of PBF-built Alloy 718 were shown to be governed by local dislocation density close to the defects [160]. Sheridan et al. [142] found that the pore size (i.e., the large pores resulted in low fatigue life) and stress level contributed to fatigue failure; therefore, a new model covering the effect of both pore size and stress level was developed to reduce the scatter in the S—N data to a single curve.

An aggregate with slit-shaped regions of un-melted powder particles located in the LoF defects had high-stress accumulations at low nominal strains. This high level of stress facilitated the crack initiation at the surroundings of the un-melted particles, which grew to the open surface. A slit-shaped LoF defect containing un-melted powder was the most dangerous defect with the highest level of stress accumulation. A deeper investigation on the crack nucleation mechanism via the LoF defects was performed in [98]; see Fig. 15. At the core of the crack initiation region, a porosity with an irregular shape was found. The appearance of the LoF defects was found irregular and random, even with an optimal processing parameter set. The LoF defects had sharp edges, leading to local stress concentration at the tip. Therefore, the LoF defects are highly undesired for the fatigue performance of the PBF parts than other defects, such as the round-shaped pores. It was found that an improper selection of processing parameters, such as insufficient applied energy input, the low quality of the powder bed, which comes from the powder spreading system functionality or stability of laser/electron beam movements, leads to local interruptions [155], which generates the LoF defects.

It was also shown that the defect (e.g., pore) size distributions could be used to estimate the fatigue life of the LB-PBF-built Alloy 718 parts, and it was found that the worst-case pore caused premature fatigue failure [161]. The process parameters were shown to be essential factors that dictated the defect content within the parts and, consequently, the fatigue life of the machined parts.

The effect of surface roughness and post-treatment, including thermal and mechanical treatments, on fatigue life of EB- and LB-PBF-built Alloy 718 was also studied using a 4-point bending test [150]. The surface roughness in the as-built condition manufactured using the recommended process theme provided by the machine suppliers was three times higher in the EB- than LB-PBF parts (S_a of 45 ± 5 μm in EB-PBF versus S_a of 15 ± 2 μm in LB-PBF). The higher layer thickness and the coarser powder particles in EB-PBF resulted in the high surface roughness. Machining reduced the S_a value of both EB- and LB-PBF parts to below 1 μm and improved fatigue life, and reduced the scatter in comparison to the as-built part. The large scatter in the as-built condition was due to the several crack initiation sites on the surface, an order of magnitude greater than those in the machined parts. The multiple crack initiation sites reduced the randomness in failures resulting in a low scatter. HIP enhanced fatigue life in both EB- and LB-PBF-built parts due to

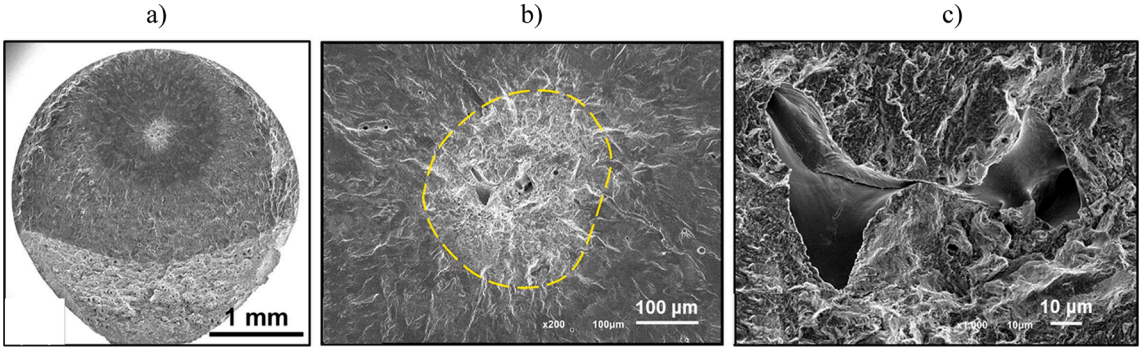

Fig. 15. Fracture surface of as-built Alloy 718 manufactured via LB-PBF, showing the LoF defects as the fatigue crack initiation sites ($\sigma_a = 480$ MPa, $N_f = 2.6231 \times 10^8$ cycles) [98]. Reprinted with permission from Elsevier.

removing a great portion of the pores. The characteristics of the crack growth region were more ductile in the heat-treated (HT) condition and more brittle (cleavage appearance) in the HIP + HT state. This difference was owing to the recrystallization, and grain growth resulted from the HIP. The LB-PBF-built part outperformed the EB-PBF-built part in HCF due to the large LoF defects found in the contour and at the contour/hatch interface regions of the EB-PBF-built parts. The LoF defects found at the surface and sub-surface regions underwent the maximum tensile stresses; therefore, the LoF defects had a more significant effect than the bulk. Moreover, inclusions inside the LoF defects prevented full closure of the defects during HIP; however, HIP was beneficial in the partial closure of the sub-surface LoF defects; hence a slight enhancement in fatigue life.

4.3. Phases

It has been shown that the γ matrix, γ“ and γ’ precipitates, δ and Laves phase do not contribute to the fatigue life. In PBF-built Alloy 718, the crack initiation was dominated by the defects and/or inclusions [52,149]. Furthermore, the smaller size of NbC and Laves phase in the PBF-built Alloy 718 compared to conventionally-built Alloy 718 [33,162] showed less influence on fatigue life.

Komarasamy et al. [163] showed that in LB-PBF-built Alloy 718, severe δ phase precipitation was present at intragranular regions, for instance, between the dendrites and inter-granular regions, together with a low amount of the Laves phase and interdendritic segregation. γ' and γ” were found in the thermal post-treated condition (954 °C for 1 h/air cool/aging at 718 °C for 8 h/furnace cool to 621 °C and held for 18 h). Thus, the hardness of the thermally-post treated part was greater than that of the as-built part (approximately 50 % higher). A high amount of δ found at the grain boundaries did not adversely affect fatigue life. Indeed, the presence of a certain amount of globular δ at the grain boundaries was found important for improving the resistance to intergranular crack propagation because of two reasons [164]: i) Globular δ phase distribution at the grain boundaries can block intergranular crack propagation, and ii) The ductile region near the grain boundaries due to the existence of a denuded zone of γ″ and γ′ can relax the stress concentration at the grain boundaries, and retard the grain boundary crack initiation and propagation.

The relationship between the microstructure of LB-PBF-built Alloy 718, exposed to two different thermal post-treatments (stress relief and full heat treatment), and fatigue life, was investigated [165]. Stress relief was performed at 1065 °C/1.5 h followed by an argon gas cooling. The full heat treatment was conducted at 1177 °C/1h/ followed by a cooling rate of 38 °C/h, then 982 °C/1h/gas fan cooling, and finally 718 °C/8 h/furnace cooled/621 °C/18 h/gas fan cooling. The stress-relieving treatment led to grain coarsening, an equiaxed grain microstructure, the elimination of the dendrite cell structure, and the formation of γ’ and γ“. The microstructure resulted from each of the above two heat treatments had its own fatigue-strengthening mechanisms in preventing the plastic flow. The stress-relieved part showed a homogenous distribution of strain because of the refined grains and cell boundaries [166]. The fully heat-treated part had the uniform distribution of γ’, γ’’, and annealing twins. The strengthening by precipitates hardening was found more efficient than grain and cell boundaries.

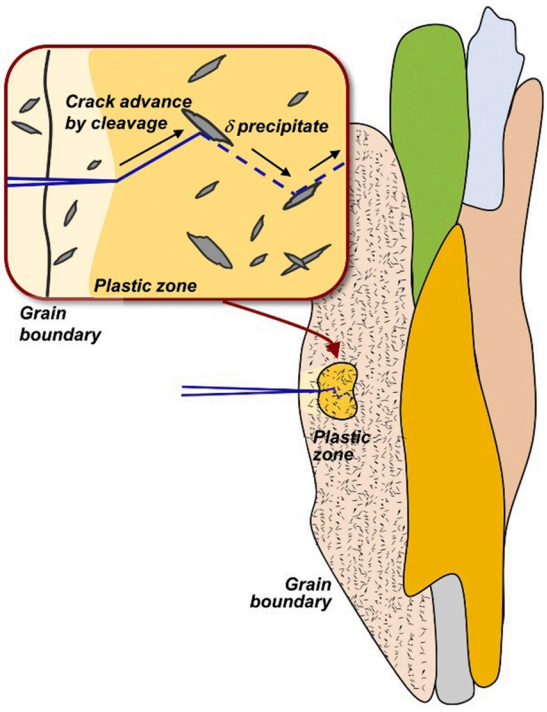

Fig. 16. The schematic view of the interaction between δ precipitates and a growing crack following a particular cleavage plane, demonstrating how precipitates and/or Laves phases frequently obstruct the advancement of the crack [169].

LB-PBF-built Alloy 718 studied in both the as-built and direct aged conditions had a substantial level of the Laves phase; however, the fatigue life was not affected by this phase [167]. The δ phase found in in [149] resulted in a softening behavior in the cyclic stress–strain curve as δ reduced the size and volume fraction of the γ‘‘ and γ’ precipitates. however, the fatigue life did not change even with a high amount of δ. The γ’’ and γ’ precipitates showed a contradictory effect on cyclic behavior, i.e., the phase may result in cyclic hardening or softening. The absence of γ‘‘ and γ’ resulted in an initial cycle-dependent hardening before the beginning of the softening behavior [167]. The initial softening was because of the interaction between the uniformly distributed deformation-induced dislocations. Later, the rearrangement of the dislocations led to softening behavior. In contrast, the presence of γ’’ and γ’ resulted in cyclic softening [149,167], because the dislocations shear the precipitates during loading [168].

According to Fig. 16, grain orientation has a negligible effect on the crack propagation of LB-PBF Alloy 718 because δ precipitates, rather than grain boundaries, obstruct the advance of growing crack at the crack tip [169]. Indeed, several studies have demonstrated that the relationship between the direction of construction and the direction of crack growth has no effect on the crack propagation resistance of the AM Alloy 718 parts [146]. Previously, fractographic examination of Alloy 718 specimens fabricated using the LB-PBF process revealed that the number of defects on the fracture surface was significantly greater than the number of defects on the microstructure, implying that fatigue cracks tended to grow in the direction of the relatively weak area containing defects [65].

4.4. Residual stress

Residual stress is the stress that exists after the elimination of applied stress in the material [56]. While the influence of microscopic stress resulted from precipitates or atomic dislocations are localized, macroscopic stress can have a significant influence on the PBF-built parts; the macroscopic stress can be induced thermally in the PBF-built parts via differential expansion/contraction during and after solidification. Residual stress is inherent in PBF-built Alloy 718 due to the rapid cooling rate of the process, which can adversely affect the mechanical properties and fatigue performance. The residual stress can motivate the grain structure alterations, e.g., grain coarsening, when the part is exposed to subsequent heat treatment. Residual stress was higher in LB-PBF than EB-PBF because of the lower processing temperature in the former technique. Considering the complex thermal history in PBF, understanding residual stress formation at different length scales and reducing the amount of residual stress are highly critical [170].

One of the critical process parameters affecting the residual stress is the scanning strategy [171,172]. In LB-PBF, the island scanning strategy is commonly used to decrease the residual stress. The island scanning strategy is a checkerboard pattern of alternating unidirectional fills, efficiently reducing the temperature gradients in the scan plane by better distributing the heat. This strategy can be more important when the material being built presents a high level of anisotropy in mechanical properties. The residual stress affects the part’s structural integrity [151], particularly when the external loads are cyclic (i.e., fatigue). In HCF, the crack can initiate from the micron-scale, known as Types II and III residual stress. Moreover, it is also reported that the presence of the residual stress at the macro-scale (Type I) also reduces the HCF life. The residual stress acts as mean stress superimposed to the cyclic load. The mean stresses typically have a significant impact on the HCF life. Overall, residual stress is an important aspect of fatigue life that is deserved considerable attention [174-176].

4.5. Surface condition and notch effect

The fatigue life of the PBF-built parts with as-built surfaces was found to be substantially inferior (around 40 % lower) compared to that of the polished/machined surfaces [15,177-179]. The high surface roughness induces local stress concentrations resulting in the crack initiation at lower applied stresses and shorter fatigue cycles. The surface roughness depends on several parameters, such as powder characteristics, process parameters, and build orientations. Post-surface engineering techniques have been extensively investigated because most parts’ functionalities need a smooth and finished surface. However, the cost of extra processing, such as machining or finishing, can be undesirable for the industry. Complexity in geometrical design is one of the critical motives of the PBF technology; however, the surfaces of the PBF-built part might not even be accessible for most post-surface processing.

The standard fatigue testing of specimens, either round or flat, uniform, or continuous radius, is an accepted method of evaluating the fatigue performance. However, it is worth noting that, according to military handbooks for aerospace vehicle structures, particularly MIL-HDBK-5, rotating beam and bending fatigue testing are not recommended. According to Gorelik [180], life-limiting features, such as the locations of high-stress concentration, might affect fatigue in a way that is not clear based only on the uniform or continuous radius specimens. Therefore, the notched specimens have been utilized to understand the effect of such stress concentrations.

Dealing with the fatigue performance of the notched PBF-built specimens, two main approaches are followed, i.e., testing (i) machined specimens (with or without the notch) or (ii) as-built specimens (with or without the designed notch). The geometry of the notch might interact with the internal features and defects of the test specimen [181]. In the as-built parts, smaller notches/defects induced by the PBF process can be found on the surface of the notches. Such defects serve as notches (with smaller dimensions) within the primary notch geometry [182], where cracks can initiate. The microstructural characteristics rely on the notch geometry [183]. The quasi-static loading of the as-built notches was investigated [183], verifying notch strengthening behavior and that the negative effect of defects is decreased when the notch acuity rises [184].

The surface roughness has a significant influence on fatigue life, particularly when the part thickness is reduced. The effect is even worse when the combined impact of miniaturization (build thickness) and surface conditions on the mechanical properties, particularly the fatigue performance of the PBF-built parts, is concerned. Little information is available concerning the combined influence of surface roughness and part thickness on the fatigue life of the PBF-built parts. This knowledge is highly critical as intricate designs

usually have internal passages that cannot be readily machined after manufacturing. For such complex parts, the interior surface irregularities are likely a dominating factor in fatigue life. Fatemi et al. [185] showed that the surface roughness of the as-built part is similarly the motive in multi-axial fatigue failures. Pegues et al. [151] reported that the cracks initiate at the rough down-skin surfaces, and the more irregular surfaces had a lower fatigue life.

The influence of the surface roughness and the build thickness on the fatigue life of LB-PBF-built Alloy 718 at 650 °C were thoroughly investigated [106]. The high-temperature fatigue strength was increased by approximately 50 %, and the R_a value was decreased from around 14 to 0.1 μm after machining and polishing. The rough surface of the LB-PBF parts was due to two primary steps that each layer experience [186]; i.e., (i) the stripe scanning strategy using a high laser energy input coupled with a low scanning speed, and (ii) the contouring step using a low laser energy input coupled with a high scanning speed. A high level of total energy is needed for the thicker parts. The greater total energy during the contouring step might encourage sintering and entangle more powder particles from the surrounding, leading to a rougher surface. Unexpectedly, un-machined thinner parts showed a longer fatigue life than the machined thicker parts, a behavior linked to several factors, e.g., stress distribution, surface roughness and thickness-dependent microstructure. It seems that the defect shape had a more severe impact on fatigue life than the defect depth (d) when $d \leq 200$ μm because of the significant stress concentrations.

Based on the quantitative X-ray computed tomography (X-ray CT) analysis and the alteration in the stress concentration factor (K_t), the LB-PBF-induced surface defects were divided into three categories and also given into simple shapes [106]. The three types of defects were defects with i) $1 < K_t < 3$ (oblate hemi-ellipsoid shape), ii) $K_t = 3$ (hemispheroid shape), and iii) $K_t > 3$ (prolate hemi-ellipsoid shape). Based on the finite element (FE) analysis conducted to estimate the fatigue life of the parts, the shape of the defect had a more substantial effect on fatigue life than the depth of defect (d), when d is below 200 μm due to the great stress concentrations. The impact of size, shape, distribution, spacing, and orientation of the surface defects on fatigue life is worth further investigation. For instance, in cast materials, the smaller spacing of the surface defects yielded more interaction among the defects and thus resulted in higher stress concentration and lower fatigue life [187].

The locations of crack initiation in LB-PBF-built Alloy 718 under static and cyclic loading were investigated [188]; see Fig. 17. The notch strengthening was found in quasi-static loading, whereas the notch weakening was found in HCF. It was already shown by Lei et al. [189] that the strengthening was resulted from forcing a transition from shear-mode to normal-mode failure due to the geometrical limits of the notch geometry. A notch strengthening to weakening transition was found at approximately 10^3 cycles

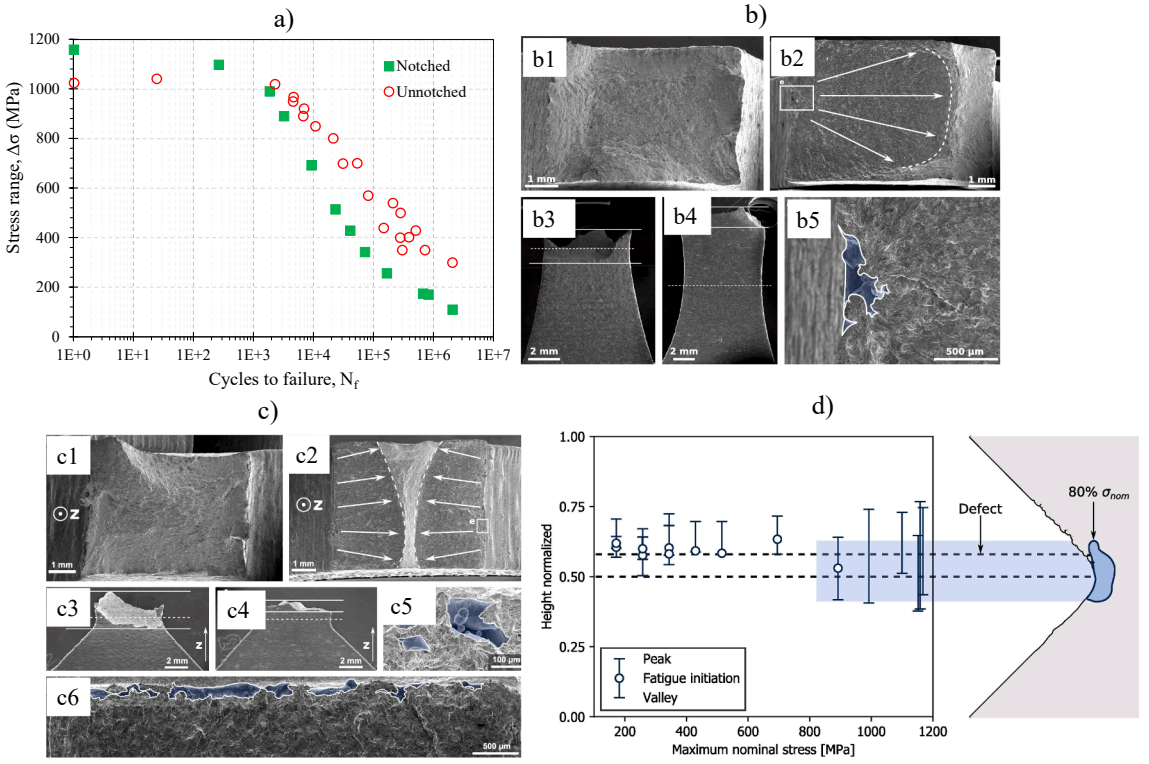

Fig. 17. A) S—N diagram of the cyclic and quasi-static tests, b) Fracture surface of the unnotched specimens. (b1) Fracture surface after static loading (b2) Fracture surface after cyclic loading (b3) Front view after static loading (b4) Front view after cyclic loading (b5) Defect from the fracture surface in cyclic loading, Fracture surface of the notched specimens. (c1) Fracture surface after static loading (c2) Fracture surface after cyclic loading (c3) Front view after static loading (c4) Front view after cyclic loading (c5) Detail of defect from crack initiation (c6) Distribution of defects along the edge of a notched specimen. d) Failure locations of the notched specimens compared to (asymmetric) stress field from FEA [188]. Reprinted with permission from Elsevier.

corresponding to a stress level of about 1000 MPa. In HCF, the crack started from the down-skin surface (with R_z of 259 μm) of the notched specimens and not from the primary notch roots designed in the specimen, see Fig. 17d. The defects found on the down-skin surface were named crust defects [190] instead of the LoF defect. The crack initiated from a surface defect in the unnotched specimen and then grew within the part until fracture. In this specimen, the crack did not initiate in the minimum cross-section. In the notched specimen, the crack grew from both notches (designed on two sides of the specimen) towards the center of the specimen. For the unnotched specimen, a wide scatter was observed in the locations of failure from both the up-skin and the down-skin surfaces. The locations of failure were not localized in one region in the unnotched specimen, unlike the notched specimen.

Kotzem et al. [191] investigated the influence of miniaturization and surface roughness on fatigue life in EB-PBF of Alloy 718, see Fig. 18. The microstructure in the small-scale and large-scale parts was identical. However, the small-scale parts had a higher level of defects with higher geometrical deviations, leading to sharp changes in cross-section and greater stress concentration zones at the surface. The as-built part had a low surface quality with a high level of defects; therefore, the part showed lower mechanical strength, i.e., 60 % drop in ultimate tensile strength and 75 % drop in fatigue strength. In the polished parts, all the parts failed from the surface and sub-surface defects. Furthermore, no sign of the LoF defects was found in the fracture surface, but only fine round-shaped pores were present. In contrast to the fracture surface of the polished parts, the fracture surface of the as-built parts showed a high level of the un-melted powders and sub-surface LoF defects that served similar to the notch defects during cyclic loading, resulting in stress concentrations and accordingly lower fatigue life.

The influence of the contour parameters on the surface roughness and fatigue life of LB-PBF-built Alloy 718 was evaluated [192]. Two surface parameters of arithmetic mean height (S_a) and maximum pit height (S_v) were measured via two non-destructive testing methods of structured light (SL) surface scanning and X-ray CT, see Fig. 19. S_a was reduced with a rise in laser power, but an obvious relationship between S_a and scan speed was not found. S_v was decreased with an increase in laser power; however, S_v was increased with a rise in scan speed. The process parameters significantly influenced the melt pool size. An enhanced laser power resulted in a larger melt pool and finer surface notches. Further increasing the laser power led to keyholing that created sub-surface pores.

On the other hand, an enhanced scan speed resulted in finer melt pools and larger surface notches. The surface analysis by X-ray CT supported similar behavior; however, X-ray CT is able to measure larger maximum notches than those of the SL technique because the powder and large surface asperities did not completely cover the surface. S_v had an inverse correlation to fatigue life; see Fig. 19. By increasing S_v, fatigue life was reduced. This correlation was confirmed in both measurement techniques, with the X-ray CT technique giving a better fit. S_a did not have any relationship to fatigue life. The fracture surfaces illustrate that when the surface roughness is high, and the notch values are maximum, the contour is not adequately fused to the underlying layer, leading to large notches. When the higher laser power is applied, the layers are well fused, and the crack initiates at a surface notch at the interface between the melt pools of the contour. The high laser power at low scan speed resulted in the lowest S_v and also led the crack initiation sites to be from inclusions instead of a surface notch. It was confirmed that if a proper melting strategy is applied, the crack initiation site will be affected by other factors, including inclusions and sub-surface defects.

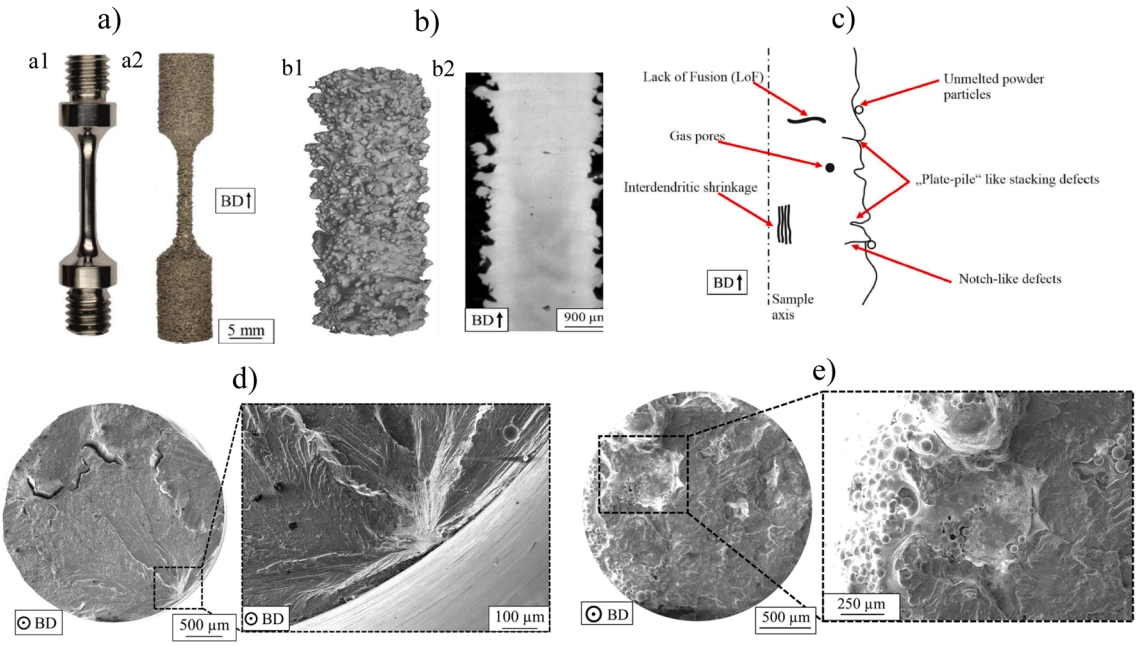

Fig. 18. The specimen geometry for mechanical testing in a1) polished, and a2) as-built condition, b1) Reconstructed 3D volume and corresponding b2) μ-CT cross-section, c) Schematic view of defects in the small-scale EB-PBF-built Alloy 718 part, d) Fracture surface of the polished specimen tested on stress amplitude σ_a = 520 MPa (N_f = 82725 cycles), and e) Fracture surface of the as-built specimen tested at a stress amplitude of σ_a = 120 MPa (N_f = 76722 cycles) [191]. Reprinted with permission from Elsevier.

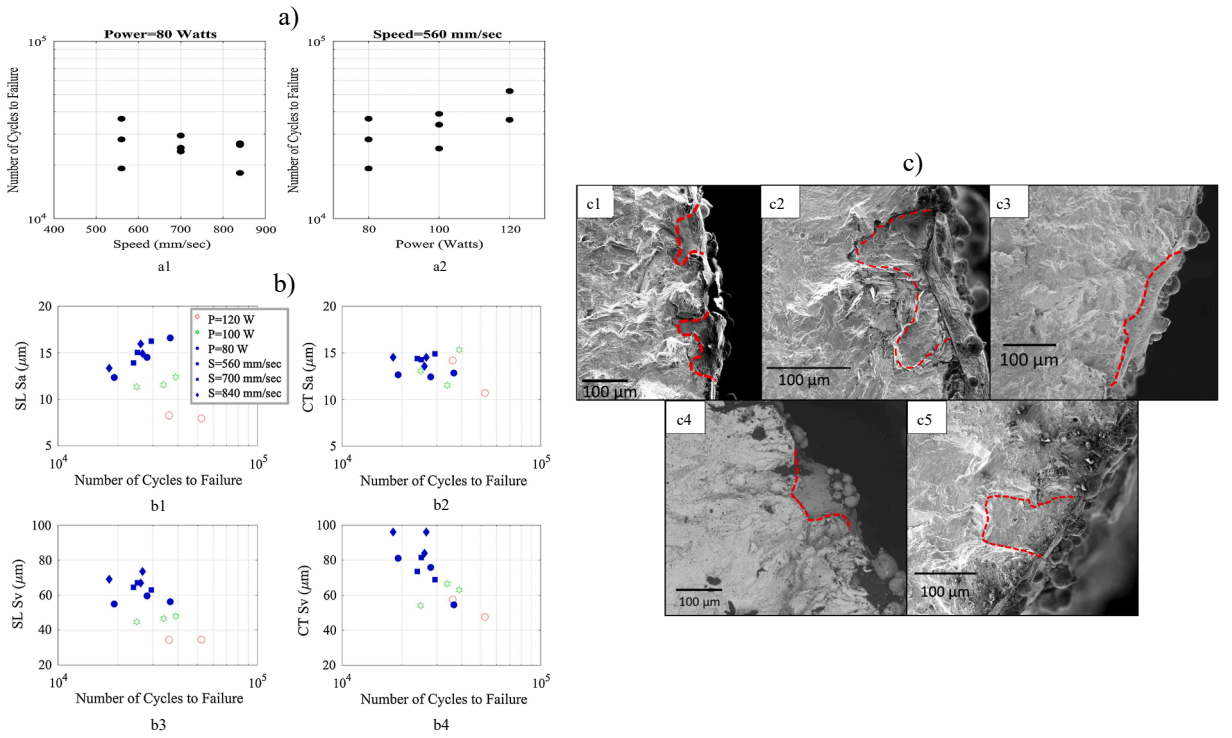

Fig. 19. A) Relationship between fatigue life and the process parameters in the contour region, b) relationship between fatigue life and surface roughness parameters obtained via the sl and x-ct methods (b1) sl s_a, (b2) CT S_a, (b3) SL $S_{v,}$ and (b4) CT S_v, and c) Fracture surfaces resulted from each contour parameter set. (c1) P = 80 W, S = 820 mm/*sec* (c2) P = 80 W, S = 700 mm/*sec* (c3) P = 80 W, S = 560 mm/*sec* (c4) P = 100 W, S = 560 mm/*sec*, (c5) P = 120 W, S = 560 mm/*sec* [192]. Reprinted with permission from Elsevier.

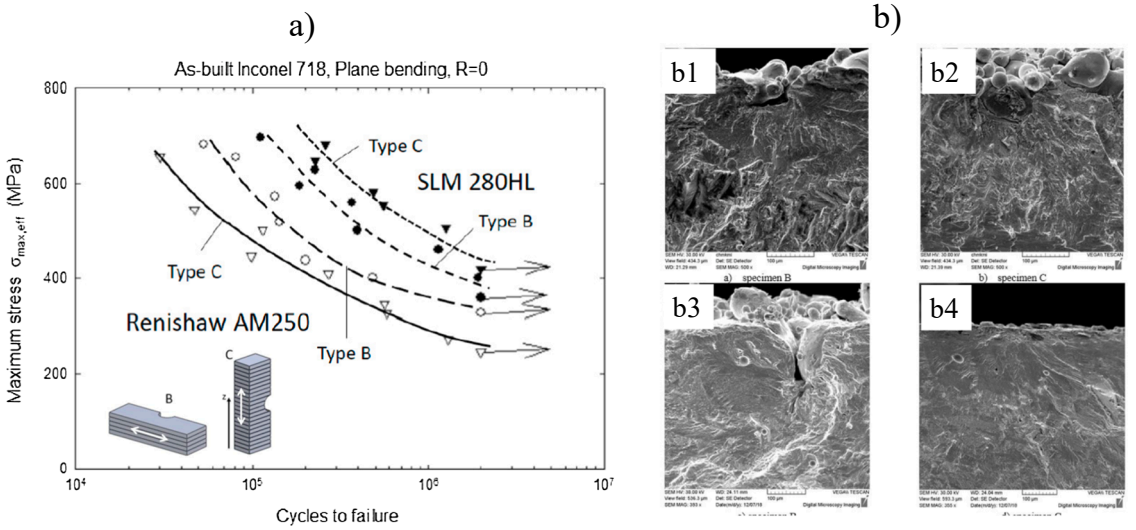

Fig. 20. A) Orientations of the miniature specimen with respect to the build direction. The white arrows show the applied stress direction. The fatigue life of Alloy 718 built via two LB-PBF machines, b) crack initiation sites in the parts built via b1), b2) Renishaw AM250, and b3), b4) SLM 280 HL [193]. Reprinted with permission from Elsevier.

The fatigue life of the LB-PBF-built Alloy 718 parts built in two different LB-PBF machines and different loading directions was studied [193]; see Fig. 20. The process parameters and scanning strategy significantly influenced the fatigue performance of Alloy 718. The LB-PBF part built via SLM Solutions 280HL with a 50-μm layer thickness provided a greater fatigue life than the part built via Renishaw AM250 with a 30-μm layer thickness; see Fig. 20c. Thicker layers increased the build rate in the flat surfaces, but thinner

layers increased the resolution for the desired geometry in the curved surfaces. The effective fatigue strength (σ_{max} at 2×10^6 cycles at R = 0) of as-built LB-PBF-built Alloy 718 ranged from 260 to 455 MPa depending on the manufacturing machine and stress orientation. The critical factors in crack initiation were the stress level and surface defects. Regardless of the machine type, several fatigue crack initiation sites were found in each part.

The influence of geometrical notches on fatigue performance of LB-PBF-built Alloy 718 was investigated using the small parts [194]. The parts in three different orientations (A, B, and C) were manufactured and investigated; see Fig. 21. The orientation in C was identified by layers that were perpendicular to both the build direction and loading direction. The layers in B, A+ (with upward notch), and A− (with downward notch) were similarly parallel to the loading direction. The main difference between the above parts was the surface quality in the flat area, i.e., the flat surface in A − was the top and last layers obtained during manufacturing, whereas in A+, the flat surface was achieved by wire cutting. The notch quality also varied in different parts, i.e., the semicircular notch geometry of B was achieved by laser contouring, layer after layer; however, the notch quality in A + and A − were influenced by the process parameters. The notch quality in A − was also different from that in A+, because the former notch was manufactured based on the down-skin orientation, and the latter notch was identified by the up-skin orientation. The fatigue results showed that (i) the surfaces of the LB-PBF-built parts influenced the fatigue performance when a macroscopic notch exists, and (ii) the vertical U-parts have longer fatigue life than the horizontal parts significantly. The results showed that the as-built geometries had process-induced features that contributed to the higher surface irregularities and lower fatigue life.

Solberg et al. [182] investigated fatigue performance of the notched Alloy 718 parts built via LB-PBF; see Fig. 22. The fatigue notch factor increased with decreasing the notch radius. A notch sensitivity value between 0 and 1in the v-notched parts and above 1 in the semi-circular parts was achieved. The obtained values were linked to the higher roughness in the down-skin surfaces. By reducing the notch radius, the level of scattering in both the location of failure and fatigue life decreased. The notch geometry and defects from the overhanging region acted as stress risers and were the reasons for the little scattering. When there was a low-stress concentration in the notch geometry, the defects were the reason for failure, and a wide scatter was found; however, when there was a large stress concentration, the cracking initiated at the notch root, and the scatter was negligible. The surface defects were found as the crack initiation sites in all the parts. The locations of failure were localized defects and large LoF defects (basically found along the edge of the notch) in the unnotched and notched parts, respectively. A clear relationship between the area of the defect and positioning in confidence bands was reported for the unnotched parts, while the link was unclear for the notched parts. The relationship between the locations of cracking and the notch acuity is shown in Fig. 22c. The figure indicates whether the notch geometry or the defect is the motive for failure and where exactly failure is in a notch geometry.

Witkin et al. [178] showed that HCF of the machined LB-PBF parts had similar behavior to the wrought Alloy 718 plate parts, whereas the as-built parts showed a lower fatigue life than both machined LB-PBF and wrought Alloy 718 parts. According to linear elastic fracture mechanics (LEFM) theory for short cracks initiating from the notch roots, it was shown that the intrinsic surface features of the LB-PBF-built parts can be the crack initiation sites. The notch geometries showed that stress intensity in the presence of surface defects is critical in quantifying the cycles before the crack initiates and grows. Machining LB-PBF-built Alloy 718 to final test size with K_t of approximately 3 resulted in fatigue life that was similar to the wrought part. These parts also deviated from the notch design requirement concerning K_t, probably due to residual stress generated during LB-PBF. It was confirmed that the stress intensity attributed to a notch was mistakenly calculated at short cracks using the formula given by Tada et al. [195]; therefore, a new factor was developed to consider the stress concentration of the notch at a short crack. The new analysis confirmed that the difference in the fatigue life of the as-built and machined surfaces was because of the short cracks found at the notch roots. For the as-built surfaces, a model combining stress intensity and stress concentration verified that a short crack at the root of a notch provides a greater effect on stress intensity compared to the notch itself. This mechanism shows that the low fatigue life in LB-PBF-built parts is associated with a high-stress intensity connected to crack-like surface features, resulting in early crack initiation.

The relationships between surface roughness, build orientation (0, 60, and 90), process parameters, and the HCF life in LB-PBF of Alloy 718 were investigated [69]. Two competing mechanisms influenced the fatigue performance. The first mechanism addressed the link between the build orientation and the surface roughness. Improper build orientation design resulted in increased surface roughness, leading to a rise in the frequency of the surface crack initiation sites and hence, a drop in fatigue life. The second mechanism

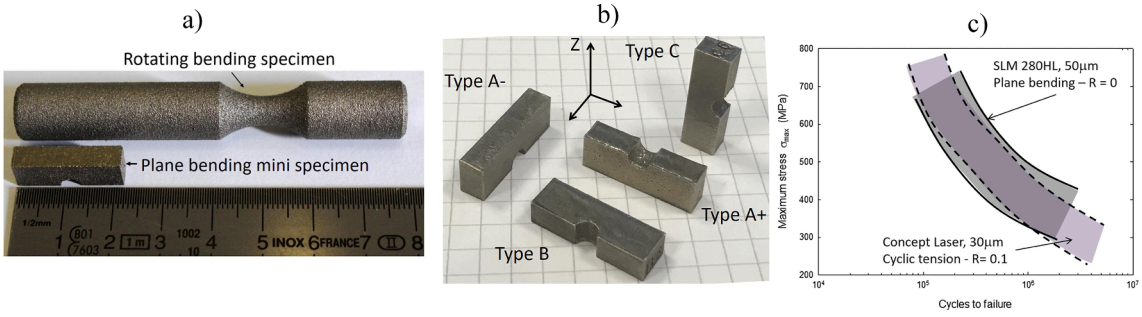

Fig. 21. The standard and modified fatigue specimens (axial lengths of 80 mm for the standard cylindrical specimen versus 22 mm for the miniature specimen), b) the specimen types based on orientations with respect to the build direction (Z), and c) Directional fatigue performance (obtained via the SLM 280HL machine) compared to the data obtained via the Concept Laser machine [194]. Reprinted with permission from Elsevier.

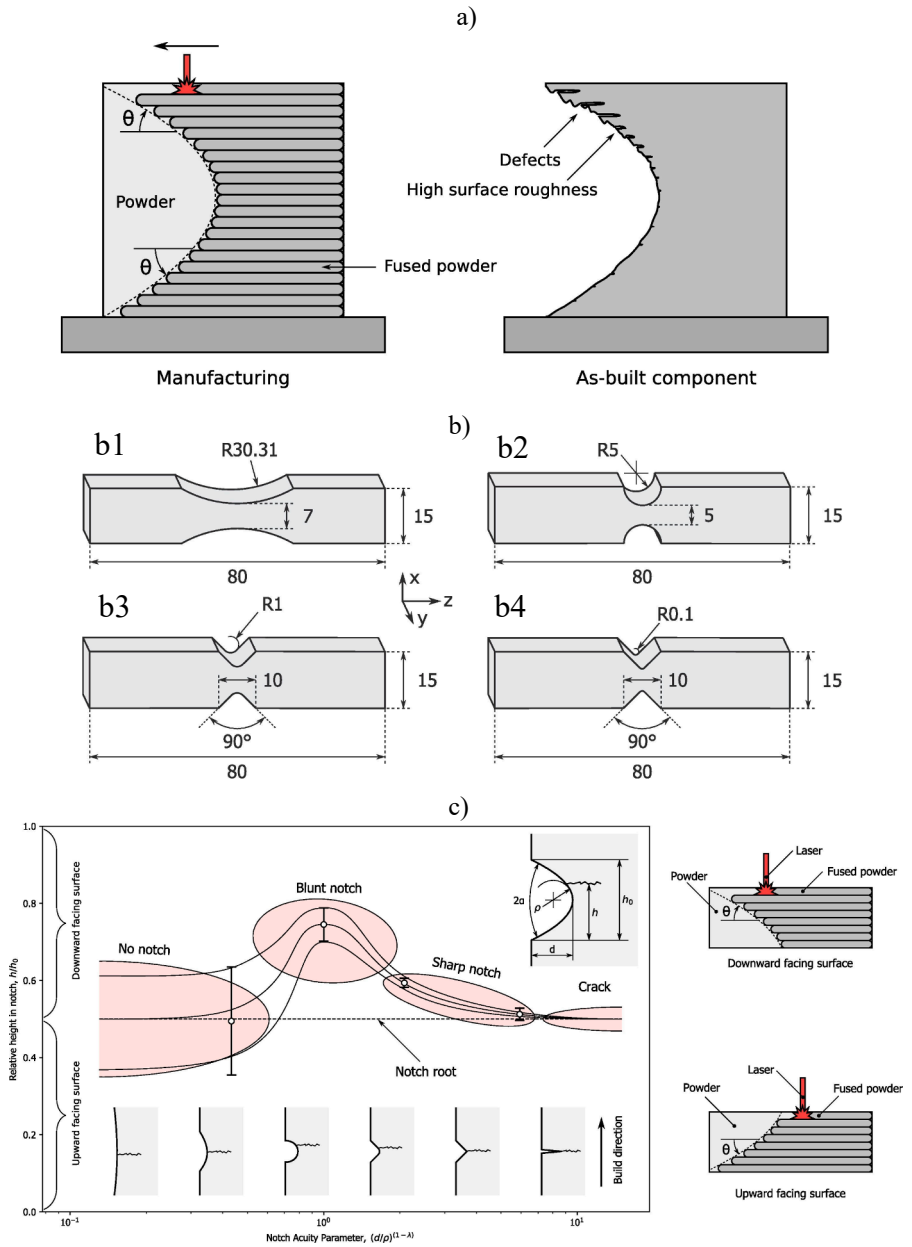

Fig. 22. a) Schematic view of the designed and as-built parts. The as-built part shows defects and low surface quality in down-skin surfaces, b) Part geometries: (b1) Unnotched; (b2) semi-circular notch; (b3) V-shaped notch with notch radius of 1 mm; (b4) V-shaped notch with notch radius of 0.1 mm. The notch depth of the parts: 4 mm, 5 mm, 4.59 mm, and 4.96 mm for (b1), (b2), (b3), and (b4), respectively, and c) Diagram linking location of failure in a notched region to the notch acuity [182]. Reprinted with permission from Elsevier.

addressed the effect of an inappropriate volumetric laser energy input, leading to an increase in the level of the sub-surface defects, and eventually, a drop in fatigue life. The worst total fatigue life was found in the horizontal parts (0° build orientation), whereas the 60° build orientation parts presented the highest life. The fracture surfaces in Fig. 23 showed a greater number of the surface crack initiation sites on the horizontal parts than on the vertical (90° build orientation) and 60° build orientation parts. Therefore, fatigue life was primarily governed by surface roughness, a factor that affected the number of surface crack initiation sites and was primarily linked to the build orientation. The drop in fatigue life was because of the early crack initiation and rapid crack growth because of the enhanced level of surface defects. The fatigue life for a given build orientation showed a bell-shaped curve, see Fig. 23c. An optimal laser energy input, governing by the layer thickness, was found in the fatigue life curve. The optimal laser energy input values were 60–70 and 40–45 J/mm^3 for the 30-μm and 60-μm layer thicknesses, respectively. At very low and high energy input values, there was an enhanced number of surface and sub-surface defects. The LoF defects and the keyhole pores were predominant in very low and high

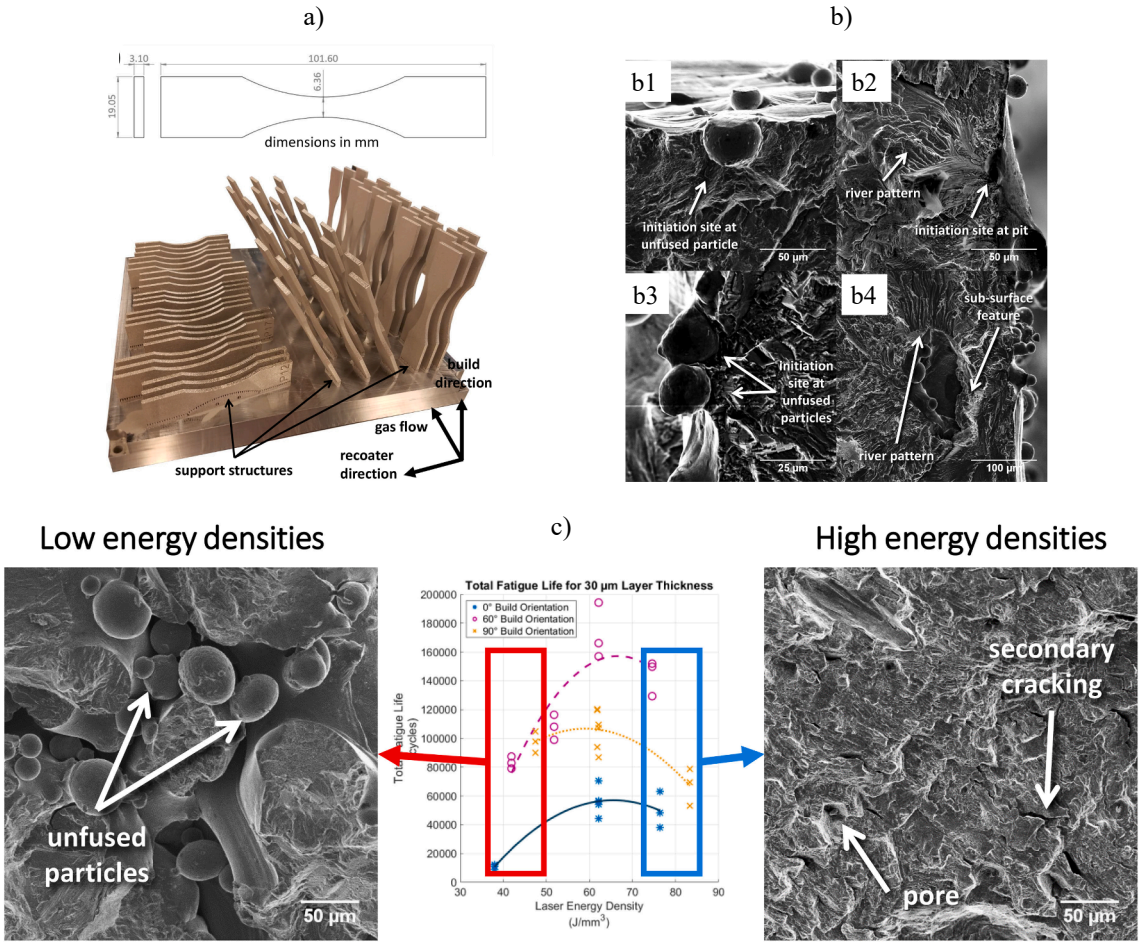

Fig. 23. A1) The specimen dimensions according to astm e466-15, and a2) the as-built alloy 718 specimens before the build plate removal, b) sem images (se mode) of the surface cracks in b1) 60, b2) 90, and b3)0°oriented parts, b4) a representative sub-surface crack initiation site, and c) the relationship between HCF life and the sub-surface defects [69]. Reprinted with permission from Elsevier.

laser energy input values, respectively. To increase the fatigue life of LB-PBF-built Alloy 718, it was recommended to reduce the sub-surface defects by screening the process parameters in the contour region, such as the laser power, scan speed, hatch spacing, and layer thickness, as well as reduce the surface roughness by selecting a proper build orientation or machining.

4.6. Thermal and mechanical post-processing

While there are limited heat-treatment standards for AM materials, PBF-built Alloy 718 is commonly subjected to a set of thermal post-treatments, including stress relief (SR), hot isostatic pressing (HIP), solution treatment (ST), and aging, such as direct aging (DA), single or double-step aging [13,15,69,84,196-199]. The selection of the individual post-treatment is based on the initial microstructure, the level of defects, and residual stress in the as-built condition; therefore, not every step of the above thermal post-treatment is necessarily required for a specific PBF-built part. In general, HT removes residual stress and resets the microstructure. The HIP is intended to close the internal pores, such as the shrinkage and round shape pores; however, the surface-connected defects, inclusion-filled LoF defects, and argon-containing pores are not entirely eliminated by HIP [173]. The mechanical post-treatment can be used to alter the surface condition. For instance, machining removes the outer layer of the as-built part, which is generally found to be highly rough with several irregularities [15].

HIP has been generally used to reduce the defects formed during the PBF processes; however, the non-affected pores after HIP and re-growth of pores during subsequent heat treatment have also been frequently reported [200-203]. After the thermal post-treatment, the mechanical properties of PBF-built Alloy 718 might be comparable to or even better compared to those of the conventionally-manufactured wrought and cast parts. Nonetheless, when it comes to time-dependent applications, such as creep and dwell-time fatigue at high temperatures, the heat-treatment standards already developed for the wrought and cast parts are not optimized for the PBF-built parts. For instance, recovering the intricate dislocation sub-structures in the microstructure of LB-PBF-built Alloy 718 by heat treatment is highly essential for their creep and dwell-time fatigue performance. The solutionizing temperature and time (<1100 ℃

and 1–2 h) used for the cast parts eliminate the deleterious Laves phase and uniform the elemental segregation; however, this homogenization condition is inadequate to remove the residual dislocation sub-structure and full recrystallization. Aydinöz et al. [204] also reported that HIP (1150 °C/100 MPa/4h/furnace cool) eliminates the dislocation sub-structure and facilitates the formation of the grain boundary δ phase that significantly decreases the LCF life of Alloy 718 built via LB-PBF [13]. Kanagarajah et al. [205] found a similar dislocation sub-structure governing the yield strength and the ultimate tensile strength in LB-PBF; however, the drop in fatigue life of the heat-treated parts was linked to the process-induced defects, such as pores [14]. Balachandramurthi et al. [177] showed that δ in the as-built condition was only found at some grain boundaries of EB-PBF-built Alloy 718. After the solutionizing and aging (STA) treatments (1066 °C for 1 h/argon quench/aging at 760 °C for 10 h/furnace cool to 649 °C and held for 8 h), δ became smaller than those found in the as-built condition. After the HIP + STA treatment (HIP at 1200 °C/120 MPa/4h/rapid quench), δ was completely dissolved. HIP + STA led to grain growth in the contour region, whereas no grain size change was reported after STA. Partial healing of the LoF defects occurred after HIP + STA was verified by the fracture surface analysis; therefore, fatigue life was enhanced, see Fig. 24. The highest fatigue strength was obtained when the contour regions were machined entirely. The faceted appearance of the fracture surfaces was a result of both grain size and texture [177]. The full elimination of the contour region guaranteed the absence of the LoF defects leading to significant enhancement in the fatigue strength. The closure of the shrinkage pores due to the full thermal post-treatment (HIP + solutionizing + aging) positively affected the crack growth behavior by reducing the local crack growth rate. Because of removing the LoF defects and shrinkage pores, the post-treated (HIP + solutionizing + aging) parts led to fatigue life with two orders of magnitude greater than that of the as-built parts.

The effect of various surface treatments on the surface roughness and fatigue properties of LB-PBF Alloy 718 were investigated [206]. These treatments included sand-blasting, drag-finishing, turning, grinding, and grinding + drag-finishing. Each of the surface treatment methods completely eliminated the irregularities on the as-built surface, but each reintroduces its own distinct surface topography. As a result, their fatigue lives were significantly different, particularly at lower strain amplitudes. All surface treatments improved fatigue performance, with sandblasting and drag-finishing causing the least improvement and grinding + drag-finishing causing the greatest improvement. Only the cracks in grinding + drag-finished specimens originated from crystallographic facets, whereas those in other conditions originated on the surface. While turning and grinding significantly improved the surface condition, as indicated by significantly decreased surface roughness metrics, the machining marks retained sufficiently severe stress concentrations to initiate cracks from the surface.

5. Fatigue life evaluation and fracture mechanisms

5.1. Low- and high-cycle fatigue (LCF and HCF)

The LCF and HCF failures are two of the primary failure modes characterized in the industry [109]. Therefore, it is essential to understand the LCF and HCF performance and principle mechanisms of the failure for Alloy 718 built via PBF processes. The HCF regime is more sensitive to defects than LCF, as the fatigue life is dominated by crack initiation in HCF rather than crack growth in LCF. It is also reported that failure of turbine blades typically takes place in the very high cycle fatigue (VHCF) (above 10^7 cycles) condition [207]. A limited number of studies have been focused on VHCF of the AM alloys [82,82,98]. Due to the high sensitivity of VHCF to defects, even small defects may act as crack initiation sites [208], which necessitates post-processing treatments, such as HIP. Ono et al.

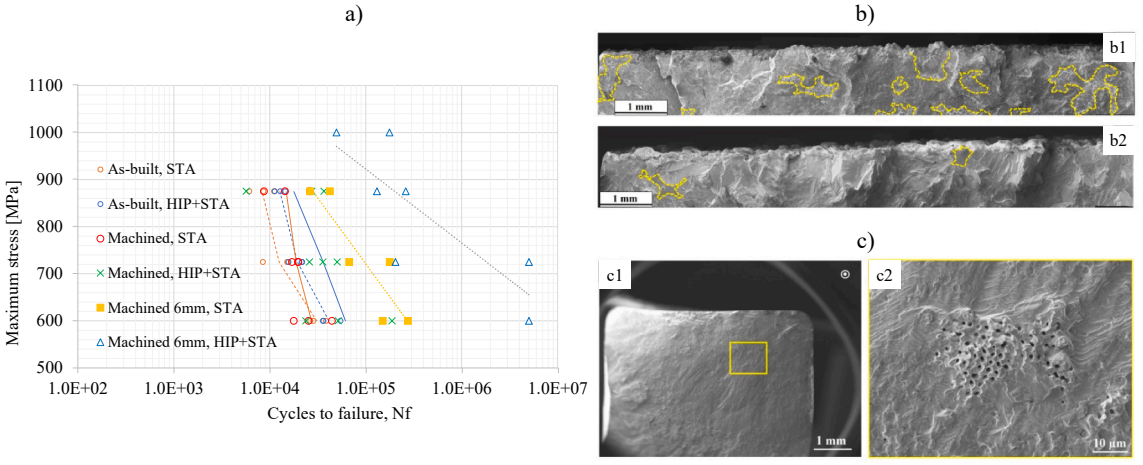

Fig. 24. A) S—N curves of EB-PBF-built Alloy 718 in various post-treated conditions, b) SEM images (SE mode) of fracture surfaces presenting the crack initiation sites in the as-built surface condition of the (b1) STA part; (b2) HIP + STA part. The yellow dotted lines show the LoF region, and c) SEM images (SE mode) of the fracture surface of a part in the STA condition; (c1) overall view, (c2) the shrinkage pores in the crack growth region [177]. Reprinted with permission from Elsevier. (For interpretation of the references to color in this figure legend, the reader is referred to the web version of this article.)

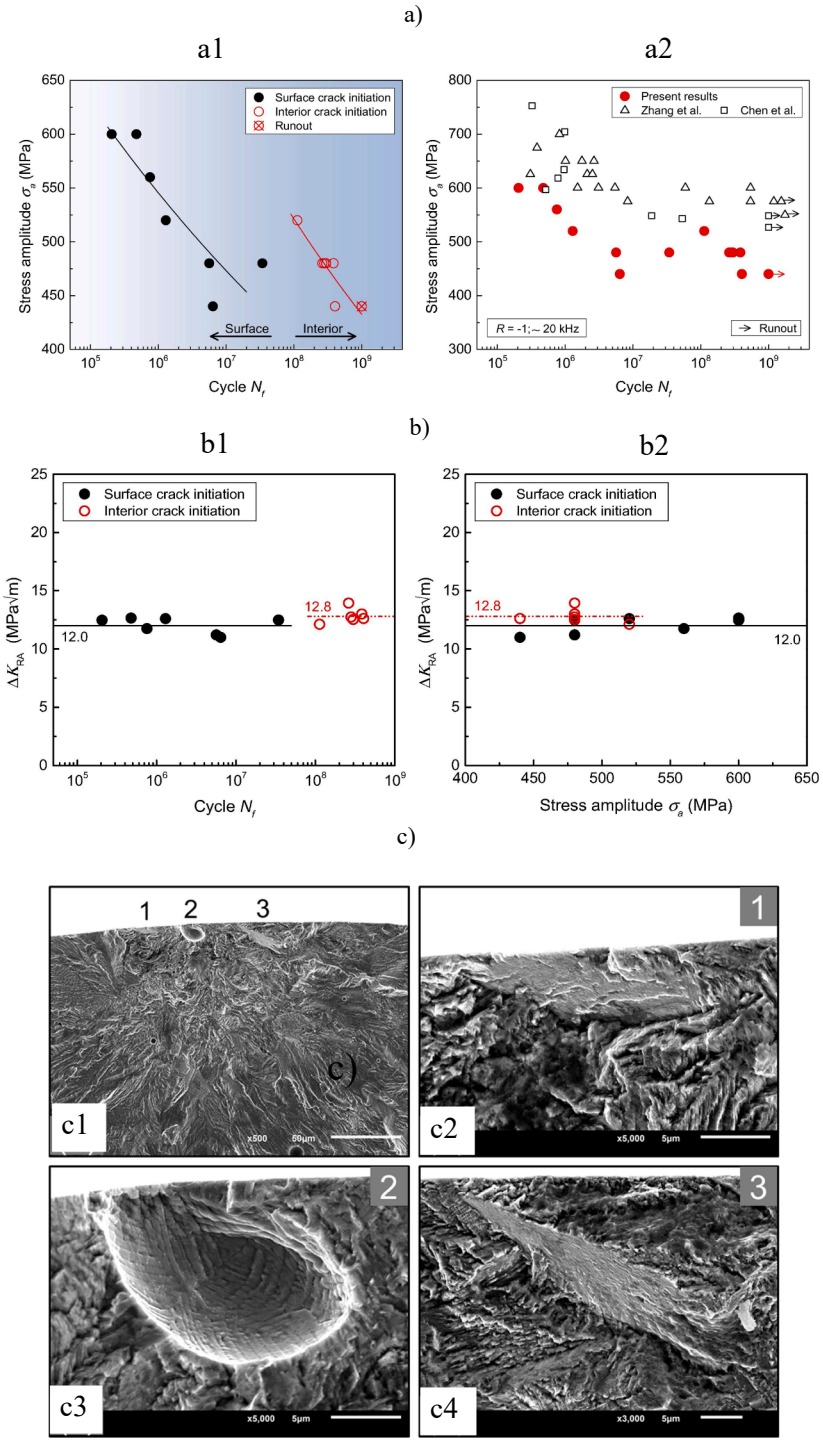

Fig. 25. A1) S—N data and fitted curves in as-built Alloy 718 at R = -1, a2) fatigue life of as-built and conventionally-built Alloy 718. b) Variations in the stress intensity factor range at the tip of the rough area (ΔK_{RA}) versus fatigue life (b1) and stress amplitude (b2), and c) representative SEM images (SE mode) showing the coexistence of the pore and facet in the same crack initiation site ($\sigma_a = 480$ MPa, $N_f = 5.6573 \times 10^6$ cycles), (c1) a high-magnification SEM image of the regions of crack initiation and growth, (c2), (c3) and (c4) the morphology of crack initiation sites marked with 1, 2, and 3 in (c1) [98]. The results were compared with Zhang et al. [213] and Chen et al. [214]. Reprinted with permission from Elsevier.

[209] reported that the HCF cracks mainly initiated from the coarse Nb-rich carbides and faceted structures were mainly due to the carbides at the cryogenic temperatures. Nonetheless, no non-metallic inclusion, such as the Nb-rich MC-type carbide, Laves, or δ, was found at the crack initiation site at room temperature, implying that these phases did not contribute to cracking [210]. Sadeghi et al. [52] found that the clustered inclusions were the main crack initiation sites in LCF of EB-PBF-built Alloy 718. Sivaprasad et al. [211] determined that cracks can detour around the Laves phase, but the influence of the Laves phase on the crack growth was not studied thoroughly.

Yang et al. [98] studied the HCF and VHCF behavior of LB-PBF-built Alloy 718 with a primary focus on three different crack initiation sites, i.e., i) the round-shaped pores, ii) the LoF defects, and iii) the crystallographic facet. Separate S—N curves were obtained due to the competition between the surface and interior crack initiation sites; see Fig. 25. The cracks can simultaneously

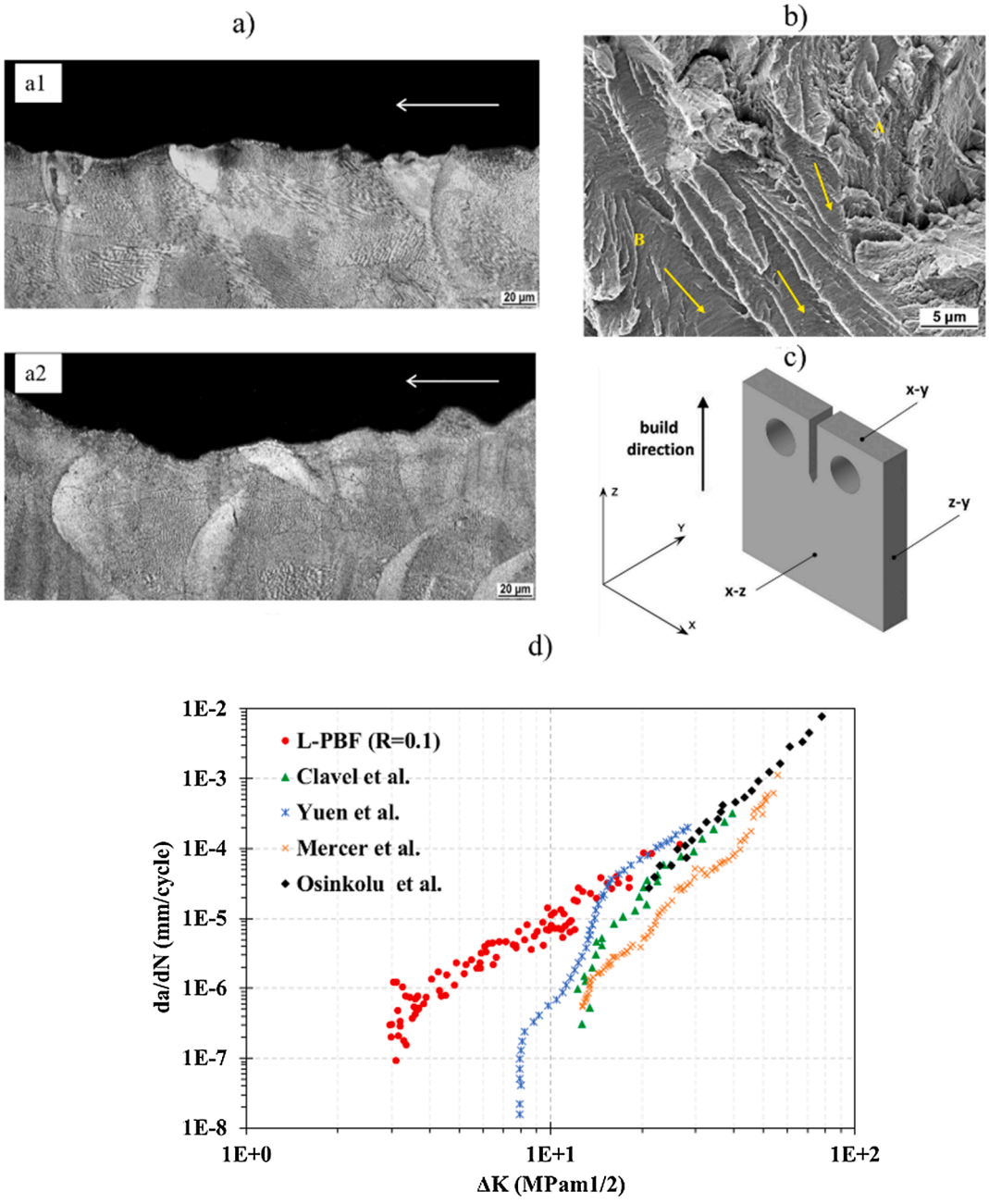

Fig. 26. A) Cross section of the fracture surface of (a1) $\delta K = 3.2$ MPam$^{1/2}$, da/dN ~ 10^{-7} mm/cycle, (a2) $\Delta K = 10.0$ MPam$^{1/2}$, da/dN ~ 10^{-5} mm/cycle, b) fracture surface corresponding to the average crack growth rate of 8×10^{-7} mm/cycle, c) Orientation of compact tension (CT) specimen, and d) Comparison of fatigue crack growth data for conventionally- and LB-PBF-built Alloy 718 [215]. The results were compared with Clavel et al. [224], Yuen et al. [225], Mercer et al. [221], and Osinkolu et al. [218]. Reprinted with permission from Elsevier.

emanate from the round-shaped pores, LoF defects, and columnar grains in the parts. As shown in Fig. 25a, it is concluded that it is challenging to eliminate the defects in the PBF-built parts [212] and, therefore, the fatigue life of the PBF-built parts is usually lower than that of the conventionally-built Alloy 718 parts [155].

The fracture surface of LB-PBF-built Alloy 718 was evaluated, and the stress intensity factor range at the tip of the rough area (ΔK_{RA}) was calculated for the surface and sub-surface crack initiation sites [98]; see Fig. 25b. ΔK for the sub-surface crack under low stress resulted in an underestimation of fatigue performance. Therefore, this approach led to a conservative evaluation of the crack initiation sites. ΔK_{RA} was between 11.0 and 12.8 $MPa\sqrt{m}$ for the surface crack initiation and between 12.1 and 14.0 $MPa\sqrt{m}$ for the interior crack initiation. The ΔK_{RA} values corresponding to the crack growth threshold of the long cracks ($\Delta K_{th,lc}$) were lower than that of conventionally-built Alloy 718. Therefore, the growth rate of the internal cracks was substantially lower to that of the surface cracks. Therefore, although the cracks initiated from the interior of the part, fatigue life was longer. The maximal cracks resulted from the defects, such as the pores, LoF defects, or facet in the crack initiation region, governed the failure, despite finding multiple cracks in the crack initiation region; see Fig. 25c. It was found that the fatigue life controlled by each feature, including the pore, facet, and LoF defect is insignificant when the site of crack initiation is already known, and the cracks have the same sizes. The HCF and VHCF life were found reliant on the size and location of the cracks with the maximum size. The maximum size of crack for the interior crack initiation were larger than those of the surface; however, fatigue life for the interior crack initiation was significantly longer than that for the surface crack initiation [98]. It verifies that the location of the crack on fatigue life is more critical compared to the size of the crack. Therefore, an efficient strategy to increase the fatigue life of the PBF-built parts is to move the crack location from surface to interior. This strategy increases fatigue life by at least two orders of magnitude. Another method is to push the inclusions towards the part's surface (i.e., the contour region) by choosing an appropriate process setting such as energy input and scanning strategy during manufacturing, followed by machining the surface [52].

5.2. Fatigue crack growth (FCG)

The crack growth in Alloy 718 built via LB-PBF has been widely studied [10,198,215,216]. Konecna et al. [215] investigated. The threshold value of the stress intensity factor (ΔK_{th}) was 3.0 $MPa\sqrt{m}$. In loading with ΔK above 20 $MPa\sqrt{m}$, the crack growth of LB-PBF-built and wrought Alloy 718 was similar; see Fig. 26. LB-PBF-built Alloy 718 had less resistance to the crack growth in the near-threshold region compared to conventionally-built Alloy 718. The low ΔK_{th} value of LB-PBF-built Alloy 718 was associated with (i) low boron content, (ii) specific grain structure, and (iii) residual stress. Reducing the level of boron from 100 to 12 ppm substantially increased the crack growth rate and decreased ΔK_{th} [217].

The investigated Alloy 718 built via LB-PBF exhibited very fine grains (about 10 μm). It is known that ΔK_{th} decreases with a decrease in the grain size [218,219]. The cross-section of the fracture surface shown in Fig. 26a verifies that the crack grew in the threshold region without intervention with the microstructural characteristics, such as the grain boundaries. There was no interference between the crack paths and the melt pool tracks (or the building layers). The crack growth mode was *trans*-granular; see Fig. 26b. The fracture surface was identical to that found in conventionally-built Alloy 718 [220,221].

The LB-PBF-built parts showed high residual stress. The crack growth rate in part before and after the stress relief post-treatment was different, which was associated with the modified residual stress states. According to Fig. 26c, by assuming that the crack growth direction is parallel to the build direction and the region surrounding the designed notch was melted last, the tensile residual stress can be anticipated affecting the notch root and favoring the closure-free crack growth. The residual stress is highly crucial in the analysis of the FCG behavior of the LB-PBF-built parts [222]. The crack growth mechanism was attributed to the planar cyclic slip in the area ahead of the primary crack tip. The cyclic slip was localized on the parallel slip planes, and the cyclic loading resulted in damage of selected slip bands and the formation of cracks. The primary crack grew by rupture of regions where the slip activity is weak due to improper orientation. This mechanism is already developed for conventionally-built Alloy 718 [223]. The crack growth mechanism in the near-threshold and the Paris regions was found almost identical. The main difference was in the size of the cyclically-loaded volume, which increased by enhancing ΔK and the cyclic plastic zone size. The effects of larger cyclic slip activity and larger plastic zone at higher ΔK were reflected in wider cracks found in the fracture surface. The crack path was *trans*-granular for growth rates ranging from the threshold region to the end of the Paris region. The striations were formed at the crack growth rates of 1×10^{-4} mm/cycle; see Fig. 26d. This is an indication of the change in the crack growth mechanism into ductile at high ΔK. The plastic blunting mechanism at the high crack growth rates can be used similar to conventionally-built Alloy 718 [223]. The da/dN versus ΔK curves of both the LB-PBF-built and wrought Alloy 718 parts are identical in the high crack growth rate region.

5.3. Dwell time effect

The turbine disks are typically exposed to dwell-time fatigue during service. The dwell time means that there is a holding period at maximum or minimum stress besides the cyclic loading. By increasing the dwell time, the crack growth rate in conventionally-built Alloy 718 has been significantly increased and becomes time dependent [226-228]. The effect of tensile dwell on crack growth in conventionally-built Alloy 718 at high temperatures has been extensively studied [228,229], verifying that the oxidation-induced failure during the dwell period leads to an enhanced crack growth rate. Dynamic embrittlement (DE) [230] and stress-assisted grain boundary oxidation (SAGBO) [231] were the two primary mechanisms in the inter-granular cracking mode that resulted from the dwell-time fatigue. DE explains that oxygen diffusion leads to the de-cohesion of the grain boundaries ahead of the crack tip with no oxide formation. According to SAGBO, the oxides formed ahead of the crack tip break away. While both mechanisms are under

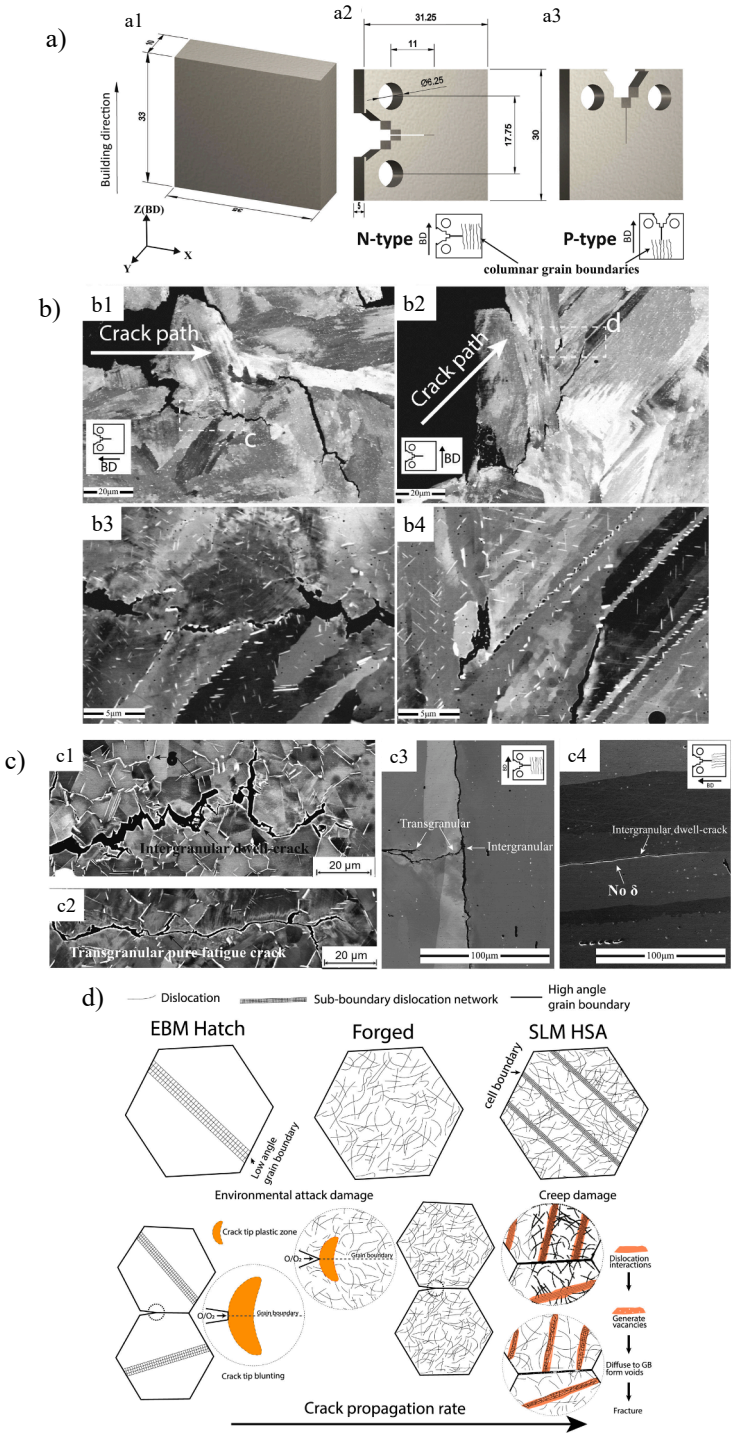

Fig. 27. Schematic drawing of the (a1) as-built specimen, (a2) *N*-type compact tension (CT) specimen with the notch in a direction normal to both the building direction and columnar grain boundaries, (a3) P-type CT specimen with the notch in a direction parallel to both the building direction and columnar grain boundaries [104]. b) Crack paths of solutionized + aged Alloy 718 built via LB-PBF (b1) P-type and (b2) *N*-type specimens illustrating the notch orientation effects. (b3) and (b4) Magnified areas marked in (b1) and (b2), respectively [235], and c) schematic view of damage mechanisms and crack growth rates with respect to the dislocation structures in the grains of EB-PBF, forged and LB-PBF. Reprinted with permission from Elsevier.

debate, the grain boundaries are concerned in the two mechanisms. It is clear that the grain boundaries are weak and most probably cracked when the crack growth becomes more time-dependent. It has been reported that the characteristics of the grain boundaries substantially influence the failure mechanism [232]. Kane et al. [233,234] showed that low angle grain boundaries (LAGBs) and coincident site lattice (CSL) Σ3 grain boundaries performed better against inter-granular oxidation and cracking compared to high angle grain boundaries (HAGBs) and other CSL grain boundaries.

The dwell-time fatigue crack growth of LB-PBF-built Alloy 718 at 550 ℃ under different thermal post-treatment conditions was studied [235]; see Fig. 27. The primary damage mechanism during the dwell-time crack growth of LB-PBF-built Alloy 718 at 550 ℃ was creep, whereas the environmentally-assisted grain boundary damage was reported for forged Alloy 718. Therefore, LB-PBF-built Alloy 718 showed lower dwell-time fatigue resistance than forged Alloy 718. The δ phase located at the grain boundaries inhibited the grain boundary sliding and reduced the crack growth rate. The transformation of the δ phase to Nb_2O_5, leading to an accelerated crack growth rate, a sign of an environmentally-assisted grain boundary damage, was not observed. Indeed, the grain boundary precipitates inhibited the grain boundary sliding through the formation of micro-voids and linkage of the wedge cracks, which are the sign of creep failure. In the *N*-type parts (loading parallel to the columnar grains), the columnar grain boundaries mostly deviated at a small angle, leading to an inferior effective stress intensity for the kinked crack path. The failure mechanism was similar in the N- and P-type parts (loading perpendicular to the columnar grains). The secondary cracks were found to be discontinuous and perpendicular to the loading direction without branching from the primary crack, verifying that the secondary cracks were not subjected to the oxygen atmosphere. The secondary cracks were associated with high-angle grain boundaries (>15°) with plastic deformation. These characteristics showed that the cracking mechanism was governed by creep rather than an environmentally-assisted grain boundary damage in LB-PBF-built Alloy 718. If DE or SAGBO was possible, the diffusion of oxygen through some grains was mandatory. Such long-range oxygen transportation via lattice diffusion was unlikely due to the rather low test temperature (550 ℃). Moreover, some random grain boundaries were passed within this long-range transportation but were not cracked, which again confronted with DE and SAGBO. Therefore, environmentally-assisted grain boundary oxidation was not the main damage mechanism. Creep of LB-PBF-built Alloy 718 was significantly inferior to cast and wrought Alloy 718, i.e., the steady creep regime was missing, and the onset of tertiary creep happened very early. The early onset of tertiary creep [236] explains the fast crack growth rate in LB-PBF-built Alloy 718.

The anisotropic dwell-time fatigue performance was likely because of the difference between the angles of the columnar grain boundaries and loading direction in the P- and *N*-type parts (i.e., perpendicular, and parallel loadings to the columnar grains, respectively). In *N*-type, the effective stress intensity factor was inferior resulted from the significant deviation of the dwell-time fatigue crack from the pre-crack plane. This deviation was reported as the primary cause for the higher dwell cracking resistance of the *N*-type compared to P-type.

The dwell-time fatigue life of EB-PBF-built Alloy 718 at 550 ℃ was also investigated with a focus on the anisotropic cracking resistance [104]. The *N*-type specimen showed improved dwell-time fatigue performance compared to the P-type specimen. In both N- and P-type, when the crack reached the high angle grain boundaries (HAGBs), the crack growth direction changed to inter-granular, whereas the direction was unchanged when the crack reached the low angle grain boundaries (LAGBs). Thermal post-treatment did not change the dwell-time fatigue crack growth rate in P-type. EB-PBF-built Alloy 718 showed greater resistance to dwell-time fatigue cracking (both *N*-type and P-type) than forged Alloy 718 [21]. The grain size, low angle grain boundaries, and the grain boundary δ phase were the primary reasons for the better fatigue performance of EB-PBF-built Alloy 718. A schematic view of environmentally-assisted and creep damage mechanisms considering the dislocation structure in EB-PBF-built, LB-PBF-built and forged Alloy 718 after a full thermal post-treatment (1080℃ for 1 h/980℃ for 1 h/720℃ for 8 h/620℃ for 8 h), are given in Fig. 27c [130]. The figure illustrates that the crack growth rate during the dwell-time fatigue was enhanced by increasing dislocation density within the grains. The role of the dislocation density in LB-PBF and EB-PBF was different and considered as a deciding factor in determining the susceptibility of the material to creep or environmental damage. The dislocation structure in EB-PBF accommodates the misorientation between the two adjacent sub-grains, and such a dislocation-induced boundary is similar to an equilibrium low angle grain boundary. In LB-PBF, the dislocation density surpasses the requirement for accommodating the misorientation between the two adjacent sub-grains, which is linked more to the deformation process and is better termed as a cell boundary. The LB-PBF dislocation network was more closely packed than that of EB-PBF.

6. Opportunities, challenges, and future directions

The PBF techniques have undergone tremendous advances in recent years; however, a few common technical challenges are to be addressed before the technology can have a substantial effect. A major issue in PBF is obtaining the desired surface and bulk quality, leading to enhanced fatigue performance [186]. Certain features are identified on the PBF-built parts surface, e.g., overhangs from down-skin surfaces, balling defects, staircase defects, satellites, surface-related micro-cracks or sharp end valleys, and stacked partially-melted powder particles [170]. Screening the process parameters in the contour region (e.g., modifying the number of contours and using an appropriate melting strategy), using a high-quality powder, or refraining from the use of support structures (if possible) can boost the surface quality [237,238]. The nonuniformities on the surface of the PBF-built parts require the implementation of appropriate post-surface treatment, including chemical milling, electrochemical polishing, shot peening, extrude honing, chemically assisted vibro-finishing, ultrasonic cavitation, laser remelting, grinding, sandblasting that can be practically implemented on the parts to improve the surface quality and consequently fatigue life [16,61,170,239]. The mechanical post-treatment, such as shot peening, can introduce compressive residual stress, which can be impressive in increasing the resistance to fatigue crack initiation and growth as well as in removing the pores at the sub-surface regions [61]. Although the tailored microstructure with less anisotropy showed enhanced fatigue life in PBF-built Alloy 718 [240]; the fatigue life of the PBF-built parts is still governed by the internal and

surface defects rather than the microstructural features [150,241,242].

If the PBF-built part is initially homogenous and defect-free, the microstructural decay under fatigue loading will be longer. In the nonhomogeneous material, pre-existing flaws, non-metallic inclusions, or surface defects act as local stress raisers, in which cracks can readily initiate. In Alloy 718, the co-existence of unwanted non-metallic inclusions, such as oxides (e.g., Al-rich oxide) and nitrides (e.g., TiN) in the recycled powders, were commonly documented [53]. Such inclusions were found to be extremely deleterious to the mechanical properties, particularly fatigue, because of their brittle nature and high-strain localization characteristics [243]. The removal of these inclusions ensured excellent mechanical properties in PBF-built Alloy 718 [35]. Recent studies also emphasized the significant dangers from the surface and sub-surface inclusions in the high plastic damage zone near the crack tip, resulting in a very short LCF life [162]. The non-metallic inclusions are of greater concern if they cluster during any manufacturing steps [59]. The formation mechanisms of the defects, such as pores (shrinkage, or round-shaped), and the LoF defects in PBF-built Alloy 718 have been already investigated [170,129,244-246]; however, the formation mechanisms of the inclusions and how they can decrease fatigue life of PBF-built Alloy 718 have been less studied. Therefore, fundamental analysis of the origins of the inclusions, and thus, the low fatigue lives are demanding.

One of the great potentials of PBF is the possibility to manufacture parts with tailored and site-specific microstructures, hence achieving controlled mechanical properties [92,94,95,247,248]. The transition from columnar to equiaxed microstructures has been performed primarily by changing the process parameters and melting strategies to govern the thermal gradient and solidification rate [91-95]. Disrupting the strong thermal gradient observed in PBF assists the transition [249]. The faster cooling at the melt pool bottom, the grain detachment due to partially-melted grains at the melt pool boundaries, and the dendrite fragmentation due to the vigorous motion in the melt pools were potential assumptions for the nucleation of equiaxed grains [250]. Besides controlling the level of anisotropy via the above transition, the possibility of having site-specific grain size is also critical to modify the local mechanical properties.

Thermal post-treatments are implemented on PBF-built Alloy 718 to eliminate defects, elemental segregations, residual stress, detrimental phases and consequently achieve an enhanced functional performance required for a specific application [37,112]. The thermal post-treatments can change grain size, grain orientation, precipitate phases, pores, and consequently fatigue life. During the thermal post-treatments, grains are generally affected through recovery, recrystallization, and growth (or any combination of these), whereas the phases are affected through dissolution, precipitation, and growth (or any combination of these). While there is no well-developed thermal post-treatment standard for the PBF-built parts, PBF-built Alloy 718 is commonly subjected to a set of thermal post-treatments, including stress relief (SR), hot isostatic pressing (HIP), solution treatment (ST), and aging, such as direct aging (DA), single or double-step aging [84]. The selection of the individual post-treatment is based on the initial microstructure, the level of defects, residual stress in the as-built condition, and the printed part application; therefore, not every step of the above thermal post-treatment is necessarily required for a specific AM-built part. The microstructure of wrought and cast Alloy 718 has already been shown to be very different from that of AM-built Alloy 718 due to different thermal history; however, the thermal post-treatment procedures for such materials are borrowed from the standards developed for the wrought and cast materials. Recently, ASTM (F3055) has established standard specification for heat treatment of the PBF-built Ni-based alloys [251]. In general, to design AM-specific post-treatment standards for Alloy 718, a detailed understanding of the effect of each post-treatment step on a specific microstructure to achieve desired properties for a given application is highly demanding. It is worth noting that different applications need different properties. For instance, the turbine blades need superior creep and fatigue performances, whereas the aerospace fasteners need high tensile and shear strength. Therefore, it is critical to control the mechanical properties using a proper thermal post-treatment according to the given application. However, the underlaying mechanism on how the thermal post-treatments affect fatigue life of PBF-built Alloy 718 remains unclear at present and need further investigation.

As mentioned earlier, the PBF technology can ensure achieving a controlled microstructure with enhanced fatigue life. However, the PBF-built Alloy 718 parts are still susceptible to embrittling elements, such as hydrogen and sulfur [252]. The crack growth can be accelerated by chemical interaction with such embrittling elements in the atmosphere [253,254]. Several studies showed that the microstructural features, such as the grain boundary δ phase in Alloy 718, act as a trap for hydrogen and serve as a site for strain localization; thus, the de-cohesion along grain boundaries subsequently the ductility loss is accelerated. Therefore, attempts have been performed on Alloy 718 to eliminate the δ phase during manufacturing or post-processing. Recent studies reported that the size/volume fraction of γ' and γ'' also play a critical role [7]. The size of γ'' can be controlled during PBF or thermal post-treatment, making Alloy 718 more versatile by changing its susceptibility to hydrogen embrittlement [7]. The impact of grain structure, texture, and anisotropy on the hydrogen embrittlement susceptibility in PBF-built Alloy 718 has not been investigated and requires further exploration.

Non-destructive evaluations (NDE) add a great possibility to investigate crack initiation and growth in materials, including the PBF-built parts. Reid et al. [255] used neutron and synchrotron X-ray tomography. The neutron tomography provided a 3D image in which the crack was detectable. Neutron tomography has a lower spatial resolution than that of X-ray synchrotron tomography and needs a longer acquisition time; however, neutron tomography is more sensitive to the chemistry and useful in part size measurement. A combination of neutron and synchrotron X-ray tomography analysis can be beneficial in analyzing three-dimensional plastic strain. Neikter et al. [256] used X-ray CT to analyze defects, such as the LoF defects and non-metallic inclusions. X-ray CT, with its high spatial resolution, was utilized to characterize fine inclusions down to 150 nm in diameter. Cakmak et al. [257] used *in-situ* neutron diffraction to analyze the distribution of stresses during elastic loading in geometrically complex theta-shaped Alloy 718 parts built via EB-PBF. The *in-situ* loading showed the stresses undergone by the cross-members of the part gradually enhanced in tensile mode with increasing load levels as the theta-shaped parts were under compression. Sheridan et al. [142] developed a new finite life prediction model, which is dependent on both applied stress and defect size. In this model, a threshold defect size for a given stress value that a PBF-built part

can have a finite life is identified. NDE of the PBF-built parts can look for defects greater than a critical size based on this threshold value. The applicability of common NDE methods for textured PBF-built Alloy 718 with the columnar grain morphology should be appreciated, particularly if the printed parts are used as spare parts for replacing the conventionally manufactured parts. This enables engineers to find the limit of detection for the PBF-built materials and alter the inspection period for damage tolerant designs in the aircraft structures.

Multi-axial loads, e.g., in-phase (proportional) or out-of-phase (non-proportional), are typically experienced by many parts in industries, such as automotive, aerospace, and power generation [258]. Due to geometrical constraints at notches, the multi-axial stresses (i.e., in-phase stresses) can be found even under uniaxial loads. Because many of the distinguishing features of the PBF-built Alloy 718 parts are directional, the multi-axial fatigue studies are extremely important for a better understanding of fatigue performance [259]. There has been a limited number of investigations addressing the multi-axial fatigue life of PBF-built Alloy 718. The subject is of greater importance when considering the common features predominant in the PBF-built Alloy 718 parts. The dominant characteristics are multi-axial stress states at critical locations due to the geometrical complexities of the parts, multi-directional residual stress resulted from the manufacturing process, and directionality (or anisotropy) in the microstructure. Moreover, Alloy 718 can be used in applications where torsional forces are concerned [260]. To precisely model the multi-axial fatigue life, the torsional properties must be considered, particularly for the PBF-built parts with anisotropic behavior. The studies on the torsional fatigue behavior of PBF-built Alloy 718 are very limited [261] and need further investigations.

Besides exploiting the PBF techniques to produce the entire part, PBF, particularly LB-PBF, has been very promising for repair [18]. LB-PBF has been an effective process, particularly when the geometry of the part is complex. For instance, significant attention has been put into the implementation of PBF in the repair of the compressor or turbine blades in the energy sectors. Nevertheless, the limitations and challenges of PBF, particularly EB-PBF, need further research and development, particularly when the fatigue life of the repaired parts is concerned.

Despite common applications of Alloy 718 at elevated temperatures, extensive research has been performed on the room temperature fatigue behavior of the PBF-built parts. It has been shown that surface roughness is the most affecting feature on fatigue life at room temperature following by the subsurface and internal defects and secondary phases. However, the effects of these features at high temperatures have not been fully explored yet. The evolution of microstructural features, such as residual stress relaxation, changes in dislocations density, precipitates and second phases coarsening or dissolution, recrystallization and grain growth should be investigated in detail to shed light on the high-temperature cyclic behavior of PBF Alloy 718. The influence of heat-treatment procedure on the high-temperature fatigue response of Alloy 718 manufactured via PBF has not been studied vigorously yet. In addition, the actual high-temperature operation conditions of Alloy 718 necessitate thermomechanical fatigue (TMF) investigations before replacing the conventionally manufactured parts with the PBF-processed ones. It should be noted that during TMF, testing temperature variation is happening simultaneously by straining, and fatigue crack growth is more complicated than the pure fatigue cracks growth due to time-dependent material behavior characteristics, such as creep deformation and oxidation.

Because fatigue is the primary failure mechanism in most engineering components and structures, accurate fatigue life prediction is crucial. Several models have been established for the fatigue life prediction based on the fatigue damage developed at each cycle. Strain- and energy-based fatigue models are among the widely-used models for fatigue life prediction, relating the half-life stabilized material's response to fatigue lives. On the other hand, fracture mechanics-based models establish a relationship between process defects and observed lives. AM specimens are commonly associated with high scatter in the fatigue response compared to the conventionally manufactured samples. This is usually due to the internal defects found in the AM specimens. High scatter in experimental data affects the modeling approaches as the models cannot accurately predict the fatigue response. However, it should be mentioned that specimens manufactured with the optimized process parameters result in low scatter as observed with conventionally manufactured specimens. On the other hand, as long as the manufacturing conditions are not optimized, various types of defects (gas pores and LoF defects) could be present in the test specimens, and the fatigue crack can initiate from each of them. This can lead to high scatter in fatigue lives and cause misunderstanding in interpreting the fatigue test results. Therefore, to improve the fatigue model predictions, the first attempt should be process optimization to minimize the volume fraction of defects. The applicability of well-developed fatigue models and the need for developing more sophisticated fatigue models considering different features of the specimens could be the topics of further investigations.

7. Concluding remarks

The paper addresses the fatigue performance of Alloy 718 built via powder bed fusion (PBF) techniques, including electron- and laser-beam PBF (EB- and LB-PBF), and presents an extensive overview of the mechanisms that result in the fatigue failure. The effects of feedstock powder, manufacturing process, process parameters, part geometry, build layout and orientation, phases, residual stress, grain structure including morphology and texture, as well as loading mode, thermal and mechanical post processes on the fatigue life of PBF-built Alloy 718 were reviewed. Despite some differences in the microstructure, PBF-built Alloy 718 can sustain the cyclic loading condition in service life similar to wrought and cast Alloy 718. The PBF-built Alloy 718 parts with excellent fatigue resistance can be developed by optimizing the process parameters or post-treatment.

While the already-developed fatigue theories can be used for the PBF-built parts, the fundamental differences between the conventionally-built and AM Alloy 718 need to be better understood. It is demanding to implement a combination of ordinary and advanced characterization techniques to explore the fatigue response of the PBF-built Alloy 718. The effect of the volume fraction of the δ phase, as well as the presence of the Laves phase and NbC precipitates, was negligible on the fatigue performance up to a certain life. However, the grain morphology of the γ matrix, as well as the presence of the γ''/γ' precipitates and δ phase directly or indirectly

affected the fatigue behavior.

The geometry, morphology, distribution, and orientation of internal (bulk-related) and external (surface-related) defects showed a severe effect on the fatigue life of PBF-built Alloy 718 due to the significant stress concentrations. In the as-built condition, the notch-like features and surface irregularities, such as surface roughness, as well as surface and sub-surface inclusions, were the crack initiation sites (with stress concentration), and therefore, the primary reason for early failure. The high frequency of the crack initiation sites at the surface results in a lower scatter in the fatigue life. The results highlighted the significance of surface topography assessment in analyzing fatigue performance. The surface defects were dominant in fatigue life of the as-built parts; therefore, no positive effect of thermal post-processing on fatigue life in the as-built condition was reported.

However, the fatigue strength of PBF-built Alloy 718 showed a great improvement after surface machining and polishing. In the machined parts, the process-induced defects, including (e.g., round, and semi-round shape pores, shrinkage pores, and LoF defects) and columnar grains (facets) identified in the microstructure, facilitated the cracks. The LoF defects and non-metallic inclusions served as crack initiation sites, whereas the shrinkage pores (due to a uniform distribution) enhanced the crack growth. The LoF defects, particularly when oriented perpendicular to the build direction, were among the major reasons for the low fatigue life of PBF-built Alloy 718. Proper post-processing treatments need to be developed to substantially enhance damage tolerance and, eventually, in-service properties. For instance, HIP can heal most internal defects and to improve fatigue life; however, inclusion-containing defects are unaffected by HIP, which can still act as a crack initiation site. In general, thermal and mechanical post-treatments are recommended to achieve a fully functional PBF-built part.

The $\langle 1\,0\,0 \rangle$ fiber texture along the build direction led to the anisotropic elastic modulus. Therefore, anisotropic behavior in the fatigue life under strain-controlled conditions was reported (i.e., longer fatigue life along the low elastic modulus direction). The pseudo-elastic stress versus life could be plotted to understand the effect of anisotropy. Such anisotropic behavior of PBF-built Alloy 718 can be eliminated by modifying the standard heat-treatment procedures currently used for wrought and cast Alloy 718. Challenges still exist in enhancing the productivity of the PBF processes and lowering the cost of manufacturing high-quality feedstock powders while increasing the fatigue performance of the PBF-built parts. A better understanding of the PBF processes is required for greater adaptation of the processes in the industry. Understanding the entire feedstock powder-process-microstructure-properties-performance relationship can be greatly useful to lead future process parameter optimization activities and inform the qualification strategy for linking the fatigue test data to parts experienced different thermal histories.

Declaration of Competing Interest

The authors declare that they have no known competing financial interests or personal relationships that could have appeared to influence the work reported in this paper.

Data availability

No data was used for the research described in the article.

References

[1] Attallah MM, Jennings R, Wang X, Carter LN. Additive manufacturing of Ni-based superalloys: The outstanding issues. MRS Bull 2016;41(10):758–64.
[2] Donachie MJ, Donachie SJ. Superalloys: a technical guide. ASM International 2002.
[3] Gibson I, Rosen D, Stucker B. Additive Manufacturing Technologies: 3D Printing, Rapid Prototyping, and Direct Digital Manufacturing, 2nd ed. New York: Springer-Verlag, 2015. Accessed: May 11, 2019. [Online]. Available: https://www.springer.com/gp/book/9781493921126.
[4] Sanchez S, et al. Powder bed fusion of nickel-based superalloys: A review. Int J Mach Tools Manuf Jun. 2021;165:103729. https://doi.org/10.1016/j.ijmachtools.2021.103729.
[5] Thompson MK, et al. Design for additive manufacturing: Trends, opportunities, considerations, and constraints. CIRP Ann Jan. 2016;65(2):737–60. https://doi.org/10.1016/j.cirp.2016.05.004.
[6] Huang R, et al. Energy and emissions saving potential of additive manufacturing: the case of lightweight aircraft components. J Clean Prod Nov. 2016;135:1559–70. https://doi.org/10.1016/j.jclepro.2015.04.109.
[7] DebRoy T, et al. Additive manufacturing of metallic components – Process, structure and properties. Prog Mater Sci Mar. 2018;92:112–224. https://doi.org/10.1016/j.pmatsci.2017.10.001.
[8] Harrison NJ, Todd I, Mumtaz K. Reduction of micro-cracking in nickel superalloys processed by selective laser melting: A fundamental alloy design approach. Acta Mater Aug. 2015;94:59–68. https://doi.org/10.1016/j.actamat.2015.04.035.
[9] Deng D, Peng RL, Brodin H, Moverare J. Microstructure and mechanical properties of Inconel 718 produced by selective laser melting: Sample orientation dependence and effects of post heat treatments. Mater Sci Eng A Jan. 2018;713:294–306. https://doi.org/10.1016/j.msea.2017.12.043.
[10] Radhakrishnan J, Kumar P, Li S, Zhao Y, Ramamurty U. Unnotched fatigue of Inconel 718 produced by laser beam-powder bed fusion at 25 and 600°C. Acta Mater Feb. 2022;225:117565. https://doi.org/10.1016/j.actamat.2021.117565.
[11] Gallmeyer TG, Moorthy S, Kappes BB, Mills MJ, Amin-Ahmadi B, Stebner AP. Knowledge of process-structure-property relationships to engineer better heat treatments for laser powder bed fusion additive manufactured Inconel 718. Addit Manuf Jan. 2020;31:100977. https://doi.org/10.1016/j.addma.2019.100977.
[12] Findlay SJ, Harrison ND. Why aircraft fail. Mater Today Nov. 2002;5(11):18–25. https://doi.org/10.1016/S1369-7021(02)01138-0.
[13] Hovig EW, Azar AS, Sunding MF, Andreassen E, Sørby K. High cycle fatigue life estimation of materials processed by laser powder bed fusion. Fatigue Fract Eng Mater Struct 2019;42(7):1454–66. https://doi.org/10.1111/ffe.12982.
[14] Sheridan L, Gockel JE, Scott-Emuakpor OE. Primary processing parameters, porosity production, and fatigue prediction for additively manufactured alloy 718. J Mater Eng Perform, vol. 28, no. 9, Art. no. 9, Sep. 2019, doi: 10.1007/s11665-019-04305-7.
[15] Witkin DB, Patel D, Albright TV, Bean GE, McLouth T. Influence of surface conditions and specimen orientation on high cycle fatigue properties of Inconel 718 prepared by laser powder bed fusion. Int J Fatigue Mar. 2020;132:105392. https://doi.org/10.1016/j.ijfatigue.2019.105392.
[16] Sadeghi M, Diaz A, McFadden P, Sadeghi E. Chemical and mechanical post-processing of Alloy 718 built via electron beam-powder bed fusion: Surface texture and corrosion behavior. Mater Des Feb. 2022;214:110405. https://doi.org/10.1016/j.matdes.2022.110405.

[17] Beese AM, Carroll BE. Review of mechanical properties of Ti-6Al-4V made by laser-based additive manufacturing using powder feedstock. JOM 2016;68(3):724–34.
[18] Fayazfar H, et al. A critical review of powder-based additive manufacturing of ferrous alloys: Process parameters, microstructure and mechanical properties. Mater Des Apr. 2018;144:98–128. https://doi.org/10.1016/j.matdes.2018.02.018.
[19] Hosseini E, Popovich VA. A review of mechanical properties of additively manufactured Inconel 718. Addit Manuf Dec. 2019;30:100877. https://doi.org/10.1016/j.addma.2019.100877.
[20] Kok Y, et al. Anisotropy and heterogeneity of microstructure and mechanical properties in metal additive manufacturing: A critical review. Mater Des Feb. 2018;139:565–86. https://doi.org/10.1016/j.matdes.2017.11.021.
[21] Lewandowski JJ, Seifi M. Metal additive manufacturing: a review of mechanical properties. Annu Rev Mater Res Jul. 2016;46(1):151–86. https://doi.org/10.1146/annurev-matsci-070115-032024.
[22] Yadollahi A, Shamsaei N. Additive manufacturing of fatigue resistant materials: Challenges and opportunities. Int J Fatigue May 2017;98:14–31. https://doi.org/10.1016/j.ijfatigue.2017.01.001.
[23] Laleh M, et al. Heat treatment for metal additive manufacturing. Prog Mater Sci 2022.
[24] Durand-Charre M. The microstructure of superalloys. CRC Press; 1998.
[25] Li X, et al. Effect of heat treatment on microstructure evolution of Inconel 718 alloy fabricated by selective laser melting. J Alloys Compd Oct. 2018;764:639–49. https://doi.org/10.1016/j.jallcom.2018.06.112.
[26] Pröbstle M, et al. Superior creep strength of a nickel-based superalloy produced by selective laser melting. Mater Sci Eng A Sep. 2016;674:299–307. https://doi.org/10.1016/j.msea.2016.07.061.
[27] Deng D. On the microstructures and anisotropic mechanical behaviours of additively manufactured IN718, 2019, Accessed: Aug. 12, 2020. [Online]. Available: http://urn.kb.se/resolve?urn=urn:nbn:se:liu:diva-161706.
[28] Azadian S. Aspects of precipitation in alloy inconel 718. Doctoral Thesis, Luleå Tekniska Universitet, 2004. Accessed: May 09, 2019. [Online]. Available: http://muep.mau.se/handle/2043/4919.
[29] Ghorbanpour S, et al. Experimental characterization and crystal plasticity modeling of anisotropy, tension-compression asymmetry, and texture evolution of additively manufactured Inconel 718 at room and elevated temperatures. Int J Plast Feb. 2020;125:63–79. https://doi.org/10.1016/j.ijplas.2019.09.002.
[30] Sims CT, Stoloff NS, Hagel WC. *Superalloys II*. New York: Wiley, 1987. Accessed: Aug. 10, 2020. [Online]. Available: http://books.google.com/books?id=kqZTAAAAMAAJ.
[31] Sames WJ, Unocic KA, Dehoff RR, Lolla T, Babu SS. Thermal effects on microstructural heterogeneity of Inconel 718 materials fabricated by electron beam melting. J Mater Res Sep. 2014;29(17):1920–30. https://doi.org/10.1557/jmr.2014.140.
[32] Desvallees Y, Bouzidi M, Bois F, Beaude N. Delta phase in INCONEL 718: mechanical properties and forging process requirements. 1994, pp. 281–291. doi: 10.7449/1994/Superalloys_1994_281_291.
[33] Schirra JJ, Caless RH, Hatala R. The effect of laves phase on the mechanical properties of wrought and cast + HIP inconel 718. 1991, doi: 10.7449/1991/SUPERALLOYS_1991_375_388.
[34] Chen Y, Zhang K, Huang J, Hosseini SRE, Li Z. Characterization of heat affected zone liquation cracking in laser additive manufacturing of Inconel 718. Mater Des Jan. 2016;90:586–94. https://doi.org/10.1016/j.matdes.2015.10.155.
[35] Deng D, Moverare J, Peng RL, Söderberg H. Microstructure and anisotropic mechanical properties of EBM manufactured Inconel 718 and effects of post heat treatments. Mater Sci Eng A May 2017;693:151–63. https://doi.org/10.1016/j.msea.2017.03.085.
[36] Amato KN, et al. Microstructures and mechanical behavior of Inconel 718 fabricated by selective laser melting. Acta Mater Mar. 2012;60(5):2229–39. https://doi.org/10.1016/j.actamat.2011.12.032.
[37] Wang Z, Guan K, Gao M, Li X, Chen X, Zeng X. The microstructure and mechanical properties of deposited-IN718 by selective laser melting. J Alloys Compd Feb. 2012;513:518–23. https://doi.org/10.1016/j.jallcom.2011.10.107.
[38] Lawitzki R, et al. Differentiation of γ′- and γ″- precipitates in Inconel 718 by a complementary study with small-angle neutron scattering and analytical microscopy. Acta Mater Jan. 2019;163:28–39. https://doi.org/10.1016/j.actamat.2018.10.014.
[39] Jiang R, et al. Effect of heat treatment on microstructural evolution and hardness homogeneity in laser powder bed fusion of alloy 718. Addit Manuf Oct. 2020;35:101282. https://doi.org/10.1016/j.addma.2020.101282.
[40] Dowling L, Kennedy J, O'Shaughnessy S, Trimble D. A review of critical repeatability and reproducibility issues in powder bed fusion. Mater Des Jan. 2020;186:108346. https://doi.org/10.1016/j.matdes.2019.108346.
[41] Yin J, et al. High-power laser-matter interaction during laser powder bed fusion. Addit Manuf Oct. 2019;29:100778. https://doi.org/10.1016/j.addma.2019.100778.
[42] Smith CJ, Tammas-Williams S, Hernandez-Nava E, Todd I. Tailoring the thermal conductivity of the powder bed in Electron Beam Melting (EBM) Additive Manufacturing. Sci Rep, vol. 7, no. 1, Art. no. 1, Sep. 2017, doi: 10.1038/s41598-017-11243-8.
[43] Scime L, Beuth J. Melt pool geometry and morphology variability for the Inconel 718 alloy in a laser powder bed fusion additive manufacturing process. Addit Manuf Oct. 2019;29:100830. https://doi.org/10.1016/j.addma.2019.100830.
[44] Scime L, Beuth J. Using machine learning to identify in-situ melt pool signatures indicative of flaw formation in a laser powder bed fusion additive manufacturing process. Addit Manuf Jan. 2019;25:151–65. https://doi.org/10.1016/j.addma.2018.11.010.
[45] Sames WJ, Medina F, Peter WH, Babu SS, Dehoff RR. Effect of process control and powder quality on inconel 718 produced using electron beam melting. 8th International Symposium on Superalloy 718 and Derivatives, John Wiley & Sons Ltd 2014:409–23. https://doi.org/10.1002/9781119016854.ch32.
[46] Presley MA, Christensen PR. Thermal conductivity measurements of particulate materials: 5. Effect of bulk density and particle shape. J Geophys Res Planets, vol. 115, no. E7, 2010, doi: 10.1029/2009JE003483.
[47] Qiu C, Panwisawas C, Ward M, Basoalto HC, Brooks JW, Attallah MM. On the role of melt flow into the surface structure and porosity development during selective laser melting. Acta Mater Sep. 2015;96:72–9. https://doi.org/10.1016/j.actamat.2015.06.004.
[48] Chan LC, Page NW. Particle fractal and load effects on internal friction in powders. Powder Technol 1997;90(3):259–66.
[49] Clayton J. Optimising metal powders for additive manufacturing. Met Powder Rep Sep. 2014;69(5):14–7. https://doi.org/10.1016/S0026-0657(14)70223-1.
[50] Strondl A, Lyckfeldt O, Brodin H, Ackelid U. Characterization and control of powder properties for additive manufacturing. JOM, vol. 67, no. 3, Art. no. 3, Mar. 2015, doi: 10.1007/s11837-015-1304-0.
[51] Soltani-Tehrani A, Pegues J, Shamsaei N. Fatigue behavior of additively manufactured 17–4 PH stainless steel: The effects of part location and powder re-use. Addit Manuf Dec. 2020;36:101398. https://doi.org/10.1016/j.addma.2020.101398.
[52] Sadeghi E, Karimi P, Israelsson N, Shipley J, Månsson T, Hansson T. Inclusion-induced fatigue crack initiation in powder bed fusion of Alloy 718. J Addit Manuf 2020;36.
[53] Gruber H, Henriksson M, Hryha E, Nyborg L. Effect of powder recycling in electron beam melting on the surface chemistry of alloy 718 powder. Metall Mater Trans A Sep. 2019;50(9):4410–22. https://doi.org/10.1007/s11661-019-05333-7.
[54] Kumar M, Balasubramanian TV, Misra RDK. On the characterization of inert-gas atomized nickel-based superalloy powders. J Mater Sci Lett Feb. 1990;9(2):147–51. https://doi.org/10.1007/BF00727699.
[55] Gruber H, Luchian C, Hryha E, Nyborg L. Effect of powder recycling on defect formation in electron beam melted alloy 718. Metall Mater Trans A May 2020;51(5):2430–43. https://doi.org/10.1007/s11661-020-05674-8.
[56] Sames W. Additive manufacturing of Inconel 718 using electron beam melting: Processing, post-processing, & Mechanical properties, PhD Thesis, 2015.
[57] Texier D, et al. Crack initiation sensitivity of wrought direct aged alloy 718 in the very high cycle fatigue regime: the role of non-metallic inclusions. Mater Sci Eng A Dec. 2016;678:122–36. https://doi.org/10.1016/j.msea.2016.09.098.
[58] Ogawahara M, Sasaki S. Effects of defects and inclusions on the fatigue properties of inconel 718 fabricated by laser powder bed fusion followed by HIP. Mater Trans 2021;62(5):631–5. https://doi.org/10.2320/matertrans.Y-M2021804.

[59] Cockcroft S, Degawa T, Mitchell A, Tripp DW, Schmalz AJ. Inclusion precipitation in superalloys, 1992. doi: 10.7449/1992/Superalloys_1992_577_586.
[60] Denda T, Bretz PL, Tien JK. Inclusion size effect on the fatigue crack propagation mechanism and fracture mechanics of a superalloy. Metall Trans A Feb. 1992; 23(2):519–26. https://doi.org/10.1007/BF02801169.
[61] Ardi DT, Guowei L, Maharjan N, Mutiargo B, Leng SH, Srinivasan R. Effects of post-processing route on fatigue performance of laser powder bed fusion Inconel 718. Addit Manuf Dec. 2020;36:101442. https://doi.org/10.1016/j.addma.2020.101442.
[62] Chandrasekar S, et al. Investigating the effect of metal powder recycling in Electron beam Powder Bed Fusion using process log data. Addit Manuf Mar. 2020; 32:100994. https://doi.org/10.1016/j.addma.2019.100994.
[63] Georgilas K, Khan RHU, Kartal ME. The influence of pulsed laser powder bed fusion process parameters on Inconel 718 material properties. Mater Sci Eng A Jan. 2020;769:138527. https://doi.org/10.1016/j.msea.2019.138527.
[64] Hilaire A, Andrieu E, Wu X. High-temperature mechanical properties of alloy 718 produced by laser powder bed fusion with different processing parameters. Addit Manuf Mar. 2019;26:147–60. https://doi.org/10.1016/j.addma.2019.01.012.
[65] Kim S, Choi H, Lee J, Kim S. Room and elevated temperature fatigue crack propagation behavior of Inconel 718 alloy fabricated by laser powder bed fusion. Int J Fatigue Nov. 2020;140:105802. https://doi.org/10.1016/j.ijfatigue.2020.105802.
[66] Kim SK, Lee YD, Hansson K, Fredriksson H. Influence of cooling rate on the hot cracking formation of nickel rich alloys. ISIJ Int 2002;42(5):5. https://doi.org/10.2355/isijinternational.42.512.
[67] Knapp GL, Raghavan N, Plotkowski A, DebRoy T. Experiments and simulations on solidification microstructure for Inconel 718 in powder bed fusion electron beam additive manufacturing. Addit Manuf Jan. 2019;25:511–21. https://doi.org/10.1016/j.addma.2018.12.001.
[68] Wang X, Chou K. The effects of stress relieving heat treatment on the microstructure and residual stress of Inconel 718 fabricated by laser metal powder bed fusion additive manufacturing process. J Manuf Process Dec. 2019;48:154–63. https://doi.org/10.1016/j.jmapro.2019.10.027.
[69] Watring DS, Carter KC, Crouse D, Raeymaekers B, Spear AD. Mechanisms driving high-cycle fatigue life of as-built Inconel 718 processed by laser powder bed fusion. Mater Sci Eng A Jul. 2019;761:137993. https://doi.org/10.1016/j.msea.2019.06.003.
[70] Watring DS, Benzing JT, Hrabe N, Spear AD. Effects of laser-energy density and build orientation on the structure–property relationships in as-built Inconel 718 manufactured by laser powder bed fusion. Addit Manuf Dec. 2020;36:101425. https://doi.org/10.1016/j.addma.2020.101425.
[71] Marques A, et al. Inconel 718 produced by laser powder bed fusion: an overview of the influence of processing parameters on microstructural and mechanical properties. Int J Adv Manuf Technol Aug. 2022;121(9):5651–75. https://doi.org/10.1007/s00170-022-09693-0.
[72] Murr LE, et al. Metal fabrication by additive manufacturing using laser and electron beam melting technologies. J Mater Sci Technol Jan. 2012;28(1):1–14. https://doi.org/10.1016/S1005-0302(12)60016-4.
[73] Sing SL, An J, Yeong WY, Wiria FE. Laser and electron-beam powder-bed additive manufacturing of metallic implants: A review on processes, materials and designs. J Orthop Res Off Publ Orthop Res Soc Mar. 2016;34(3):369–85. https://doi.org/10.1002/jor.23075.
[74] Körner C, Bauereiß A, Attar E. Fundamental consolidation mechanisms during selective beam melting of powders. Model Simul Mater Sci Eng Nov. 2013;21(8): 085011. https://doi.org/10.1088/0965-0393/21/8/085011.
[75] Popovich VA, Borisov EV, Popovich AA, Sufiiarov VS, Masaylo DV, Alzina L. Impact of heat treatment on mechanical behaviour of Inconel 718 processed with tailored microstructure by selective laser melting. Mater Des Oct. 2017;131:12–22. https://doi.org/10.1016/j.matdes.2017.05.065.
[76] Rafi HK, Karthik NV, Gong H, Starr TL, Stucker BE. Microstructures and mechanical properties of Ti6Al4V parts fabricated by selective laser melting and electron beam melting. J Mater Eng Perform Dec. 2013;22(12):3872–83. https://doi.org/10.1007/s11665-013-0658-0.
[77] Carolo LCB, Cooper O RE. A review on the influence of process variables on the surface roughness of Ti-6Al-4V by electron beam powder bed fusion. Addit Manuf, vol. 59, p. 103103, Nov. 2022, doi: 10.1016/j.addma.2022.103103.
[78] Gong H, et al. Melt pool characterization for selective laser melting of Ti-6Al-4V pre-alloyed powder. In: Solid freeform fabrication symposium, 2014, pp. 256–267.
[79] Gong H, Rafi K, Gu H, Starr T, Stucker B. Analysis of defect generation in Ti–6Al–4V parts made using powder bed fusion additive manufacturing processes. Addit Manuf Oct. 2014;1–4:87–98. https://doi.org/10.1016/j.addma.2014.08.002.
[80] Herzog D, Seyda V, Wycisk E, Emmelmann C. Additive manufacturing of metals. Acta Mater Sep. 2016;117:371–92. https://doi.org/10.1016/j.actamat.2016.07.019.
[81] Mostafa A, Picazo Rubio I, Brailovski V, Jahazi M, Medraj M. Structure, texture and phases in 3D printed IN718 alloy subjected to homogenization and HIP treatments. Metals Jun. 2017;7(6):6. https://doi.org/10.3390/met7060196.
[82] Muhammad M, Frye P, Simsiriwong J, Shao S, Shamsaei N. An investigation into the effects of cyclic strain rate on the high cycle and very high cycle fatigue behaviors of wrought and additively manufactured Inconel 718. Int J Fatigue Mar. 2021;144:106038. https://doi.org/10.1016/j.ijfatigue.2020.106038.
[83] Tucho WM, Cuvillier P, Sjolyst-Kverneland A, Hansen V. Microstructure and hardness studies of Inconel 718 manufactured by selective laser melting before and after solution heat treatment. Mater Sci Eng A Mar. 2017;689:220–32. https://doi.org/10.1016/j.msea.2017.02.062.
[84] Zhang D, Niu W, Cao X, Liu Z. Effect of standard heat treatment on the microstructure and mechanical properties of selective laser melting manufactured Inconel 718 superalloy. Mater Sci Eng A Sep. 2015;644:32–40. https://doi.org/10.1016/j.msea.2015.06.021.
[85] He M, Xiang Z, Yi J, Ni Y, Wang S. A comparison of dislocation cellular patterns generated in Inconel 718 alloy and pure Ni fabricated by laser powder bed fusion. Vacuum May 2022;199:110974. https://doi.org/10.1016/j.vacuum.2022.110974.
[86] He M, Cao H, Liu Q, Yi J, Ni Y, Wang S. Evolution of dislocation cellular pattern in Inconel 718 alloy fabricated by laser powder-bed fusion. Addit Manuf Jul. 2022;55:102839. https://doi.org/10.1016/j.addma.2022.102839.
[87] Parab ND, et al. High-speed synchrotron X-ray imaging of laser powder bed fusion process. Synchrotron Radiat News Mar. 2019;32(2):4–8. https://doi.org/10.1080/08940886.2019.1582280.
[88] Jia Q, Gu D. Selective laser melting additive manufacturing of Inconel 718 superalloy parts: Densification, microstructure and properties. J Alloys Compd Feb. 2014;585:713–21. https://doi.org/10.1016/j.jallcom.2013.09.171.
[89] Keshavarzkermani A, et al. An investigation into the effect of process parameters on melt pool geometry, cell spacing, and grain refinement during laser powder bed fusion. Opt Laser Technol Aug. 2019;116:83–91. https://doi.org/10.1016/j.optlastec.2019.03.012.
[90] Karimi P, Sadeghi E, Ålgårdh J, Andersson J. EBM-manufactured single tracks of Alloy 718: Influence of energy input and focus offset on geometrical and microstructural characteristics. Mater Charact 2019;148:88–99.
[91] Ding X, et al. Microstructural control of alloy 718 fabricated by electron beam melting with expanded processing window by adaptive offset method. Mater Sci Eng A Sep. 2019;764:138058. https://doi.org/10.1016/j.msea.2019.138058.
[92] Kirka MM, et al. Strategy for Texture Management in Metals Additive Manufacturing. JOM Mar. 2017;69(3):523–31. https://doi.org/10.1007/s11837-017-2264-3.
[93] Parimi LL, A RG, Clark D, Attallah MM. Microstructural and texture development in direct laser fabricated IN718. Mater Charact, vol. 89, pp. 102–111, Mar. 2014, doi: 10.1016/j.matchar.2013.12.012.
[94] Dehoff RR, Kirka MM, List FA, Unocic KA, Sames WJ. Crystallographic texture engineering through novel melt strategies via electron beam melting: Inconel 718. Mater Sci Technol Jun. 2015;31(8):939–44. https://doi.org/10.1179/1743284714Y.0000000697.
[95] Dehoff RR, et al. Site specific control of crystallographic grain orientation through electron beam additive manufacturing. Mater Sci Technol Jun. 2015;31(8): 931–8. https://doi.org/10.1179/1743284714Y.0000000734.
[96] Raghavan S, et al. Effect of different heat treatments on the microstructure and mechanical properties in selective laser melted INCONEL 718 alloy. Mater Manuf Process Oct. 2017;32(14):1588–95. https://doi.org/10.1080/10426914.2016.1257805.
[97] Popovich VA, Borisov EV, Popovich AA, Sufiiarov VS, Masaylo DV, Alzina L. Functionally graded Inconel 718 processed by additive manufacturing: Crystallographic texture, anisotropy of microstructure and mechanical properties. Mater Des Jan. 2017;114:441–9. https://doi.org/10.1016/j.matdes.2016.10.075.

[98] Yang K, Huang Q, Wang Q, Chen Q. Competing crack initiation behaviors of a laser additively manufactured nickel-based superalloy in high and very high cycle fatigue regimes. Int J Fatigue Jul. 2020;136:105580. https://doi.org/10.1016/j.ijfatigue.2020.105580.

[99] Zhao X, Chen J, Lin X, Huang W. Study on microstructure and mechanical properties of laser rapid forming Inconel 718. Mater Sci Eng A Apr. 2008;478(1):119–24. https://doi.org/10.1016/j.msea.2007.05.079.

[100] Kantzos C, Pauza J, Cunningham R, Narra SP, Beuth J, Rollett A. An investigation of process parameter modifications on additively manufactured inconel 718 parts. J Mater Eng Perform Feb. 2019;28(2):2. https://doi.org/10.1007/s11665-018-3612-3.

[101] Kotzem D, Arold T, Niendorf T, Walther F. Influence of specimen position on the build platform on the mechanical properties of as-built direct aged electron beam melted Inconel 718 alloy. Mater Sci Eng A Jan. 2020;772:138785. https://doi.org/10.1016/j.msea.2019.138785.

[102] Li P, Warner DH, Fatemi A, Phan N. Critical assessment of the fatigue performance of additively manufactured Ti–6Al–4V and perspective for future research. Int J Fatigue Apr. 2016;85:130–43. https://doi.org/10.1016/j.ijfatigue.2015.12.003.

[103] Nicoletto G. A novel test method for the fatigue characterization of metal powder bed fused alloys. Procedia Struct Integr Jan. 2017;7:67–74. https://doi.org/10.1016/j.prostr.2017.11.062.

[104] Deng D, Peng RL, Moverare J. On the dwell-fatigue crack propagation behavior of a high strength superalloy manufactured by electron beam melting. Mater Sci Eng A Jul. 2019;760:448–57. https://doi.org/10.1016/j.msea.2019.06.013.

[105] Nicoletto G. Anisotropic high cycle fatigue behavior of Ti–6Al–4V obtained by powder bed laser fusion. Int J Fatigue Jan. 2017;94:255–62. https://doi.org/10.1016/j.ijfatigue.2016.04.032.

[106] Wan HY, et al. Effects of surface roughness and build thickness on fatigue properties of selective laser melted Inconel 718 at 650 °C. Int J Fatigue Aug. 2020;137:105654. https://doi.org/10.1016/j.ijfatigue.2020.105654.

[107] Persenot T, Burr A, Martin G, Buffiere J-Y, Dendievel R, Maire E. Effect of build orientation on the fatigue properties of as-built Electron Beam Melted Ti-6Al-4V alloy. Int J Fatigue Jan. 2019;118:65–76. https://doi.org/10.1016/j.ijfatigue.2018.08.006.

[108] Kotzem D, Arold T, Niendorf T, Walther F. Damage Tolerance Evaluation of E-PBF-Manufactured Inconel 718 Strut Geometries by Advanced Characterization Techniques. Materials Jan. 2020;13(1):1. https://doi.org/10.3390/ma13010247.

[109] Suresh S. Fatigue of Materials, 2nd ed. Cambridge: Cambridge University Press, 1998. doi: 10.1017/CBO9780511806575.

[110] Babamiri BB, Indeck J, Demeneghi G, Cuadra J, Hazeli K. Quantification of porosity and microstructure and their effect on quasi-static and dynamic behavior of additively manufactured Inconel 718. Addit Manuf Aug. 2020;34:101380. https://doi.org/10.1016/j.addma.2020.101380.

[111] Brenne F, et al. Microstructural design of Ni-base alloys for high-temperature applications: impact of heat treatment on microstructure and mechanical properties after selective laser melting. Prog Addit Manuf Dec. 2016;1(3):141–51. https://doi.org/10.1007/s40964-016-0013-8.

[112] Chlebus E, Gruber K, Kuźnicka B, Kurzac J, Kurzynowski T. Effect of heat treatment on the microstructure and mechanical properties of Inconel 718 processed by selective laser melting. Mater Sci Eng A Jul. 2015;639:647–55. https://doi.org/10.1016/j.msea.2015.05.035.

[113] Deng D, Peng RL, Söderberg H, Moverare J. On the formation of microstructural gradients in a nickel-base superalloy during electron beam melting. Mater Des Dec. 2018;160:251–61. https://doi.org/10.1016/j.matdes.2018.09.006.

[114] Kirka MM, Unocic KA, Raghavan N, Medina F, Dehoff RR, Babu SS. Microstructure development in electron beam-melted inconel 718 and associated tensile properties. JOM Mar. 2016;68(3):3. https://doi.org/10.1007/s11837-016-1812-6.

[115] Kirka MM, Greeley DA, Hawkins C, Dehoff RR. Effect of anisotropy and texture on the low cycle fatigue behavior of Inconel 718 processed via electron beam melting. Int J Fatigue Dec. 2017;105:235–43. https://doi.org/10.1016/j.ijfatigue.2017.08.021.

[116] Murr LE. Metallurgy of additive manufacturing: Examples from electron beam melting. Addit Manuf Jan. 2015;5:40–53. https://doi.org/10.1016/j.addma.2014.12.002.

[117] Nadammal N, et al. Effect of hatch length on the development of microstructure, texture and residual stresses in selective laser melted superalloy Inconel 718. Mater Des Nov. 2017;134:139–50. https://doi.org/10.1016/j.matdes.2017.08.049.

[118] Sochalski-Kolbus LM, et al. Comparison of residual stresses in inconel 718 simple parts made by electron beam melting and direct laser metal sintering. Metall Mater Trans A Mar. 2015;46(3):3. https://doi.org/10.1007/s11661-014-2722-2.

[119] Wang X, Keya T, Chou K. Build height effect on the inconel 718 parts fabricated by selective laser melting. Procedia Manuf Jan. 2016;5:1006–17. https://doi.org/10.1016/j.promfg.2016.08.089.

[120] Zhao J-R, Hung F-Y, Lui T-S. Microstructure and tensile fracture behavior of three-stage heat treated inconel 718 alloy produced via laser powder bed fusion process. J Mater Res Technol May 2020;9(3):3357–67. https://doi.org/10.1016/j.jmrt.2020.01.030.

[121] Hagen JF, Rasch M, Kohl S, Schmidt M. Geometry dependent microstructures: bug or feature? Procedia CIRP Jan. 2018;74:724–7. https://doi.org/10.1016/j.procir.2018.08.024.

[122] Lee YS, Zhang W. Modeling of heat transfer, fluid flow and solidification microstructure of nickel-base superalloy fabricated by laser powder bed fusion. Addit Manuf Oct. 2016;12:178–88. https://doi.org/10.1016/j.addma.2016.05.003.

[123] Azadian S, Wei L-Y, Warren R. Delta phase precipitation in Inconel 718. Mater Charact Sep. 2004;53(1):7–16. https://doi.org/10.1016/j.matchar.2004.07.004.

[124] Tao P, Li H, Huang B, Hu Q, Gong S, Xu Q. The crystal growth, intercellular spacing and microsegregation of selective laser melted Inconel 718 superalloy. Vacuum Jan. 2019;159:382–90. https://doi.org/10.1016/j.vacuum.2018.10.074.

[125] Gong X, Chou K. "Microstructures of Inconel 718 by Selective Laser Melting", in *TMS2015 Supplemental Proceedings*. John Wiley & Sons Ltd 2015:461–8. https://doi.org/10.1002/9781119093466.ch58.

[126] Raghavan N, et al. Localized melt-scan strategy for site specific control of grain size and primary dendrite arm spacing in electron beam additive manufacturing. Acta Mater Nov. 2017;140:375–87. https://doi.org/10.1016/j.actamat.2017.08.038.

[127] Sames WJ, et al. Feasibility of in situ controlled heat treatment (ISHT) of Inconel 718 during electron beam melting additive manufacturing. Addit Manuf Jan. 2017;13:156–65. https://doi.org/10.1016/j.addma.2016.09.001.

[128] Zhang F, et al. Effect of heat treatment on the microstructural evolution of a nickel-based superalloy additive-manufactured by laser powder bed fusion. Acta Mater Jun. 2018;152:200–14. https://doi.org/10.1016/j.actamat.2018.03.017.

[129] Karimi P, Sadeghi E, Åkerfeldt P, Ålgårdh J, Andersson J. Influence of successive thermal cycling on microstructure evolution of EBM-manufactured alloy 718 in track-by-track and layer-by-layer design. Mater Des 2018;160:427–41.

[130] Deng D, Peng RL, Moverare J. A comparison study of the dwell-fatigue behaviours of additive and conventional IN718: The role of dislocation substructure on the cracking behaviour. Mater Sci Eng A Oct. 2020;797:140072. https://doi.org/10.1016/j.msea.2020.140072.

[131] Kumara C, Balachandramurthi AR, Goel S, Hanning F, Moverare J. Toward a better understanding of phase transformations in additive manufacturing of Alloy 718. Materialia Sep. 2020;13:100862. https://doi.org/10.1016/j.mtla.2020.100862.

[132] Dinda GP, Dasgupta AK, Mazumder J. Texture control during laser deposition of nickel-based superalloy. Scr Mater Sep. 2012;67(5):503–6. https://doi.org/10.1016/j.scriptamat.2012.06.014.

[133] Zhang B, et al. Mechanical properties and microstructure evolution of selective laser melting Inconel 718 along building direction and sectional dimension. Mater Sci Eng A Sep. 2020;794:139941. https://doi.org/10.1016/j.msea.2020.139941.

[134] Vieille B, et al. Investigations on the fracture behavior of Inconel 718 superalloys obtained from cast and additive manufacturing processes. Mater Sci Eng A Jul. 2020;790:139666. https://doi.org/10.1016/j.msea.2020.139666.

[135] Jayaraj Radhakrishnan R, Kumar P, Seet HL, Nai SML, Wang P, Ramamurty U. Cascading of the as-built microstructure through heat treatment and its role on the tensile properties of laser powder bed fused Inconel 718. Materialia Mar. 2022;21:101272. https://doi.org/10.1016/j.mtla.2021.101272.

[136] Wei HL, Mazumder J, DebRoy T. Evolution of solidification texture during additive manufacturing. Sci Rep Nov. 2015;5(1):1. https://doi.org/10.1038/srep16446.

[137] Liu SY, Li HQ, Qin CX, Zong R, Fang XY. The effect of energy density on texture and mechanical anisotropy in selective laser melted Inconel 718. Mater Des Jun. 2020;191:108642. https://doi.org/10.1016/j.matdes.2020.108642.

[138] Karimi P, et al. Columnar-to-equiaxed grain transition in powder bed fusion via mimicking casting solidification and promoting in situ recrystallization. Addit Manuf Oct. 2021;46:102086. https://doi.org/10.1016/j.addma.2021.102086.
[139] Trosch T, Strößner J, Völkl R, Glatzel U. Microstructure and mechanical properties of selective laser melted Inconel 718 compared to forging and casting. Mater Lett Feb. 2016;164:428–31. https://doi.org/10.1016/j.matlet.2015.10.136.
[140] Andrieu E, Molins R, Ghonem H, Pineau A. Intergranular crack tip oxidation mechanism in a nickel-based superalloy. Mater Sci Eng A Jun. 1992;154(1):21–8. https://doi.org/10.1016/0921-5093(92)90358-8.
[141] Balachandramurthi AR, Moverare J, Dixit N, Deng D, Pederson R. Microstructural influence on fatigue crack propagation during high cycle fatigue testing of additively manufactured Alloy 718. Mater Charact Mar. 2019;149:82–94. https://doi.org/10.1016/j.matchar.2019.01.018.
[142] Sheridan L, Gockel JE, Scott-Emuakpor OE. Stress-defect-life interactions of fatigued additively manufactured alloy 718. Int J Fatigue Feb. 2021;143:106033. https://doi.org/10.1016/j.ijfatigue.2020.106033.
[143] Reed RC. The Superalloys: Fundamentals and Applications. Cambridge University Press; 2008.
[144] Ghorbanpour S, et al. Effect of microstructure induced anisotropy on fatigue behaviour of functionally graded Inconel 718 fabricated by additive manufacturing. Mater Charact Sep. 2021;179:111350. https://doi.org/10.1016/j.matchar.2021.111350.
[145] Sabelkin VP, et al. Mitigation of anisotropic fatigue in nickel alloy 718 manufactured via selective laser melting. Mater Des Nov. 2019;182:108095. https://doi.org/10.1016/j.matdes.2019.108095.
[146] Pei C, Shi D, Yuan H, Li H. Assessment of mechanical properties and fatigue performance of a selective laser melted nickel-base superalloy Inconel 718. Mater Sci Eng A Jun. 2019;759:278–87. https://doi.org/10.1016/j.msea.2019.05.007.
[147] Konečná R, Nicoletto G, Kunz L, Bača A. Microstructure and directional fatigue behavior of Inconel 718 produced by selective laser melting. Procedia Struct Integr Jan. 2016;2:2381–8. https://doi.org/10.1016/j.prostr.2016.06.298.
[148] Ma XF, et al. Fatigue short crack propagation behavior of selective laser melted Inconel 718 alloy by in-situ SEM study: Influence of orientation and temperature. Int J Fatigue Oct. 2020;139:105739. https://doi.org/10.1016/j.ijfatigue.2020.105739.
[149] Balachandramurthi AR, Moverare J, Hansson T, Pederson R. Anisotropic fatigue properties of Alloy 718 manufactured by Electron Beam Powder Bed Fusion. Int J Fatigue Dec. 2020;141:105898. https://doi.org/10.1016/j.ijfatigue.2020.105898.
[150] Balachandramurthi AR, Moverare J, Dixit N, Pederson R. Influence of defects and as-built surface roughness on fatigue properties of additively manufactured Alloy 718. Mater Sci Eng A Sep. 2018;735:463–74. https://doi.org/10.1016/j.msea.2018.08.072.
[151] Pegues J, Roach M, Scott Williamson R, Shamsaei N. Surface roughness effects on the fatigue strength of additively manufactured Ti-6Al-4V. Int J Fatigue, vol. 116, pp. 543–552, Nov. 2018, doi: 10.1016/j.ijfatigue.2018.07.013.
[152] Sanaei N, Fatemi A, Phan N. Defect characteristics and analysis of their variability in metal L-PBF additive manufacturing. Mater Des Nov. 2019;182:108091. https://doi.org/10.1016/j.matdes.2019.108091.
[153] Snell R, et al. Methods for rapid pore classification in metal additive manufacturing. JOM Jan. 2020;72(1):101–9. https://doi.org/10.1007/s11837-019-03761-9.
[154] Mukherjee T, Zhang W, DebRoy T. An improved prediction of residual stresses and distortion in additive manufacturing. Comput Mater Sci Jan. 2017;126:360–72. https://doi.org/10.1016/j.commatsci.2016.10.003.
[155] Günther J, et al. Fatigue life of additively manufactured Ti–6Al–4V in the very high cycle fatigue regime. Int J Fatigue Jan. 2017;94:236–45. https://doi.org/10.1016/j.ijfatigue.2016.05.018.
[156] Meneghetti G, Rigon D, Gennari C. An analysis of defects influence on axial fatigue strength of maraging steel specimens produced by additive manufacturing. Int J Fatigue Jan. 2019;118:54–64. https://doi.org/10.1016/j.ijfatigue.2018.08.034.
[157] Poulin J-R, Kreitcberg A, Terriault P, Brailovski V. Fatigue strength prediction of laser powder bed fusion processed Inconel 625 specimens with intentionally-seeded porosity: Feasibility study. Int J Fatigue Mar. 2020;132:105394. https://doi.org/10.1016/j.ijfatigue.2019.105394.
[158] Hamidi Nasab M, Romano S, Gastaldi D, Beretta S, Vedani M. Combined effect of surface anomalies and volumetric defects on fatigue assessment of AlSi7Mg fabricated via laser powder bed fusion. Addit Manuf, vol. 34, p. 100918, Aug. 2020, doi: 10.1016/j.addma.2019.100918.
[159] Murakami Y. Chapter 2 - stress concentration. In: Metal Fatigue, Y. Murakami, Ed. Oxford: Elsevier Science Ltd, 2002, pp. 11–24. doi: 10.1016/B978-008044064-4/50002-5.
[160] Bond DM, Zikry MA. Effects of electron beam manufacturing induced defects on fracture in Inconel 718. Addit Manuf Mar. 2020;32:101059. https://doi.org/10.1016/j.addma.2020.101059.
[161] Sheridan L, Scott-Emuakpor OE, George T, Gockel JE. Relating porosity to fatigue failure in additively manufactured alloy 718. Mater Sci Eng A Jun. 2018;727:170–6. https://doi.org/10.1016/j.msea.2018.04.075.
[162] Texier D, et al. Microstructural features controlling the variability in low-cycle fatigue properties of alloy inconel 718DA at intermediate temperature. Metall Mater Trans A Mar. 2016;47(3):1096–109. https://doi.org/10.1007/s11661-015-3291-8.
[163] Komarasamy M, Shukla S, Williams S, Kandasamy K, Kelly S, Mishra RS. Microstructure, fatigue, and impact toughness properties of additively manufactured nickel alloy 718. Addit Manuf Aug. 2019;28:661–75. https://doi.org/10.1016/j.addma.2019.06.009.
[164] Li S, et al. The effect of delta-phase on crack propagation under creep and fatigue conditions in alloy 718, 1994, doi: 10.7449/1994/SUPERALLOYS_1994_545_555.
[165] Yoo YSJ, Book TA, Sangid MD, Kacher J. Identifying strain localization and dislocation processes in fatigued Inconel 718 manufactured from selective laser melting. Mater Sci Eng A May 2018;724:444–51. https://doi.org/10.1016/j.msea.2018.03.127.
[166] Ma T, Zhang G-P, Tan P, Zhang B. Effects of homogenization temperature on creep performance of laser powder bed fusion-fabricated Inconel 718 at 650 °C. Mater Sci Eng A Sep. 2022;853:143794. https://doi.org/10.1016/j.msea.2022.143794.
[167] Balachandramurthi AR, et al. On the microstructure of laser beam powder bed fusion alloy 718 and its influence on the low cycle fatigue behaviour. Materials 2020;13(22):5198.
[168] Xiao L, Chen DL, Chaturvedi MC. Shearing of γ″ precipitates and formation of planar slip bands in Inconel 718 during cyclic deformation. Scr Mater Apr. 2005;52(7):603–7. https://doi.org/10.1016/j.scriptamat.2004.11.023.
[169] Choi H, Kim S, Goto M, Kim S. Effect of powder recycling on room and elevated temperature damage tolerability of Inconel 718 alloy fabricated by laser powder bed fusion. Mater Charact Jan. 2021;171:110818. https://doi.org/10.1016/j.matchar.2020.110818.
[170] Sadeghi E, Pant P, Jafari R, Peng RL, Karimi P. Subsurface grain refinement in electron beam-powder bed fusion of Alloy 718: Surface texture and oxidation performance. Mater Charact Oct. 2020;168:110567. https://doi.org/10.1016/j.matchar.2020.110567.
[171] Čapek J, Polatidis E, Casati N, Pederson R, Lyphout C, Strobl M. Influence of laser powder bed fusion scanning pattern on residual stress and microstructure of alloy 718. Mater Des Sep. 2022;221:110983. https://doi.org/10.1016/j.matdes.2022.110983.
[172] Ravichander BB, et al. Experimental investigation of laser scan strategy on the microstructure and properties of Inconel 718 parts fabricated by laser powder bed fusion. Mater Charact Apr. 2022;186:111765. https://doi.org/10.1016/j.matchar.2022.111765.
[173] Sadeghi E, Prabhat P, Jafari R, Peng R, Karimi P. Subsurface grain refinement in powder bed fusion Alloy 718: Surface texture and oxidation performance. Mater Charact 2020.
[174] Klotz T, Delbergue D, Bocher P, Lévesque M, Brochu M. Surface characteristics and fatigue behavior of shot peened Inconel 718. Int J Fatigue May 2018;110:10–21. https://doi.org/10.1016/j.ijfatigue.2018.01.005.
[175] Salvati E, Korsunsky AM. An analysis of macro- and micro-scale residual stresses of Type I, II and III using FIB-DIC micro-ring-core milling and crystal plasticity FE modelling. Int J Plast Nov. 2017;98:123–38. https://doi.org/10.1016/j.ijplas.2017.07.004.
[176] Everaerts J, Salvati E, Uzun F, Romano Brandt L, Zhang H, Korsunsky AM. Separating macro- (Type I) and micro- (Type II+III) residual stresses by ring-core FIB-DIC milling and eigenstrain modelling of a plastically bent titanium alloy bar, Acta Mater, vol. 156, pp. 43–51, Sep. 2018, doi: 10.1016/j.actamat.2018.06.035.

[177] Balachandramurthi AR, Moverare J, Mahade S, Pederson R. Additive manufacturing of alloy 718 via electron beam melting: effect of post-treatment on the microstructure and the mechanical properties. Materials, vol. 12, no. 1, Art. no. 1, Jan. 2019, doi: 10.3390/ma12010068.
[178] Witkin DB, Patel DN, Bean GE. Notched fatigue testing of Inconel 718 prepared by selective laser melting. Fatigue Fract Eng Mater Struct 2019;42(1):166–77. https://doi.org/10.1111/ffe.12880.
[179] Uriati F, Nicoletto G, Lutey AHA. As-built surface quality and fatigue resistance of Inconel 718 obtained by additive manufacturing. Mater Des Process Commun 2021;3(4):e228.
[180] Gorelik M. Additive manufacturing in the context of structural integrity. Int J Fatigue Jan. 2017;94:168–77. https://doi.org/10.1016/j.ijfatigue.2016.07.005.
[181] Benedetti M, Santus C. Notch fatigue and crack growth resistance of Ti-6Al-4V ELI additively manufactured via selective laser melting: A critical distance approach to defect sensitivity. Int J Fatigue Apr. 2019;121:281–92. https://doi.org/10.1016/j.ijfatigue.2018.12.020.
[182] Solberg K, Berto F. Notch-defect interaction in additively manufactured Inconel 718. Int J Fatigue May 2019;122:35–45. https://doi.org/10.1016/j.ijfatigue.2018.12.021.
[183] Brenne F, Niendorf T. Effect of notches on the deformation behavior and damage evolution of additively manufactured 316L specimens under uniaxial quasi-static and cyclic loading. Int J Fatigue Oct. 2019;127:175–89. https://doi.org/10.1016/j.ijfatigue.2019.05.018.
[184] Peron M, Torgersen J, Ferro P, Berto F. Fracture behaviour of notched as-built EBM parts: Characterization and interplay between defects and notch strengthening behaviour. Theor Appl Fract Mech Dec. 2018;98:178–85. https://doi.org/10.1016/j.tafmec.2018.10.004.
[185] Fatemi A, Molaei R, Phan N. Multiaxial fatigue of additive manufactured metals: Performance, analysis, and applications. Int J Fatigue May 2020;134:105479. https://doi.org/10.1016/j.ijfatigue.2020.105479.
[186] Townsend A, Senin N, Blunt L, Leach RK, Taylor JS. Surface texture metrology for metal additive manufacturing: a review. Precis Eng Oct. 2016;46:34–47. https://doi.org/10.1016/j.precisioneng.2016.06.001.
[187] Fan J, McDowell DL, Horstemeyer MF, Gall K. Cyclic plasticity at pores and inclusions in cast Al–Si alloys. Eng Fract Mech Jul. 2003;70(10):1281–302. https://doi.org/10.1016/S0013-7944(02)00097-8.
[188] Solberg K, Berto F. The effect of defects and notches in quasi-static and fatigue loading of Inconel 718 specimens produced by selective laser melting. Int J Fatigue Aug. 2020;137:105637. https://doi.org/10.1016/j.ijfatigue.2020.105637.
[189] Lei X, Li C, Shi X, Xu X, Wei Y. Notch strengthening or weakening governed by transition of shear failure to normal mode fracture. Sci Rep May 2015;5. https://doi.org/10.1038/srep10537.
[190] Magnien J, Cosemans P, Nutal N, Kairet T. Current surface issues in additive manufacturing. Plasma Process Polym 2020;17(1):1900154. https://doi.org/10.1002/ppap.201900154.
[191] Kotzem D, Dumke P, Sepehri P, Tenkamp J, Walther F. Effect of miniaturization and surface roughness on the mechanical properties of the electron beam melted superalloy Inconel®718. Prog Addit Manuf Oct. 2019. https://doi.org/10.1007/s40964-019-00101-w.
[192] Gockel J, Sheridan L, Koerper B, Whip B. The influence of additive manufacturing processing parameters on surface roughness and fatigue life. Int J Fatigue Jul. 2019;124:380–8. https://doi.org/10.1016/j.ijfatigue.2019.03.025.
[193] Konečná R, Nicoletto G. On the link between as-built surface quality and fatigue behavior of additively manufactured Inconel 718. Procedia Struct Integr Jan. 2019;23:384–9. https://doi.org/10.1016/j.prostr.2020.01.117.
[194] Nicoletto G. Smooth and notch fatigue behavior of selectively laser melted Inconel 718 with as-built surfaces. Int J Fatigue Nov. 2019;128:105211. https://doi.org/10.1016/j.ijfatigue.2019.105211.
[195] Tada H, Paris PC, Irwin GR. The Stress Analysis of Cracks Handbook, Third Edition. Three Park Avenue New York, NY 10016-5990: ASME, 2000. doi: 10.1115/1.801535.
[196] Liu SY, Shao S, Guo H, Zong R, Qin CX, Fang XY. The microstructure and fatigue performance of Inconel 718 produced by laser-based powder bed fusion and post heat treatment. Int J Fatigue Mar. 2022;156:106700. https://doi.org/10.1016/j.ijfatigue.2021.106700.
[197] Georgilas K, Sergi A, Khan RHU, Kartal ME. Investigation of novel post-thermal treatments of alloy 718 fabricated by modulated laser powder bed fusion. Mater Sci Eng A Aug. 2022;849:143502. https://doi.org/10.1016/j.msea.2022.143502.
[198] Ostergaard HE, Pribe JD, Tarik Hasib M, Paradowska AM, Siegmund T, Kruzic JJ. Near-threshold fatigue crack growth in laser powder bed fusion produced alloy 718. Int J Fatigue, vol. 163, p. 107041, Oct. 2022, doi: 10.1016/j.ijfatigue.2022.107041.
[199] Gruber K, Stopyra W, Kobiela K, Madejski B, Malicki M, Kurzynowski T. Mechanical properties of Inconel 718 additively manufactured by laser powder bed fusion after industrial high-temperature heat treatment. J Manuf Process Jan. 2022;73:642–59. https://doi.org/10.1016/j.jmapro.2021.11.053.
[200] Tammas-Williams S, Withers PJ, Todd I, Prangnell PB. Porosity regrowth during heat treatment of hot isostatically pressed additively manufactured titanium components. Scr Mater Sep. 2016;122:72–6. https://doi.org/10.1016/j.scriptamat.2016.05.002.
[201] du Plessis A, Macdonald E. Hot isostatic pressing in metal additive manufacturing: X-ray tomography reveals details of pore closure. Addit Manuf Aug. 2020;34:101191. https://doi.org/10.1016/j.addma.2020.101191.
[202] Cunningham R, et al. Analyzing the effects of powder and post-processing on porosity and properties of electron beam melted Ti-6Al-4V. Mater Res Lett Nov. 2017;5(7):516–25. https://doi.org/10.1080/21663831.2017.1340911.
[203] Kaletsch A, Qin S, Herzog S, Broeckmann C. Influence of high initial porosity introduced by laser powder bed fusion on the fatigue strength of Inconel 718 after post-processing with hot isostatic pressing. Addit Manuf Nov. 2021;47:102331. https://doi.org/10.1016/j.addma.2021.102331.
[204] Aydinöz ME, et al. On the microstructural and mechanical properties of post-treated additively manufactured Inconel 718 superalloy under quasi-static and cyclic loading. Mater Sci Eng A Jul. 2016;669:246–58. https://doi.org/10.1016/j.msea.2016.05.089.
[205] Kanagarajah P, Brenne F, Niendorf T, Maier HJ. Inconel 939 processed by selective laser melting: Effect of microstructure and temperature on the mechanical properties under static and cyclic loading. Mater Sci Eng A Dec. 2013;588:188–95. https://doi.org/10.1016/j.msea.2013.09.025.
[206] Lee S, Shao S, Wells DN, Zetek M, Kepka M, Shamsaei N. Fatigue behavior and modeling of additively manufactured IN718: The effect of surface treatments and surface measurement techniques. J Mater Process Technol Apr. 2022;302:117475. https://doi.org/10.1016/j.jmatprotec.2021.117475.
[207] Yang K, et al. Very high cycle fatigue behaviors of a turbine engine blade alloy at various stress ratios. Int J Fatigue Jun. 2017;99:35–43. https://doi.org/10.1016/j.ijfatigue.2016.11.032.
[208] Yu C, Huang Z, Zhang Z, Shen J, Wang J, Xu Z. Influence of post-processing on very high cycle fatigue resistance of Inconel 718 obtained with laser powder bed fusion. Int J Fatigue Dec. 2021;153:106510. https://doi.org/10.1016/j.ijfatigue.2021.106510.
[209] Ono Y, Yuri T, Sumiyoshi H, Takeuchi E, Matsuoka S, Ogata T. High-cycle fatigue properties at cryogenic temperatures in INCONEL 718 nickel-based superalloy. Mater Trans 2004;45(2):342–5. https://doi.org/10.2320/matertrans.45.342.
[210] Ono Y, Yuri T, Nagashima N, Sumiyoshi H, Ogata T, Nagao N. High-cycle fatigue properties of alloy718 base metal and electron beam welded joint. Phys Procedia Jan. 2015;67:1028–35. https://doi.org/10.1016/j.phpro.2015.06.196.
[211] Sivaprasad K, Raman SGS. Influence of magnetic arc oscillation and current pulsing on fatigue behavior of alloy 718 TIG weldments. Mater Sci Eng A Mar. 2007;448(1):120–7. https://doi.org/10.1016/j.msea.2006.10.048.
[212] Tillmann W, Schaak C, Nellesen J, Schaper M, Aydinöz ME, Hoyer K-P. Hot isostatic pressing of IN718 components manufactured by selective laser melting. Addit Manuf Jan. 2017;13:93–102. https://doi.org/10.1016/j.addma.2016.11.006.
[213] Zhang Y, Duan Z, Shi H. Comparison of the very high cycle fatigue behaviors of INCONEL 718 with different loading frequencies. Sci China Phys Mech Astron Mar. 2013;56(3):617–23. https://doi.org/10.1007/s11433-013-5013-9.
[214] Chen Q, Kawagoishi N, Wang QY, Yan N, Ono T, Hashiguchi G. Small crack behavior and fracture of nickel-based superalloy under ultrasonic fatigue. Int J Fatigue Oct. 2005;27(10):1227–32. https://doi.org/10.1016/j.ijfatigue.2005.07.022.
[215] Konečná R, Kunz L, Nicoletto G, Bača A. Long fatigue crack growth in Inconel 718 produced by selective laser melting. Int J Fatigue Nov. 2016;92:499–506. https://doi.org/10.1016/j.ijfatigue.2016.03.012.
[216] Gruber K, et al. Fatigue crack growth characterization of Inconel 718 after additive manufacturing by laser powder bed fusion and heat treatment. Int J Fatigue Jan. 2023;166:107287. https://doi.org/10.1016/j.ijfatigue.2022.107287.

[217] Xiao L, Chen DL, Chaturvedi MC. Effect of boron on fatigue crack growth behavior in superalloy IN 718 at RT and 650°C. Mater Sci Eng A Jul. 2006;428(1):1–11. https://doi.org/10.1016/j.msea.2005.08.206.
[218] Osinkolu GA, Onofrio G, Marchionni M. Fatigue crack growth in polycrystalline IN 718 superalloy. Mater Sci Eng A Sep. 2003;356(1):425–33. https://doi.org/10.1016/S0921-5093(03)00156-4.
[219] Abikchi M, et al. Fatigue life and initiation mechanisms in wrought Inconel 718 DA for different microstructures, Jun. 2013, p. 11 p. Accessed: Dec. 31, 2020. [Online]. Available: https://hal-mines-paristech.archives-ouvertes.fr/hal-00853448.
[220] Clavel M, Pineau A. Frequency and wave-form effects on the fatigue crack growth behavior of alloy 718 at 298 K and 823 K. Metall Trans A Apr. 1978;9(4):471–80. https://doi.org/10.1007/BF02646402.
[221] Mercer C, Soboyejo ABO, Soboyejo WO. Micromechanisms of fatigue crack growth in a forged Inconel 718 nickel-based superalloy. Mater Sci Eng A Sep. 1999;270(2):308–22. https://doi.org/10.1016/S0921-5093(99)00214-2.
[222] Yamada Y, Newman JC. Crack closure under high load-ratio conditions for Inconel-718 near threshold behavior. Eng Fract Mech Jan. 2009;76(2):209–20. https://doi.org/10.1016/j.engfracmech.2008.09.009.
[223] Andersson H, Persson C. In-situ SEM study of fatigue crack growth behaviour in IN718. Int J Fatigue Mar. 2004;26(3):211–9. https://doi.org/10.1016/S0142-1123(03)00172-5.
[224] Clavel M, Pineau A. Fatigue behaviour of two nickel-base alloys I: Experimental results on low cycle fatigue, fatigue crack propagation and substructures. Mater Sci Eng Sep. 1982;55(2):157–71. https://doi.org/10.1016/0025-5416(82)90129-X.
[225] Yuen JL, Roy P, Nix WD. Effect of oxidation kinetics on the near threshold fatigue crack growth behavior of a nickel base superalloy. Metall Trans A Sep. 1984;15(9):1769–75. https://doi.org/10.1007/BF02666360.
[226] Andersson H, Persson C, Hansson T. Crack growth in IN718 at high temperature. Int J Fatigue Oct. 2001;23(9):817–27. https://doi.org/10.1016/S0142-1123(01)00031-7.
[227] Gustafsson D, Lundström E. High temperature fatigue crack growth behaviour of Inconel 718 under hold time and overload conditions. Int J Fatigue Mar. 2013;48:178–86. https://doi.org/10.1016/j.ijfatigue.2012.10.018.
[228] Gustafsson D, et al. Influence of high temperature hold times on the fatigue crack propagation in Inconel 718. Int J Fatigue Nov. 2011;33(11):1461–9. https://doi.org/10.1016/j.ijfatigue.2011.05.011.
[229] Gustafsson D, Lundström E, Simonsson K. Modelling of high temperature fatigue crack growth in Inconel 718 under hold time conditions. Int J Fatigue Jul. 2013;52:124–30. https://doi.org/10.1016/j.ijfatigue.2013.03.004.
[230] Krupp U, McMahon CJ. Dynamic embrittlement–time-dependent brittle fracture. J Alloys Compd Sep. 2004;378(1):79–84. https://doi.org/10.1016/j.jallcom.2003.10.074.
[231] Bricknell RH, Woodford DA. Grain boundary embrittlement of the iron-base superalloy IN903A. Metall Trans A Sep. 1981;12(9):1673–80. https://doi.org/10.1007/BF02643573.
[232] Pfaendtner JA, McMahon Jr CJ. Oxygen-induced intergranular cracking of a Ni-base alloy at elevated temperatures—an example of dynamic embrittlement. Acta Mater Sep. 2001;49(16):3369–77. https://doi.org/10.1016/S1359-6454(01)00005-2.
[233] Kane WM, Krupp U, McMahon CJ. Part I: Anisotropy of cracking from oxygen-induced dynamic embrittlement in bicrystals of IN718. Mater Sci Eng A May 2009;507(1):58–60. https://doi.org/10.1016/j.msea.2008.12.002.
[234] Kane WM, McMahon CJ. Part II. Effects of grain-boundary structure on the path of cracking in polycrystals. Mater Sci Eng A May 2009;507(1):61–5. https://doi.org/10.1016/j.msea.2008.07.015.
[235] Deng D, Eriksson R, Peng RL, Moverare J. On the dwell-fatigue crack propagation behavior of a high-strength Ni-base superalloy manufactured by selective laser melting. Metall Mater Trans A Feb. 2020;51(2):962–72. https://doi.org/10.1007/s11661-019-05548-8.
[236] Kuo Y-L, Nagahari T, Kakehi K. The effect of post-processes on the microstructure and creep properties of alloy718 built up by selective laser melting. Materials Jun. 2018;11(6):6. https://doi.org/10.3390/ma11060996.
[237] Tian Y, Tomus D, Rometsch P, Wu X. Influences of processing parameters on surface roughness of Hastelloy X produced by selective laser melting. Addit Manuf Jan. 2017;13:103–12. https://doi.org/10.1016/j.addma.2016.10.010.
[238] Karimi P, Schnur C, Sadeghi E, Andersson J. Contour design to improve topographical and microstructural characteristics of Alloy 718 manufactured using electron beam-powder bed fusion. Addit Manuf Dec. 2019:101014. https://doi.org/10.1016/j.addma.2019.101014.
[239] Enrique PD, et al. Enhancing fatigue life of additive manufactured parts with electrospark deposition post-processing. Addit Manuf Dec. 2020;36:101526. https://doi.org/10.1016/j.addma.2020.101526.
[240] Morton PA, Mireles J, Mendoza H, Cordero PM, Benedict M, Wicker RB. Enhancement of low-cycle fatigue performance from tailored microstructures enabled by electron beam melting additive manufacturing technology. J Mech Des Nov. 2015;137(11). https://doi.org/10.1115/1.4031057.
[241] Polonsky AT, Echlin MP, Lenthe WC, Dehoff RR, Kirka MM, Pollock TM. Defects and 3D structural inhomogeneity in electron beam additively manufactured Inconel 718. Mater Charact Sep. 2018;143:171–81. https://doi.org/10.1016/j.matchar.2018.02.020.
[242] Esmaeilizadeh R, et al. On the effect of laser powder-bed fusion process parameters on quasi-static and fatigue behaviour of Hastelloy X: A microstructure/defect interaction study. Addit Manuf Feb. 2021;38:101805. https://doi.org/10.1016/j.addma.2020.101805.
[243] Popovich VA, Borisov EV, Popovich AA, Sufiiarov VS, Masaylo DV, Alzina L. Functionally graded Inconel 718 processed by additive manufacturing: Crystallographic texture, anisotropy of microstructure and mechanical properties. Mater Des 2017;114:441–9. https://doi.org/10.1016/j.matdes.2016.10.075.
[244] Karimi P, Schnur C, Sadeghi E, Andersson J. Contour design to improve topographical and microstructural characteristics of Alloy 718 manufactured by electron beam-powder bed fusion technique. Addit Manuf Mar. 2020;32:101014. https://doi.org/10.1016/j.addma.2019.101014.
[245] Karimi P, Sadeghi E, Deng D, Gruber H, Andersson J, Nylén P. Influence of build layout and orientation on microstructural characteristics of electron beam melted Alloy 718. Int J Adv Manuf Technol Dec. 2018;99(9):2903–13. https://doi.org/10.1007/s00170-018-2621-6.
[246] Karimi P, Sadeghi E, Ålgårdh J, Harlin P, Andersson J. Effect of build location on microstructural characteristics and corrosion behavior of EB-PBF built Alloy 718. Int J Adv Manuf Technol Feb. 2020;106(7):3597–607. https://doi.org/10.1007/s00170-019-04859-9.
[247] Körner C, Helmer H, s AB, Singer RF. Tailoring the grain structure of IN718 during selective electron beam melting, 2014. doi: 10.1051/matecconf/20141408001.
[248] Helmer HE, Körner C, Singer RF. Additive manufacturing of nickel-based superalloy Inconel 718 by selective electron beam melting: Processing window and microstructure. J Mater Res Sep. 2014;29(17):1987–96. https://doi.org/10.1557/jmr.2014.192.
[249] Helmer H, Bauereiß A, Singer RF, Körner C. Grain structure evolution in Inconel 718 during selective electron beam melting. Mater Sci Eng A Jun. 2016;668:180–7. https://doi.org/10.1016/j.msea.2016.05.046.
[250] Kou S. Welding Metallurgy, 2nd Edition. Wiley, 2002. Accessed: May 09, 2020. [Online]. Available: https://www.wiley.com/en-us/Welding+Metallurgy%2C+2nd+Edition-p-9780471434917.
[251] ASTM F3055-14a. Specification for additive manufacturing nickel alloy (UNS N07718) with powder bed fusion. ASTM International, West Conshohocken, PA, 2014. doi: 10.1520/F3055-14A.
[252] Kevinsanny, et al. Defect tolerance and hydrogen susceptibility of the fatigue limit of an additively manufactured Ni-based superalloy 718. Int J Fatigue Oct. 2020;139:105740. https://doi.org/10.1016/j.ijfatigue.2020.105740.
[253] Helmer H, Bauereiß A, Singer RF, Körner C. Grain structure evolution in Inconel 718 during selective electron beam melting. Mater Sci Eng Struct Mater Prop Microstruct Process 2016;668:180–7. https://doi.org/10.1016/j.msea.2016.05.046.
[254] Stenerud G, Johnsen R, Olsen JS, He J, Barnoush A. Effect of hydrogen on dislocation nucleation in alloy 718. Int J Hydrog Energy Jun. 2017;42(24):15933–42. https://doi.org/10.1016/j.ijhydene.2017.04.290.
[255] Reid A, et al. Application of neutron imaging to detect and quantify fatigue cracking. Int J Mech Sci Aug. 2019;159:182–94. https://doi.org/10.1016/j.ijmecsci.2019.05.037.

[256] Neikter M, et al. Defect characterization of electron beam melted Ti-6Al-4V and Alloy 718 with X-ray microtomography. Aeronaut Aerosp Open Access J 2018; 2(3):3.
[257] Cakmak E, et al. Mechanical characterization of an additively manufactured inconel 718 theta-shaped specimen. Metall Mater Trans A Feb. 2016;47(2): 971–80. https://doi.org/10.1007/s11661-015-3186-8.
[258] Fatemi A, Shamsaei N. Multiaxial fatigue: An overview and some approximation models for life estimation. Int J Fatigue Aug. 2011;33(8):948–58. https://doi.org/10.1016/j.ijfatigue.2011.01.003.
[259] Fatemi A, Molaei R, Phan N. Multiaxial fatigue of additive manufactured metals. MATEC Web Conf 2019;300:01003. https://doi.org/10.1051/matecconf/201930001003.
[260] Assessment of multiaxial fatigue life prediction methodologies for Inconel 718. Procedia Eng, vol. 2, no. 1, pp. 2347–2356, Apr. 2010, doi: 10.1016/j.proeng.2010.03.251.
[261] Sabelkin VP, Cobb GR, Doane BM, Kemnitz RA, O'Hara RP. Torsional behavior of additively manufactured nickel alloy 718 under monotonic loading and low cycle fatigue. Mater Today Commun Sep. 2020;24:101256. https://doi.org/10.1016/j.mtcomm.2020.101256.